2019

CREEP DEFORMATION MECHANISMS IN CARBIDE PRECIPITATE STRENGTHENED NICKEL-BASED SUPERALLOYS AT ELEVATED TEMPERATURES

Michael Lapera
University of Rhode Island, mlapera.11@gmail.com

CREEP DEFORMATION MECHANISMS IN CARBIDE PRECIPITATE STRENGTHENED NICKEL-BASED SUPERALLOYS AT ELEVATED TEMPERATURES

BY

MICHAEL A. LAPERA

A THESIS SUBMITTED IN PARTIAL FULFILLMENT OF THE

REQUIREMENTS FOR THE DEGREE OF

MASTER OF SCIENCE

IN

MECHANICAL ENGINEERING AND APPLIED MECHANICS

UNIVERSITY OF RHODE ISLAND

2019

MASTER OF SCIENCE THESIS

OF

MICHAEL A. LAPERA

APPROVED:

Thesis Committee

Major Professor Hamouda Ghonem

David Taggart

Hongyan Yuan

Otto Gregory

Nasser H. Zawia
DEAN OF THE GRADUATE SCHOOL

UNIVERSITY OF RHODE ISLAND

2019

ABSTRACT

Creep deformation of nickel-based superalloys at elevated temperatures is inherently dependent on the microstructural state of the material. Carbides have been observed to suppress intragranular and intergranular deformation rates at elevated temperatures by impeding dislocation motion within the grain and along the grain boundary. First, the rate controlling effects of intra- and intergranular carbides as it relates to the grain boundary sliding are examined. A microstructurally sensitive, viscous description and model of grain boundary sliding is then presented. This work provides the concepts and mathematical formulation to model the rate controlling processes governing the grain boundary sliding associated with creep of carbide-strengthened superalloy Inconel 617 (IN617). The framework of the model considers both the microstructural state (size, volume fraction, and spacing of carbides) in the matrix, as well as along the grain boundary when determining the overall sliding rate. The model accounts for the role of carbides as they pertain to dislocation arrival/absorption into the grain boundary and the rate at which they glide and climb along the grain boundary plane, resulting in grain boundary sliding. It is considered that grain boundary sliding necessitates the supply of extrinsic dislocations from the matrix to facilitate sliding and, as such, the rate at which dislocations arrive to and are absorbed into the grain boundary dictates the overall sliding rate. Carbides along the grain boundary are then modeled as accumulation points for backstress which suppresses grain boundary sliding as a function of their size and spacing. At elevated temperatures, carbides within the matrix and along the grain boundary are subjected to diffusional

processes resulting in time-dependent microstructure and mechanical response, requiring a detailed understanding of the rate controlling properties of both intra- and intergranular carbides as they pertain to grain boundary sliding and creep deformation.

Following this, a method of using stress relaxation tests carried out at 780 °C on IN617 specimens of various aging exposure times to examine the effect that the matrix microstructure exerts over the material's deformation at elevated temperatures is explored. Included in this experimental work are quantitative microstructural assessments of IN617 specimens of various exposure times through the use of scanning electron microscopy (SEM). Once the microstructure of the material has been evaluated, the elevated temperature stress relaxation tests are utilized as a means of producing accelerated creep behavior via interconversion of stress relaxation data to creep strain data.

At 780°C, above the solvus temperature of gamma prime (γ'), but below that of the chromium-rich $M_{23}C_6$ carbides, the microstructure could be regarded as constant. In doing this, the time dependent nature of the $M_{23}C_6$ carbide evolution was able to be eliminated, thereby allowing a "snapshot in time" with fixed carbide radius, volume fraction, and spacing values which could be quantified via SEM. As the inelastic sliding of the viscous grain boundary is asserted to provide the means of stress relaxation, holding constant the grain and grain boundary microstructure allowed for determination of the number of grain boundary dislocations (n_{gb}) required to produce the corresponding amount of grain boundary displacement. This is achieved by analyzing the matrix and grain boundary dislocation behavior

within the framework of a physics-based deformation model which couples the matrix dislocation release (n_m) to the grain boundary dislocation population which – through prevailing glide and climb processes internal to the boundary that occur at the experimental stress and temperature – facilitate grain boundary sliding. A unification of the influence of the matrix and grain boundary microstructure on the creep behavior of IN617 is then provided, proffering a comprehensive and efficient tool for consideration in the design and analysis of carbide precipitate strengthened nickel-based superalloys for high temperature applications.

ACKNOWLEDGEMENTS

I owe an Acknowledgements section that rivals the length of this thesis in order to express the whole-hearted feelings of gratitude to the people who have made this journey possible; even still, such an homage would likely fall short of conveying the depths of my appreciation. I'd like to thank my advisor, Dr. Hamouda Ghonem, for his tutelage and guidance. The knowledge and many lessons you have imparted to me have made an indelible mark. I'd like to thank my friend and colleague, Daniel Spader, with whom I've worked side-by-side in the laboratory. You have been a creative, inspirational, and intellectual engine which has helped propel us through some of our most trying times. Your ingenuity, insight, and optimism will undoubtedly be appreciated wherever your path takes you. I'd also like to thank Dr. David Taggart and Dr. Otto Gregory for their help early in my graduate career. A special thanks is owed to Dr. Hongyan Yuan for his mentoring and assistance in the numerical work involved in my research.

To my mother, Linda - I am immensely indebted to you for being the person I have always been able to look up to and call my best friend. Everything I have accomplished I owe to you, your sacrifices, hard work, and resilience. You are the epitome of a role model and the proof that I turn to when I need to be reminded of how kindness, love, curiosity, and hard work allow us to make a lasting impact on the world. I could never repay you for all that you have given me.

To my sister, Cassie - thank you for always being a fortifying presence in my life and living it in a way which constantly reminds me that the pursuit of knowledge and science is so much more than what it appears on the surface.

To Sunny - for the tireless love and support you show in every way and for sharing in my enthusiasm when it comes to chasing dreams.

To Mike Dean - for being so much more to me and my family than I could have ever realized at the time. Your presence will always be missed, but your love always felt.

To my father, Tony - for always believing in me and teaching me that with a foundation of respect, what we can accomplish in this life is virtually limitless.

I would also like to express my sincere gratitude to Dr. James LeBlanc, Chris DelMastro, Stacy Canepari, and Derek Potvin of the Naval Undersea Warfare Center (Newport, RI) for their support.

PREFACE

This thesis is prepared using Manuscript Format.

Chapter 1 introduces the application of nickel-based superalloy Inconel 617 and its significance in industrial applications. Included are the problem statement to be addressed by, and justification for, this thesis.

Chapter 2 contains the first paper in a two-part paper submitted to the *Journal of the Mechanics and Physics of Solids*. This chapter provides the background information involved in the physics of high temperature creep deformation in nickel-based superalloys. Formulations for the matrix and grain boundary deformation are presented, and a common parameter which acts as a synergistic link between the two forms of deformation is presented. The coupling of the matrix and grain boundary deformation models is explained, which is completed by the introduction of a traction-displacement formality which is used to quantify the amount of inelastic grain boundary sliding which occurs at temperatures above $0.6\text{-}0.7T_m$ in nickel-based superalloys. A discussion of how the model is applied to study the dislocation kinetics based on high temperature stress relaxation tests follows, which is performed in the second part of the two-part paper and presented in Chapter 3. The formatting of this chapter will be in alignment with that which is required for the *Journal of the Mechanics and Physics of Solids*.

Chapter 3 presents a series of experimental heat treatments, quantitative microscopic analyses, and high temperature stress relaxation experiments performed on three test coupons of Inconel 617. A unique heat treatment is applied to each test coupon in order to produce matrix and grain boundary microstructures

which are representative of those which are seen at increasing service life exposure times of the material. Prior to the high temperature stress relaxation tests, the matrix and grain boundary microstructure are investigated via SEM. Following the microstructural characterization, each test coupon is subjected an initial stress of 200 MPa at a temperature of 780 °C and allowed to relax until a sufficiently low rate of relaxation is observed ($\geq$ 20 hrs). The use of stress relaxation data for prediction of primary and secondary creep deformation behavior by way of relaxation to creep strain interconversion is explained within the model framework presented in Chapter 2. Using this technique, the physics-based model is used in an uncoupled fashion to investigate the matrix and grain boundary's microstructural influence on the grain boundary sliding processes which provide a means of stress relaxation within the material. The coupled matrix and grain boundary sliding model will then be used to simulate the high temperature deformation of an additional stress relaxation test which is carried out on a previously relaxed specimen. The formatting for this chapter will be in alignment with that which is required for *Journal of the Mechanics and Physics of Solids*.

Chapter 4 discusses the opportunities for future work and efforts currently underway in the Mechanics of Materials Research Laboratory at the University of Rhode Island.

TABLE OF CONTENTS

LIST OF TABLES

TABLE **PAGE**

LIST OF FIGURES

FIGURE **PAGE**

CHAPTER 1

INTRODUCTION

1.1 Statement of Problem

Nickel-based superalloys have garnered significant interest over the past several decades. Inconel 617 (IN617) is a solid solution strengthened nickel-based alloy predominately comprised of Ni (44.5 min. wt. %), Cr (20 min. wt. %), Co (10 min. wt.%), Mo (8 min. wt. %), Al (0.8 min. wt. %), and C (0.05 min. wt. %)[2]. IN617 has found use in a myriad of components and applications within the aerospace industry, specifically in gas turbine design. In the basic design of the turbojet engine, the components which see the greatest temperature and stress lie in the combustor and turbine sections. As air flows into the turbojet engine, it is pressurized by the compressor and continues into the combustor, where fuel is injected and ignited. This combustion is then turned into mechanical work by the turbine, which in turn spins the compressor through use of a shaft. The hot gas then flows and expands through the turbine section, generating thrust. The temperature at which the gas leaving the combustor enters the turbine has a significant impact on engine efficiency; this parameter is referred to as the turbine inlet temperature. Generally speaking, the higher the turbine inlet temperature, the greater the associated enthalpic input into the turbine and subsequent efficiency. The turbine inlet temperature has increased nearly 700 °C over the span of the last seven decades. With the demand for increasing temperatures, the material capability must follow suit.

IN617 is also a candidate material for the Generation IV next generation very high temperature nuclear reactor (VHTR) components. The VHTR design, unlike its light water (pressurized water or boiling water) reactor counterparts, utilizes the Brayton cycle in lieu of the Rankine cycle. In using the Brayton cycle, a thermal efficiencies in excess of 50% can be seen[3]. This increase in thermal efficiency is driven by greater process temperatures. Even with reactor core helium cooling, primary loop temperatures are expected to exceed the 1000 °C threshold.

The most important design considerations in these applications often pertain to high temperature strength, creep resistance, ductility, oxidation resistance, and fatigue strength. Cr and Al provide superior oxidation resistance at elevated temperatures by forming an oxide layer on the outer surface of the material, while Cr, C, Mo, Ti, and B act as precipitate formers both within the grain and grain boundary. Material ductility is a desirable property in many critical applications as elongation serves as a failure precursor, indicating material strength degradation or prompting further inspection and/or preventative maintenance. This is not the case or brittle materials, where failure is often catastrophic and provides no early warning signs of impending failure. When selecting or designing a material for creep and fatigue environments, different strengthening mechanisms are relied upon to increase the strength and overall service life of the material.

Strengthening mechanisms in superalloys fall into one of several categories: work hardening, solid solution strengthening, grain boundary

strengthening, and precipitation hardening. Work hardening (strain hardening) involves the deliberate increase of dislocations within the grain such that an increase in flow stress results, thereby making plastic deformation more energetically demanding and resulting in a greater yield strength. The amount of hardening results from the balance which is achieved between dislocation storage, annihilation, and rearrangement of dislocations[4]. Solid solution strengthening is a common alloying process which increases the strength of the alloy material through the substitutional or interstitial addition of alloying elements into the base material. The effectiveness of substitutional solid solutioning is dictated by the size effect and the solubility of the solute species – this relationship can be well understood through application of the Hume-Rothery rules. In IN617, the solute elements which provide solid solution strengthening are Co, Fe, Mo, and Cr. Solute atoms affect dislocation mobility by affecting elastic and modulus interactions through distortion of the lattice and localized changes in shear modulus, respectively[5]. The effectiveness of a solute's ability to strengthen the matrix is proportional to the amount of misfit arising from differences in atomic radii. While substitutional solute atoms are only capable of affecting the motion of edge dislocations, interstitial solute atoms can impede both edge and screw dislocations due to the fact that they produce both dilatational and shear lattice distortion[6]. The strengthening of the grain boundary also presents another means of impeding dislocation motion. As dislocations from within the grain attempt to move (or transmit) from one grain to the next, the degree of misorientation between adjacent grains can make this process increasingly

difficult due to the discontinuity of slip planes[3],[6]. When sufficient temperature and stress are present, as dislocations enter and move through the more atomically disorganized (relative to the matrix) grain boundary, their motion produces grain boundary sliding. The more organized the grain boundary becomes, the less free volume exists, and the more difficult it becomes for dislocations to move. This is further compounded by the presence of grain boundary carbides, which act as barriers to dislocation glide. The precipitation hardening mechanisms occur in several different forms which somewhat parallel the means by which solid solutioning strengthens the matrix: stacking-fault strengthening, order strengthening, modulus misfit strengthening, coherency strengthening, and chemical strengthening. When a dislocation encounters a precipitate and is to continue its motion, it must either shear the precipitate, bypass it by way of Orowan looping, or climb over it. A single dislocation shearing a particle generates an anti-phase boundary, in which the stacking sequence of the particle's atomic arrangement is shifted. The energy required depends on the volume fraction, size, and spacing of particles, as these terms dictate whether a strong or weak dislocation coupling occurs. The strength or weakness of the coupling dictates the magnitude of the required, applied stress in order to move dislocations through the particles encountered. Once a critical precipitate radius is reached, Orowan looping becomes more favorable. Orowan looping occurs when a dislocation encounters a precipitate and is forced to bow due to the obstacle's presence. At the point when the maximum curvature of the dislocation is reached, the dislocation will meet around the backside of the precipitate and annihilate the

portion of itself which has opposing signs, and will proceed to continue its motion. In its wake, it leaves behind a dislocation which has now formed a loop around the precipitate. This loop contributes to an increase in backstress for future dislocations which try to bypass the particle[4]. In nickel-based superalloys at temperatures at or exceeding 0.6-0.7T_m, when accompanied by moderate to high stresses, particle looping and shearing will give way to the more energetically favorable dislocation climb. A dislocation climb event requires the motion of a vacancy to the core of the dislocation such that it can move to an adjacent glide plane.

The significance of both matrix (intragranular) and grain boundary (intergranular) deformation in high temperature creep has been explored in depth by many authors since the 1950s. These studies have examined the effects of grain size, grain and grain boundary shape, various crystalline phase/structure formations, and the precipitation of various phases as a function of heat treatment, aging, and service exposure in many different engineering alloys. Grain boundary sliding as a primary deformation mechanism in Nickel-based superalloys is well understood and has been explored in depth over the last several decades. In parallel efforts, much attention has been devoted to understanding the role of grain microstructure in polycrystalline materials and its effects on crystal stress flow during creep. The viscoplasticity models developed for creep applications, specifically in the Coble creep regime (0.6-0.7T_m) which have stemmed from a host of previous research efforts in an attempt to isolate either an intragranular or intergranular mechanism as the rate-controlling process, while effectively

disregarding the interplay or synergistic effects which exist between the grain and grain boundary. This coupling can be shown to be directly related to the availability and motion of matrix dislocations, their absorption by the grain boundary, and subsequent grain boundary dislocation motion, all of which are facilitated by the diffusion of vacancies which occurs during creep in the temperature and stress regime under investigation. To the best of the author's knowledge, there have been no attempts at developing a physics-based model which unifies each of these processes in this manner. The aim of this research is to accomplish this by way of investigation of matrix and grain boundary $M_{23}C_6$ carbide precipitation behavior and the development of two models which are then coupled through a physical term. This term will connect the matrix deformation and grain boundary deformation on the basis of grain-grain boundary accommodation during high temperature deformation. A traction-displacement formality is then applied in order to determine the relationship of the matrix deformation and the subsequent accommodation and deformation of the grain boundary via viscoplastic grain boundary sliding.

1.2 Justification of Thesis

The creep mechanisms of a crystalline material are generally described in terms of dislocation creep (low temperature, high stress) or diffusional creep (high temperature, low to moderate stress). One of the key differences in mechanisms between these two regimes can be explained by the increase in concentration of vacancies and the increase in thermal energy which promotes the ability for

vacancies to diffuse toward or away from dislocations. Without this increase in concentration and mobility of vacancies from sources to sinks (e.g. grain boundaries), edge dislocations are generally confined to glide within their respective slip system; however, as temperatures increase, dislocations become increasingly capable of climb. This becomes important when frictional stress due to dislocation-dislocation interaction approaches the order of magnitude of the applied stress or, most relevant to this thesis, when obstacles to dislocation glide are present, such as matrix carbides.

The crystal lattice has a relatively high degree of order and diffusive motion along the grain boundaries becomes the favored mechanism at lower temperatures. This is due to the lower activation energy threshold required for diffusion in the grain boundary, as the misorientation characteristic of the grain boundaries of polycrystalline materials presents a larger free volume through which diffusion can occur. As temperatures exceed $0.6\text{-}0.7T_m$, the vacancies within the matrix see a significant increase in their concentration and mobility due to the increase in thermal energy. When this increase in energy results in a total value that approaches that of activation energy of self-diffusion within the matrix, the increase in magnitude of intragranular and intergranular diffusive processes follow.

Experimental data pertaining to creep of IN617 and similar nickel-based superalloys suggests a synergistic relationship between matrix and grain boundary deformation. Kihara *et al.*[1] examined the creep behavior of IN617 subjected to various solution treatment and aging processes. It was shown that fine, intragranular carbides precipitate during solution treatment at 1200 °C, while the grain

boundaries remained clean[1],[8]. For specimens that were further aged at 1000 °C, the matrix region showed a noticeably sparser carbide population, while the grain boundaries underwent significant carbide ($M_{23}C_6$ type) precipitation. The creep data produced showed that for specimens that were only solution treated, the primary (transient) creep rate was noticeably slower than that of the aged specimens and entered into steady state creep much earlier. The aged specimens exhibited a more classical sigmoidal behavior with a greater primary creep rate and more pronounced transient creep regime.

Chomette *et al.*[9] in his investigation of IN617, in both the aged and solution treated conditions, further reinforced this difference in primary creep performed at 30 MPa and 950 °C. Furthermore, the similarities in carbide presence in the grain's microstructure to those specimens produced by Kihara *et al.* could be seen in the micrographs of the experimental samples taken over the 1 to 1000 hour aging process which Chomette provided prior to testing. Another observation noted is that the steady state creep rate of the crept specimens – regardless of the heat treatment procedure – proved to be approximately equal once controlled for the grain size.

Soula *et al.*[10] utilized micro-deposited ceramic gridding and micro-extensometry to investigate the qualitative relationship between the intragranular and intergranular deformation of γ'-strengthened NR6 material. It was shown that the amount of local deformation due to grain boundary sliding events is significantly greater than that which occurs due to matrix deformation (via activation of slip bands) and that the grain boundary sliding deformation was largest

in concentrated areas where slip band incidence was high. The authors observed that the increase in the macroscopic strain magnitude is proportional to the increase in both the number of grain boundary sliding events and slip band generations within the matrix. Prior to reaching the threshold strain of approximately 1%, the rate of increase of intragranular deformation was greater than that of the number of grain boundary sliding events, even though grain boundary sliding displacement dominated. As macroscopic strain increases beyond this strain threshold value, local deformation continued to occur at sites which have already undergone deformation (i.e. grain boundaries where sliding had already taken place and grains which had already experienced slip). Soula *et al.*[10] also noted that the localized deformation at the slip band – grain boundary junctions resulted in local deformation that was approximately twice that found elsewhere along the grain boundary under examination and four times that which was found elsewhere within the grain. These observations suggest that the ability for dislocations to move from within the matrix to the grain boundary play a significant role in the deformation mechanism and resulting strain rate. This is also seen in the work of Thibault *et al.*[11] on the same γ'-strengthened NR6 material. In varying the intragranular matrix microstructure by employing the use of different heat treatments, it has been shown that the ability of the dislocations to traverse intragranular obstacles during creep testing at 700 °C was directly reflected in the magnitude of grain boundary sliding strain which occurred.

Intragranular deformation during creep is associated with activation of slip bands, in which multiple slip systems/planes have become activated and create a

favorable system on which dislocation glide can occur. As slip bands activate over the length of the grain, the primary inhibitors to dislocation glide are dislocation networks, secondary phases, or grain boundaries. Alexandreanu *et al.* observed that the energy of grain boundaries is a factor in the ability of matrix dislocations to enter the grain boundaries. These absorption delays resulting from the varying levels of grain boundary energies, affects dislocation mobility within the grain by generating pile-ups (and subsequent backstress) within the grain. It has been proposed that the rate of dislocation absorption is fundamentally that of the rate of dislocation removal or annihilation within the grain boundary[12].

The removal of dislocations can occur via grain boundary vacancy diffusion-facilitated climb over grain boundary obstacles such as ledges, carbides, and/or triple points. It has also been proposed[12] that extrinsic grain boundary dislocations (EGBDs) can be annihilated by interaction with other EGBDs of the opposite sign moving along the same boundary and at triple points. As the structural order of the grain boundaries increase, yielding a reduction in their free volume, dislocation motion becomes more energetically demanding. In other words, as the number of coincident site lattice positions increases (i.e. the closer the grain boundary gets to the order of a perfect crystal), grain boundary free energy decreases, which then increases the activation energy required for grain boundary sliding.

It is widely accepted that grain boundary sliding is both an accommodation and deformation mechanism which produces measurable strain during creep. Grain boundary sliding models have been developed[13]–[16] to predict creep strain rate

based upon the underlying assumption that grain boundary sliding is the dominant deformation process and is proportional to the measured creep strain. Wu and Koul[15] revised a model developed originally established by Langdon[13] to capture the significance that grain boundary microstructure - specifically the presence of $M_{23}C_6$ carbides – has on the creep behavior of nickel-based superalloys. The significance presented by the models offered in References [14] and [15] is that both account for dislocation pile-ups that can occur when obstacles which prevent dislocation glide along the boundaries are encountered. These dislocation pile-ups give rise to backstress which counter the applied stress acting along the grain boundary. This backstress results in a lower effective stress acting along the grain boundary, and in turn, reduces the rate of the creep strain. This holds true so long as the carbides remain discrete[15].

Upon consideration of the above observations, it is proposed here that the grain boundary sliding is motivated and controlled by the amount of intragranular deformation and subsequent release of dislocations into the grain boundaries. As dislocations are released from within the matrix and enter the grain boundary, dislocation glide and climb within the grain boundary must ensue for sliding to occur. A viscous grain boundary can be envisaged, through which a requisite amount of viscoplastic displacement (or sliding) will occur as a function of time, temperature, stress, and microstructure. These factors directly impact the nature of the dislocation kinetics within the grain and grain boundary.

CHAPTER 2

A COUPLED, INTRA- AND INTERGRANULAR MODEL FOR HIGH TEMPERATURE CREEP DEFORMATION OF NICKEL-BASED SUPERALLOY INCONEL 617 – I. MODEL CONCEPTS AND FORMULATION[1,2]

2.1 Abstract

At elevated temperatures and moderate to high stresses, dislocation creep is considered the dominating mechanism of deformation, governed by the motion of dislocations through the matrix and along the grain boundary. Increased activity of matrix dislocations has been observed to accelerate grain boundary sliding at elevated temperatures which is considered here as a function of dislocation arrival rate to the grain boundary. Dislocations that arrive to and are absorbed into the boundary plane can contribute to grain boundary sliding as they glide under shear. Therefore, the rate at which dislocations arrive to the boundary governs the boundaries ability to slide. Precipitation of secondary phases restricts dislocation glide, shifting the rate controlling mechanism from glide to climb.

---

[1] Chapter 2 represents the full manuscript form of that which was submitted to the Journal of the Mechanics and Physics of Solids as:

A Coupled, Intra- and Intergranular Model for High Temperature Creep of Nickel-based Superalloy Inconel 617 – I. Model Concepts and Formulation

M. Lapera, D. Spader, H. Ghonem

[2] Manuscript reference formatting is revised such that it continuous throughout the thesis and shares a common bibliography. Figures, tables, and equations are enumerated to be sequential throughout the thesis.

A physics-based model for creep is presented which considers the mobility of matrix and grain boundary dislocations as they relate to grain boundary sliding during creep. Mobility of dislocations through the matrix and along the grain boundary is modeled as a function of microstructural state – namely carbide size, spacing, and volume fraction. It is considered that grain boundary sliding necessitates a supply of extrinsic dislocations from the matrix which, upon absorption into the grain boundary, glide and subsequently pile-up at irregularities (triple points, carbides, etc.). With increasing number of dislocations in the pile-up, back stress accumulates at the interface, reducing the effective stress and sliding rate. The rate at which dislocations arrive to the grain boundary (a function of climb rate, particle size and spacing within the matrix), therefore, directly influences the sliding rate. Using the model described below, dislocation mobility through the matrix, as it relates to time-dependent microstructural changes, has been simulated and analyzed from which the rate controlling properties of matrix carbides is investigated.

2.2 Introduction

The operating environment of materials used in high temperature applications such as the aerospace and energy generation industries require that they exhibit strength, toughness, and creep resistance. As the demand for greater efficiencies has driven operating environments to higher temperatures and stresses, nickel-based superalloys have become one of the most prevalent families of materials due to their strength at high temperatures. The γ'-precipitate strengthened

nickel-based alloys has proven beneficial in many industrial applications of superalloys through the resulting increases in yield strength seen in low to moderate temperature environments. With increasing service temperatures, the γ' phase also confers creep resistance by acting as a barrier to dislocation motion forcing dislocations to loop, shear, and/or climb, thereby increasing the high temperature strength and prolonging the life of the material. However, at temperatures exceeding ~760°C, the benefits of the phase are lost as the γ' precipitate phase dissolves back into the matrix[17]. In applications at or above the γ' solvus, the most common precipitates found in many nickel-based superalloys are the meta-stable MC and $M_{23}C_6$ carbide formations.

Inconel 617 (IN617), a candidate material for high temperature applications exceeding 900°C, is a solid solution strengthened nickel-based super alloy owing its high temperature strength to misfit strains induced through the addition of elements such as Cr, Mn, Fe, and Co to the FCC Ni matrix. At these elevated temperatures, the solubility of these elements is exceeded within the solid solution resulting in segregation, precipitation, and coarsening of secondary phases in both intra- and intergranular regions. The elements Cr and C often favor the precipitation of carbides of the $M_{23}C_6$ type, which precipitate in a dispersed, discrete fashion in the early stages of creep (early on in the service life exposure). These carbides have been shown to dissolve and re-precipitate within the grain boundary as service time increases. In the grain boundary, these $M_{23}C_6$ carbides can form discrete networks with discernable spacing or continuous slabs which appear as "sheets" of carbides between grains[1],[14].

The creep mechanisms of a crystalline material are generally described in terms of dislocation creep (low temperature, high stress) or diffusional creep (high temperature, low to moderate stress). This difference in mechanism can be explained by the ability for vacancies to diffuse. As the matrix has a relatively high degree of order, dislocation motion along the grain boundaries (Coble creep) becomes the favored mechanism at lower temperatures. This is due to the lower activation energy threshold required for diffusion in the grain boundary, as the misorientation of the grain boundaries presents a larger free volume through which diffusion can occur. As temperatures exceed 0.6-0.7T_m, the vacancies within the matrix increase in their mobility due to the increase in thermal energy; decreasing the energy barrier for self-diffusion within the matrix

Experimental data pertaining to creep of IN617 and similar nickel-based superalloys suggests a synergistic relationship between matrix and grain boundary deformation. Kihara *et al*.[1] examined the creep behavior of IN617 subjected to various heat treatments. In the solution treated condition, carbides were dissolved into the solid solution such that intra- and intergranular regions were denuded of precipitates. This condition allowed for the precipitation of carbides within the matrix to occur during creep deformation. In the aged condition carbides in the matrix, which have already dissolved out in favor of grain boundary carbides, are not available to obstruct dislocation mobility. It was shown that fine, intragranular carbides, which precipitate rapidly during service exposure at 1000°C, suppress creep deformation. The creep data of this alloy showed that for specimens that were only solution treated, the primary (transient) creep rate was noticeably slower than

that of the aged specimens and entered into steady state creep much earlier. The aged specimens exhibited a more classical sigmoidal behavior with a greater primary creep rate.

The work of Chomette *et al.*[9] on the same alloy mentioned above, in both aged and solution treated conditions, further reinforced this difference in primary creep performed at 30 MPa and 950 °C using specimens; the micrographs of the experimental samples taken over the 1 to 1000 hour aging process prior to testing closely resembled the behavior of the specimens tested by Kihara *et al.* Another key observation is that the steady state value of the crept specimens – regardless of the heat treatment procedure – proved to be approximately equal once controlled for the grain size.

Intragranular deformation during creep is associated with activation of slip bands, in which multiple slip systems have become activated and create a favorable system on which dislocation glide would occur. As slip bands are activated over the length of the grain, the primary inhibitors to dislocation glide are dislocation networks, secondary phases, or the grain boundaries. The energy of grain boundaries has been observed to be a factor in the dissociation of matrix dislocations and their subsequent absorption/transmission into and/or through the grain boundaries. These absorption delays resulting from the varying levels of grain boundary energies, affects dislocation mobility within the grain by generating pileups and subsequent backstress within the grain. It has been proposed that the rate of dislocation absorption is that of the rate of dislocation removal, or annihilation, within a characteristic grain boundary length[12]. This removal

process can occur via grain boundary vacancy diffusion-facilitated climb over grain boundary obstacles such as ledges, carbides, and/or triple points. It has also been proposed[12] that extrinsic grain boundary dislocations (EGBDs) can be annihilated by interaction with other EGBDs of the opposite sign moving along the same boundary. As the structural order of the grain boundaries increase, this yields a reduction in free volume encapsulated within the grain boundaries whereby dislocation motion becomes more energetically demanding. In other words, as the number of coincident site lattice positions increases, grain boundary free energy decreases, which then increases the activation energy required for grain boundary sliding.

Carbides found in intragranular and intergranular locations have been observed to control dislocation mobility by shifting the rate controlling process of deformation from dislocation glide to dislocation climb. As dislocations encounter carbides, their ability to glide is halted. In the absence of Orowan looping or particle shearing (given the temperature and stress regime under consideration), for further dislocation glide to continue, dislocations must climb over the particle interface. A dislocation climb is the slower of the two processes (i.e. glide and climb), it is regarded as the rate-controlling deformation mechanism. As such, the size, volume fraction, coherency, and locality of these phases (matrix or grain boundary) have been observed to significantly alter the high temperature mechanical response of this material, particularly in relation to creep deformation facilitated via grain boundary sliding[14],[18]–[23].

The work examined here focuses on describing the concepts and mathematics of a microstructurally sensitive creep model which considers the interaction of matrix and grain boundary dislocations with carbides. This interaction is the basis of determining the overall creep strain in terms of viscous grain boundary sliding.

2.3 Model Overview

Several authors[1],[9],[21] have examined the creep behavior of nickel-based superalloys subjected to various solution treatment and aging processes which result in the presence or absence of intragranular carbides during creep testing. Kihara et al.[1] observed that aging at 1000 °C initially resulted in the precipitation of carbides in the matrix and along grain boundaries. With increasing aging time, however, carbides residing in the matrix eventually gave way to the more stable grain boundary carbides, denuding the matrix of precipitates. The precipitation of these meta-stable carbides within the grain had been considered as the reason for the suppression of strain rate during primary creep at high temperatures for IN617. A model developed by Dyson[19] and expanded upon by Manonukul *et al.*[20] aimed to directly calculate the significance that such intragranular precipitates had on creep strain. Experimental observations were supported by mathematical models which showed γ' precipitates within the matrix effectively slowed the rate of intragranular deformation. It was considered that, by forcing the matrix deformation mechanism to that of dislocation climb by way of presenting obstacles within the matrix, the more effectively dislocation motion was

impeded. Further, the work of Liu and Jonas[24] on alloyed steels showed that the precipitation of titanium carbonitrides during stress relaxation testing was able to significantly slow the relaxation rate of the material.

Soula *et al.*[10] utilized micro-deposited ceramic gridding and micro-extensometry to examine the relationship between the intragranular and intergranular deformation of γ'-strengthened NR6 material. It was shown that the amount of local deformation due to grain boundary sliding events was significantly greater than that which occurs due to matrix deformation (via activation of slip bands) and that the grain boundary sliding deformation was largest in concentrated areas where slip-band/grain boundary incidence was high. The authors observed that the increase in the macroscopic strain magnitude is proportional to the increase in both the number of grain boundary sliding events and slip band generations within the matrix. Prior to reaching the threshold strain of approximately 1%, the rate of increase of intragranular deformation was greater than that of grain boundary sliding events, even though grain boundary sliding displacement dominated. As macroscopic strain increased beyond this strain threshold value, local deformation continued to occur at sites which had already undergone deformation – i.e., grain boundaries where sliding had already taken place and grains which had already experienced crystal slip. The authors have also noted that the localized deformation at the slip band/grain boundary junctions resulted in local deformation that was approximately twice that found elsewhere along the grain boundary under examination and four times that which was found elsewhere within the grain. These observations suggest that the ability for dislocations to move from within the matrix

to the grain boundary play a significant role in the deformation mechanism and resulting strain rate. The work of Fukutomi *et al.*[25] and Sheikh-Ali *et al.*[26] on Cd and Zn bicrystals, respectively, showed the grain boundary sliding rate increased five to ten times when accompanied by crystal slip versus that which occurred in its absence. This is seen in the work of Thibault *et al*.[11] on the same γ'-strengthened NR6 material. In varying the intragranular matrix microstructure by employing the use of different heat treatments, it was shown that the ability of the dislocations to traverse intragranular obstacles during creep testing at 700 °C was directly seen in the magnitude of grain boundary strain which occurred.

Furillo *et al.*[14] investigated the beneficial effects of grain boundary carbides on the creep response of a Nickel-based superalloy. Through conventional creep testing of specimens with and without grain boundary carbides, it was observed that the inclusion of the carbide phase was able to suppress or completely prevent grain boundary sliding. It was concluded that the presence of intergranular carbides provided points for dislocation pile up which generates a backstress resulting in a reduction in the sliding rate of the grain boundary. It was shown by examination of the creep behavior that the presence of grain boundary carbides resulted in an increase in the apparent stress exponent (from ~2 to ~15), which indicated a shift from grain boundary to matrix driven creep. Wu *et al.*[15], modeled grain boundary sliding during transient creep in the presence of grain boundary precipitates through adaptation of Langdon's[13] model with the addition of grain boundary carbides as points of dislocation accumulation.

Grain boundary sliding during stress relaxation is a time and temperature-dependent process motivated by the residual stresses stored in the matrix following elastic deformation. For creep, this process follows an accommodation of a constant stress by way of inelastic straining. In both cases, the motion of dislocations to and along the grain boundary maintains compatibility between adjacent grains and relaxes the shear component of the residual stress tangential to the grain boundary plane. The capability of a grain boundary to slide is considered here as a function of the rate at which matrix dislocations impinge on the grain boundary (where their absorption and subsequent sliding results in measurable displacement between adjacent grains) and the spacing between pinning sites (triple points for clean grain boundaries or particle spacing for decorated grain boundaries), which act as sites for the accumulation of backstress through dislocation pile-up.

The magnitude of grain boundary sliding in nickel-based superalloys at temperatures at or above 0.6-0.7T_m can be shown to be reflective of the hardening and relaxation processes internal to the boundary. The presence of dislocation pile-ups within the boundary hardens the boundary, inhibiting the glide velocity of incoming dislocations along the specific boundary plane. In the presence of discrete grain boundary carbides, the characteristic sliding length, λ_{GB}, is taken to be the value of the carbide spacing. The pinning of dislocations results in the generation of backstress, which is a function of the length of the pile-up that exists at the carbide, as shown in Figure 2.3-1.

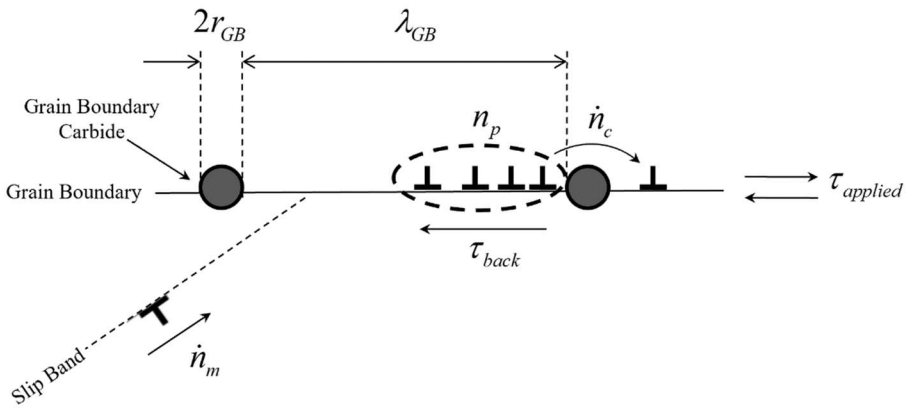

Figure 2.3-1: Pictorial representation of grain boundary absorption of matrix dislocations (n_m), backstress (τ_{back}) accumulation of grain boundary dislocations at discrete grain boundary carbides of spacing λ_{GB}. Dislocations glide in the direction of the applied stress ($\tau_{applied}$). As they approach the carbide, they begin to pile-up, as indicated by the dotted oval. As more dislocations enter the pile-up, the total number (n_p) over a given length generates a backstress which opposes the applied stress and reduces the rate at which trailing dislocations can glide to and enter the pile-up. Dislocations are then only able to escape the pile-up via climbing (n_c) the distance equivalent to that of carbide radius r_{GB}.

Within the existing grain boundary sliding models[13]–[15], the rate-controlling variables in the calculated creep strain rate lies within the backstress term as a result of dislocation pile-up in front of grain boundary carbides and the rate of dislocation climb over them. These models indicate that the transition from primary to steady state creep is achieved when the backstress due to dislocation pile-up[15] reaches a maximum, which is the result of the number of mobile grain boundary dislocations within a fixed volume of the boundary reaching an equilibrium value. Consequently, this would suggest that steady state sliding can be thought of as the result of the grain boundaries being fully "saturated" with dislocations; only able to accommodate new incoming dislocations from the matrix when an equal number

within the grain boundaries have been annihilated or have climbed over the obstacle (e.g. grain boundary carbide, triple point, etc.). Lin and McLean[27] have suggested that while it is possible that dislocations are generated within the grain boundaries, it is likely that the primary source of the increase in extrinsic grain boundary dislocations is due to absorption of lattice dislocations into the grain boundaries. The concept of a "saturated" grain boundary due to matrix dislocation absorption is reinforced by the work of Pshenichnyuk *et al.*[28]. This population is a function of the lattice dislocations which are absorbed by the grain boundary and rendered as glissile grain boundary dislocations.

Matrix dislocations, upon entrance into the grain boundaries, will either be transmitted through or dissociate within the grain boundaries[6],[11]. As the slip band spacing generated during creep is presumed to be significantly larger than that which is produced in fatigue applications, the lack of adjacent grain slip system symmetry makes transmission difficult[7], and therefore is not considered in the model presented herein. If a dislocation is absorbed and not instantly locked (i.e. the dissociation produces a glissile component), there are two different dislocation-dislocation interactions which will ensue[26],[29]. In the case of dislocations of the opposite sign, they result in micro-incompatibility which produces localized grain boundary sliding, that could then resolve itself, resulting in no measurable strain. On the other hand, dislocations of the same sign could produce incompatibility resulting in a measurable grain boundary sliding. The entry points and density of dislocations introduced into the grain boundary is a factor of adjacent grain orientation (slip band alignment and spacing) and grain boundary energy (typically

characterized by the CSL boundary values)[6],[13]. The number of glissile grain boundary dislocations contained within the boundary has been described as being inversely proportional to the boundary viscosity. This viscosity, η_B, and its relationship to dislocation density, was first proposed by Ashby[30] and takes the form of:

$$\eta_B = \frac{kT}{8bD_b(N\lambda_{GB})} \qquad [2.3\text{-}1]$$

where k is Boltzmann's constant, T is the exposure temperature (Kelvin), b is the Burgers vector, D_b is the grain boundary diffusion coefficient, N is the linear density of extrinsic dislocations within the grain boundary, and λ_{GB} is the grain boundary length.

As the grain boundary viscosity is inversely proportional to the extrinsic grain boundary dislocation density[30] for a given sliding rate, the dislocations must travel faster within a smaller population and therefore the energy required for their motion increases as a function of their velocity squared. Therefore, the sliding rate of the grain boundary can be considered a time dependent parameter based upon the rate at which matrix dislocations are absorbed into the grain boundary and the rate at which the glissile components can slide. As such, rate controlling obstacles (i.e. carbides) in the matrix must also been taken into account when considering the overall grain boundary sliding rate.

As described above, grain boundary sliding and the rate at which it occurs is dependent on dislocation mobility within the grain and along the boundary. Of

particular interest in the current work is how the size and volume fraction of intra- and intergranular carbides affect the overall grain boundary sliding rate. To accomplish this, a microstructurally sensitive, viscous grain boundary sliding model has been developed which considers the rate of dislocation glide and pile up along the boundary as a function of the supply rate of dislocations from the matrix. This model is described in the following section.

2.4 Model Physics

2.4.1 Cohesive Zone Approach for Modeling of the Grain – Grain Boundary Interface

To model the grain boundary sliding process, a cohesive zone model which considers viscous sliding will be utilized. A physical analog to the relationship of the grain and grain boundary deformation is an adaptation of Maxwell's standard linear solid model of viscoelasticity. This configuration consists of a Hookean spring and Newtonian dashpot connected in parallel, joined in series with a Hookean spring, as shown in Figure 2.4-1.

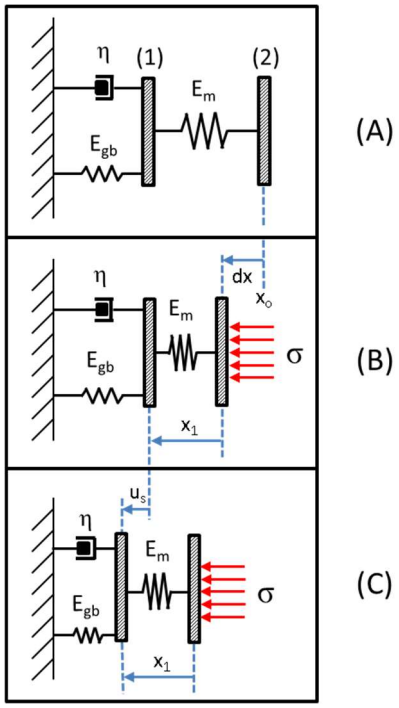

Figure 2.4-1: (A) The grain and grain boundary visualized as a network of springs and a Newtonian dashpot under the zero-stress condition. Interface (1) represents the grain boundary/matrix interface and interface (2) represents the matrix with the external surface. (B) Stress is applied to interface (2), deforming the assembly from x_o by dx. The initial loading elastically deforms the matrix. The elastic load results in a distance of x_1 between interfaces (1) and (2), which remains constant throughout the application of the load. (C) Continued displacement of interfaces (1) and (2) to the left is facilitated via interface (1) which represents the grain boundary sliding displacement, u_s.

In Figure 2.4-1.A, interface (1) represents the grain boundary and matrix interface and interface (2) represents the interface between matrix and the external surface when the external stress is applied. In Figure 2.4-1.B stress is applied to interface (2), deforming the assembly from x_0 by dx. The initial loading elastically deforms the matrix resulting in a distance of x1 between interfaces (1) and (2), which remains constant throughout the application of the load. In Figure 2.4-1.B, the continued displacement of interfaces (1) and (2) to the left is facilitated via

interface (1), which represents the grain boundary sliding displacement, u_s .The assembly shown in Figure 2.4-2 provides an alternative method for visualization of Figure 2.4-1 within the context of a matrix – grain boundary interface.

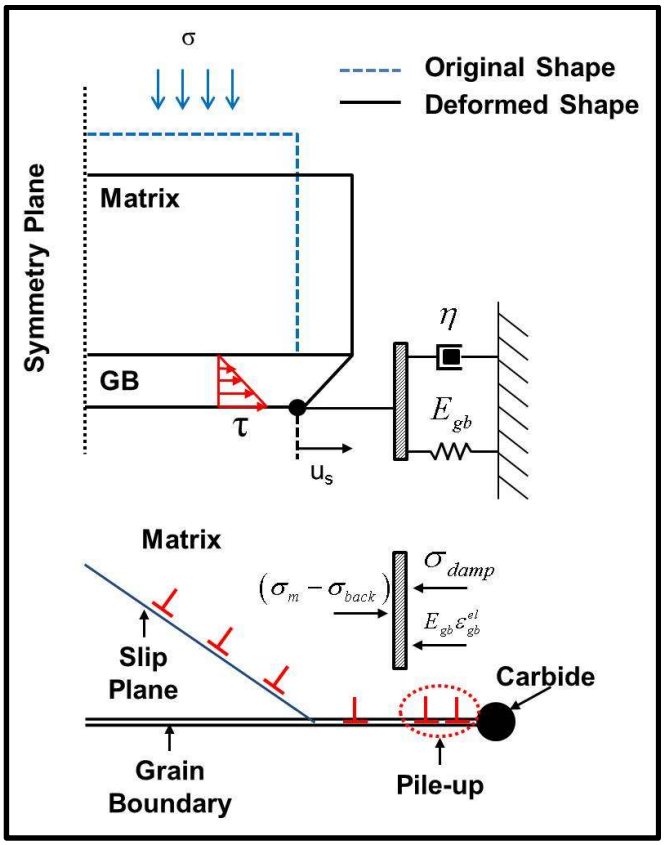

Figure 2.4-2: Representation of Maxwell's standard linear solid model of viscoelasticity for use in a cohesive zone formulation. Application of stress to the matrix results in a resolved shear stress along the grain boundary which results in grain boundary sliding, u_s.

In Figure 2.4-2, the applied stress results in the elastic displacement of the matrix and a resolved shear stress along the boundary plane; inversely proportional to the separation distance (or width of the grain boundary), δ , approximated by the

value of a single Burgers vector. The sliding velocity, $\dot{u}_s$, of the above assembly is then considered as:

$$\tau = \frac{\eta}{\delta}\dot{u}_s = \frac{\eta}{b}\dot{u}_s \qquad [2.4\text{-}1]$$

The cohesive zone relies on the elastic traction-displacement law applied at the matrix and grain boundary interface, and is described by[4]:

$$T = K_{gb}u_{gb}^{el} \qquad [2.4\text{-}2]$$

where T is the tangential traction K_{gb} is the boundary stiffness, and u_{gb}^{el} is the elastic displacement of the grain boundary. The elastic displacement is defined as:

$$u_{gb}^{el} = u_{gb}^{total} - u_s \qquad [2.4\text{-}3]$$

where u_{gb}^{total} is the total elastic displacement and inelastic displacement, u_s, is the time-dependent displacement resulting from grain boundary sliding. To account for the role of backstress affecting the grain boundary sliding rate, $\dot{u}_s$, the term T in Eq. [2.4-2] is defined as:

$$T = T_{net} = T_{app} - T_{back} \qquad [2.4\text{-}4]$$

where T_{app} is the applied traction (generated by the applied load) and T_{back} is the opposing force due to the accumulation of backstress. This produces a net traction, T_{net}.

2.4.2 Grain Boundary Backstress

From Wu *et. al*[15], the backstress exerted on a moving dislocation a distance x from the particle is given by:

$$\tau_{back}(x) = \frac{n_p E_{GB} b}{2\pi(1-\nu)x} \qquad [2.4\text{-}5]$$

where n_p is the number of dislocations in the pile-up, ν is Poisson's ratio, E_{GB} is the shear modulus of the grain boundary, and b is the Burgers vector. For a dislocation to glide over the total distance between two carbides, the applied work ($\tau\lambda$) must be greater than the resistance due to backstress. This is calculated through the integration of Eq. [2.4-5]:

$$\tau\lambda \geq \int_{n_p b}^{\lambda} \tau_{back}(x)dx \qquad [2.4\text{-}6]$$

Dividing both sides of Eq. [2.4-6] by λ (approximated as the grain boundary carbide spacing) yields the average backstress between two carbides:

$$\tau_{back}^{avg} = \frac{1}{\lambda}\int_{n_p b}^{\lambda} \tau_{back}(x)dx \qquad [2.4\text{-}7]$$

Integrating over the boundary domain provides the final form for the average backstress opposing dislocation glide between two discrete grain boundary carbides of spacing λ (referred to as λ_{GB} herein):

$$\tau_{back}^{avg} = \frac{n_p E_{GB} b}{2\pi(1-\upsilon)\lambda_{GB}} \ln\left(\frac{\lambda_{GB}}{n_p b}\right) \qquad [2.4\text{-}8]$$

Eq. [2.4-8] shows that the backstress increases proportionally with the number of dislocations in the pile-up. In the presence of dislocation climb, the rate of change of the number of dislocations in the pile-up can be envisioned as a flow balance, which considers the number of dislocations arriving to the pile-up reduced by the number of dislocations climbing over the carbide.

$$\frac{dn_p}{dt} = \rho_{gb} v_{g,gb} \lambda_{GB} - n_p \frac{1}{t_c} \qquad [2.4\text{-}9]$$

In Eq. [2.4-9], $v_{g,gb}$ is the grain boundary dislocation glide velocity, t_c is the relaxation time, and ρ_{gb} is the glissile dislocation density (number per unit area). The relaxation time is that which is required for a dislocation to climb over a grain boundary carbide of height, r_{GB}, and can be described as:

$$t_c = \frac{r_{GB}}{v_{c,gb}} \qquad [2.4\text{-}10]$$

where v_c is the grain boundary dislocation climb velocity and is written as function of the grain boundary diffusion coefficient (D_{gb}), applied stress acting normal to the grain boundary (σ_n), Burgers vector (b), temperature (T), Boltzmann's constant (k) and grain boundary carbide radius (r_{GB})[31]:

$$v_{c,gb} = \frac{D_{gb}}{r_{GB}} \left[\exp\left(\frac{\sigma_n b^3}{kT} \right) - 1 \right] \qquad [2.4\text{-}11]$$

The dislocation glide velocity in Eq. [2.4-9] described by Hull and Bacon [32] as:

$$v_{g,gb} = M_d b \tau_{net} \quad [2.4\text{-}12]$$

where M_d is used to describe a dislocation's mobility within the grain boundary (approximately equal to $\frac{D_{GB}}{kT}$), and τ_{net} is the net (effective) shear stress acting along the grain boundary and is the difference between the resolved applied shear stress and the backstress which is calculated from Eq. [2.4-8]. Substituting Eqs. [2.4-10] - [2.4-12] into Eq. [2.4-9] yields:

$$\frac{dn_p}{dt} = \rho_{gb} M_d b \lambda_{GB} \tau_{net} - n_p \frac{D_{gb}}{r_{GB}^2}\left[\exp\left(\frac{\sigma_n b^3}{kT}\right) - 1\right] \quad [2.4\text{-}13]$$

To consider the number of dislocations, n_{gb}, the density, ρ_{gb}, is divided by the square of the carbide spacing:

$$\rho_{gb} = \frac{n_{gb}}{\lambda_{GB}^2} \quad [2.4\text{-}14]$$

resulting in the expression for the rate of change of dislocations in the pile-up as:

$$\frac{dn_p}{dt} = n_{gb} \frac{M_d b}{\lambda_{GB}} \tau_{net} - n_p \frac{D_{gb}}{r_{GB}^2}\left[\exp\left(\frac{\sigma_n b^3}{kT}\right) - 1\right] \quad [2.4\text{-}15]$$

As mentioned previously, the number of dislocations in the grain boundary, n_{gb}, is considered here to be equal to the number of dislocations which have arrived to and been absorbed by the grain boundary, n_m.

2.4.3 Matrix Deformation and Dislocation Availability (n_m)

Within a deforming matrix, consider the two populations of dislocations – mobile (gliding) and immobile (pinned). The pinning refers to the fraction of the total population which will be rendered immobile by the carbides at any given time. The rate of change of the gliding dislocation density within the matrix, $\dot{\rho}_g$, is expressed as the sum of the rate of dislocations which are able to successfully climb over the carbides pinning them plus the rate of dislocation generation via multiplication minus the rate of mobile dislocations which get trapped at carbides. This is written as:

$$\dot{\rho}_g = \rho_c x_c \dot{r}_c - \rho_g x_g \dot{r}_g + \dot{Q}_g \qquad [2.4\text{-}16]$$

where ρ_c is the instantaneous density of pinned dislocations, x_c is the probability that a pinned dislocation will escape via climb, $\dot{r}_c$ is the climb rate, ρ_g is the instantaneous density of mobile dislocations, x_g is the probability that a mobile dislocation will become pinned by encountering a carbide (taken as unity), $\dot{r}_g$ is the dislocation pinning rate, and $\dot{Q}_g$ is the generation rate of mobile dislocations.

Similar to the work of Dyson[19], it is assumed that the population of mobile gliding dislocations saturates rapidly due to the presence of matrix carbides, thereby driving the left hand term of Eq. [2.4-16], $\dot{\rho}_g$, rapidly to zero. Additionally, the dislocation generation term, $\dot{Q}_g$, is assumed to be orders of magnitude smaller

than the remaining terms in Eq. [2.4-16] and is neglected [33]. The two assumptions above simplify Eq. [2.4-16] to:

$$\rho_c x_c \dot{r}_c = \rho_g x_g \dot{r}_g \qquad [2.4\text{-}17]$$

The probability that a pinned dislocation is able to climb over a particle, x_c, is considered proportional to the product of the dislocation line length in contact with the particle (approximated as the volume fraction, ϕ_p) and Burgers vector, b, and inversely proportional to the particle size, r_p. Therefore, x_c, can be approximated as[33]:

$$x_c = \frac{\phi_p b}{r_p} \qquad [2.4\text{-}18]$$

The rate of dislocation escape via climb over precipitates, $\dot{r}_c$, is the ratio of dislocation climb velocity, v_c, to Burgers vector, b:

$$\dot{r}_c = \frac{v_c}{b} \qquad [2.4\text{-}19]$$

The rate of the dislocation pinning, $\dot{r}_g$, is the ratio of the dislocation glide velocity, v_g, with respect to the average matrix carbide spacing, λ_p:

$$\dot{r}_g = \frac{v_g}{\lambda_p} \qquad [2.4\text{-}20]$$

The spacing, λ_p, is for the case of a square lattice of equally spaced spherical particles of radius r_p, and is expressed as[19]:

$$\lambda_p = 1.6 r_p \left[\left(\frac{\pi}{4\phi_p} \right)^{1/2} - 1 \right] \quad [2.4\text{-}21]$$

Substituting Eqs. [2.4-18] - [2.4-20] into Eq. [2.4-17] yields:

$$\rho_{\mathrm{c}} \frac{\phi_p}{r_p} v_c = \rho_{\mathrm{g}} \frac{v_g}{\lambda_p} \quad [2.4\text{-}22]$$

Considering that the dislocation population contributing to strain generation is the sum of the gliding and climbing dislocations, the shear strain rate of the matrix, $\dot{\gamma}_m$, can be written as a modified form of Orowan's relationship:

$$\dot{\gamma}_m = b(\rho_{\mathrm{g}} v_g + \rho_c v_{\mathrm{c}}) \quad [2.4\text{-}23]$$

As the dislocation glide velocity is significantly larger than that of the climb velocity, it can subsequently be regarded as insignificant, allowing Eq. [2.4-23] to be rewritten:

$$\dot{\gamma}_m \approx \rho_{\mathrm{c}} \frac{\phi_p}{r_p} b \lambda_p v_c \quad [2.4\text{-}24]$$

When considering a matrix containing precipitates, the total dislocation density, ρ, can be decomposed as follows[33]:

$$\rho_{\mathrm{m}} = \left(1 - \phi_{\mathrm{p}}\right) \rho = \rho_{\mathrm{g}} + \rho_c \quad [2.4\text{-}25]$$

where ρ_m is taken to be the mobile dislocation density within the matrix. The shear strain rate of the matrix and rate of change of the total dislocation density, $\dot{\rho}$, are related to one another. The general relationship presented in Eq. [2.4-26] and initial

dislocation density, ρ_0, with a value of $10^{10}\,\frac{1}{m^2}$ will be used. This initial dislocation density value is consistent with other nickel-based superalloys dislocation evolution descriptions found in literature[19],[20]:

$$\dot{\rho} = \alpha \rho_0 \dot{\gamma}_m \qquad [2.4\text{-}26]$$

where α is a material constant. In Eq. [2.4-24], the climb velocity of an edge dislocation is approximated by Friedel's relationship[18],[33]:

$$v_c = \frac{D_c}{b} \sinh\left(\frac{\hat{\tau} b^2 \lambda_p}{kT}\right) \qquad [2.4\text{-}27]$$

where D_c is the diffusion coefficient for self-diffusion, $\hat{\tau}$ is the average shear stress acting within the matrix, k is Boltzmann's constant, and T is temperature (Kelvin). The diffusion coefficient can be expressed in terms of the activation energy for glide and climb, $Q_{comb}\,(\approx Gb^3)$[20] and the universal gas constant, R:

$$D_c = D_{c,0} e^{\frac{-Q_{\text{comb}}}{RT}} \qquad [2.4\text{-}28]$$

From inspection of Eq. [2.4-24], it can be seen that as the particle spacing decreases the number of dislocation-carbide interactions which require climb increases, in turn slowing down the rate of deformation of the crystal. The mobile dislocation density within the matrix, ρ_m, ignores the much smaller density of gliding dislocations described in Eq. [2.4-25] and similar to Shirzadi[33], is subsequently taken to be equal to that of the climbing dislocation density:

$$\rho_m \cong \rho_c \qquad [2.4\text{-}29]$$

Substituting Eqs. [2.4-21], [2.4-25], [2.4-27], and [2.4-29] into Eq. [2.4-24] shows:

$$\dot{\gamma}_m = 1.6\alpha\rho\phi_p\left(1-\phi_p\right)\left[\left(\frac{\pi}{4\phi_p}\right)^{1/2}-1\right]D_c \sinh\left(\frac{\hat{\tau}b^2\lambda_p}{kT}\right) \qquad [2.4\text{-}30]$$

The matrix dislocation density in Eq. [2.4-26] shows an explicit dependence on the matrix shear strain rate. This is treated by substituting Eq. [2.4-15] into Eq. [2.4-24], thereby forming a set of ordinary differential equations (ODEs) shown below in Eq. [2.4-31].

$$\begin{cases} \dot{\gamma}_m = 1.6\alpha\rho\phi_p\left(1-\phi_p\right)\left[\left(\frac{\pi}{4\phi_p}\right)^{1/2}-1\right]D_c \sinh\left(\frac{\hat{\tau}b^2\lambda_p}{kT}\right) \\ \dot{\rho} = \left(\frac{1}{1.6\alpha}\right)\rho_0\dot{\gamma}_m \end{cases} \qquad [2.4\text{-}31]$$

It is with this set of equations that the rate of matrix strain, as well as the matrix dislocation density, can be calculated as functions of the applied stress, carbide volume fraction and carbide spacing, and time. Using Orowan's relationship, given that the rate-controlling process is dislocation climb, the number of available dislocations which can contribute to grain boundary sliding, n_m, as a function of time, can be determined by integrating Eq. [2.4-19]:

$$n_m = \int_{t_i}^{t_{i+1}} \frac{v_c}{b}\,dt \qquad [2.4\text{-}32]$$

In the above equation, the dislocation climb velocity, v_c, is obtained by rearranging Eq. [2.4-24]. The number of dislocations "released" from the matrix (i.e. able to contribute to grain boundary sliding) is a fraction of the maximum dislocation population, ρ. There is an underlying assumption within the matrix deformation model that the entire dislocation density population, as it evolves in accordance with Eq. [2.4-26], is able to participate in the glide-climb succession. With this assumption, a material constant, β, is introduced for model adjustment purposes. When Eq. [2.4-24] and [2.4-25] are substituted into Eq. [2.4-32], this produces Eq. [2.4-32] in the following form:

$$\dot{n}_m = \frac{\dot{\gamma}_m r_p}{\beta b^2 \phi_p (1-\phi_p) \rho \lambda_p} \qquad [2.4\text{-}33]$$

The number of dislocations which become available for grain boundary sliding, n_m, can then be regarded as the n_{gb} term in Eq. [2.4-15], acting as the incoming dislocation population which contributes to the pile-up. The greater the value of this term, the greater the rate of change of the pile-up, as dislocation climb is regarded as time-independent. It is also important to realize that the rate of pile-up growth and backstress generation will ultimately be affected by the characteristic length over which sliding occurs (e.g. grain boundary carbide spacing, grain boundary length, etc.) and grain boundary viscosity. As Ashby[30] identifies, this is due to the fact that the grain boundary has a saturation limit of (λ_p/b).

2.5 Intragranular Dislocation Mobility

The model framework presented in the previous section was used to determine what effects the matrix carbide radius and volume fraction had on the number and rate of dislocations which are able to escape the grain interior and be absorbed by the grain boundary. This was accomplished by running the matrix deformation model (uncoupled to the grain boundary deformation model) in a simulated creep environment of a 24.5 MPa constant stress and exposure temperature of 1000 °C with varying time profiles of radius and volume fraction, This was accomplished by running the matrix deformation model (uncoupled to the grain boundary deformation model) in a simulated creep environment of a 24.5 MPa constant stress and exposure temperature of 1000 °C with varying time profiles of radius and volume fraction, as shown in Figure 2.5-1 – Figure 2.5-4. These stress and temperature values were chosen such that they were similar to those studied by Kihara *et al.*[1]. The radius and volume fraction time profiles, Conditions 1-3 and Conditions 1a-1c, as shown in Figure 2.5-1 – Figure 2.5-4, were then used to examine the effects of the rate of change and magnitude of both the matrix carbide radius and volume fraction on intragranular dislocation mobility.

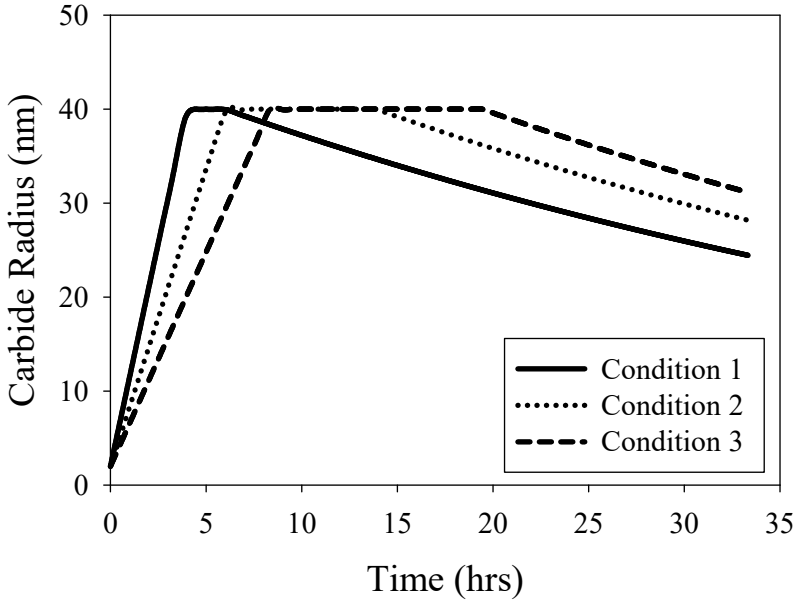

Figure 2.5-1: Theoretical matrix carbide radius profiles showing three distinct microstructural evolution conditions. The three distinct regimes aim to capture the carbide growth, coarsening, and dissolution phases.

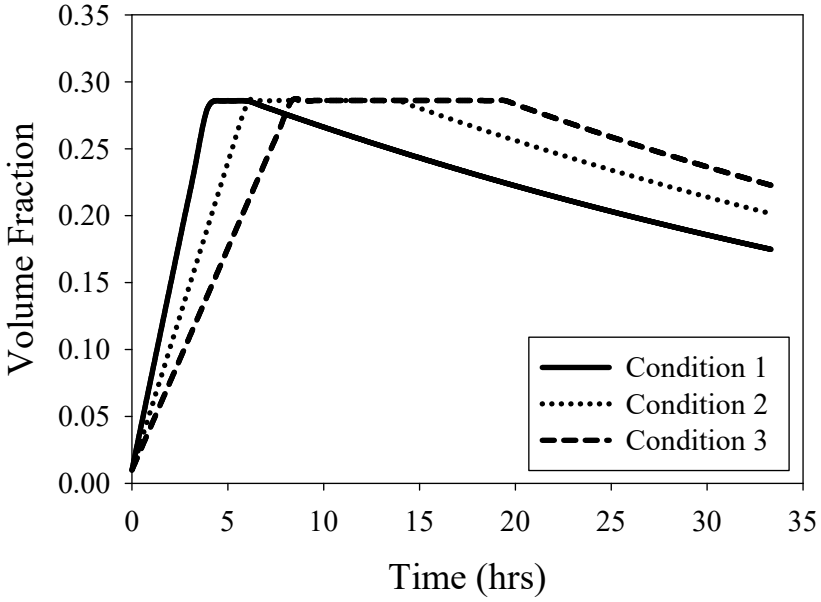

Figure 2.5-2: Theoretical matrix carbide volume fraction profiles showing three distinct microstructural evolution conditions. The three distinct regimes aim to capture the carbide growth, coarsening, and dissolution phases. For Conditions 1, 2, and 3, an approximate saturation value for the carbide volume fraction is 0.286, which was established via image analysis of the micrographs produced in the work of Kihara *et al.*[1].

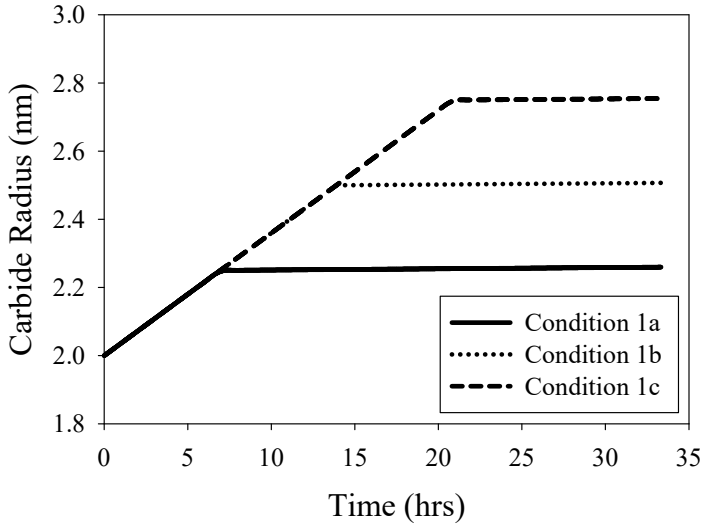

Figure 2.5-3: Theoretical matrix carbide radius profiles showing three distinct microstructural evolution conditions. The three distinct regimes aim to capture the carbide growth, coarsening, and dissolution phases. Conditions 1a, 1b, and 1c are derived from Condition 1, but maintain a constant carbide growth rate in order to elucidate the significance of the growth duration, ultimate carbide size, and volume fraction attained prior to coarsening.

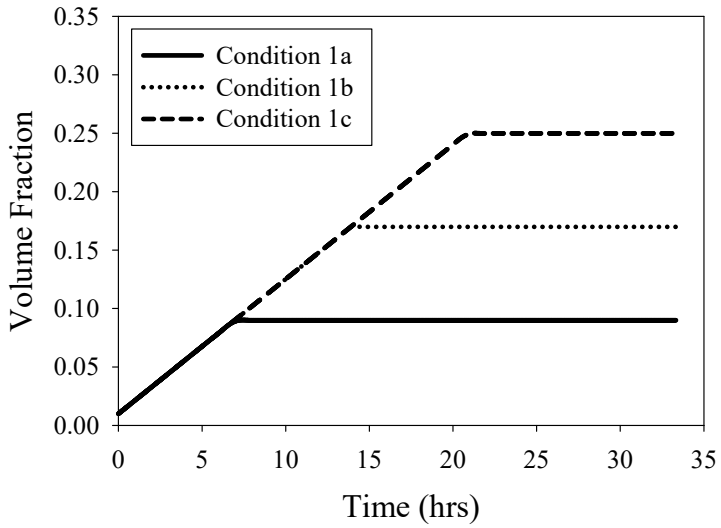

Figure 2.5-4: Theoretical matrix carbide radius profiles showing three distinct microstructural evolution conditions. The three distinct regimes aim to capture the carbide growth, coarsening, and dissolution phases. Conditions 1a, 1b, and 1c are derived from Condition 1, but maintain a constant carbide growth rate in order to elucidate the significance of the growth duration, ultimate carbide size, and volume fraction attained prior to coarsening.

The number of dislocations released for Conditions 1-3 and Conditions 1a-1c are presented in Figure 2.5-5 and Figure 2.5-6, respectively, as the ratio of dislocations released from the matrix with respect to the increase of mobile dislocations within the matrix.

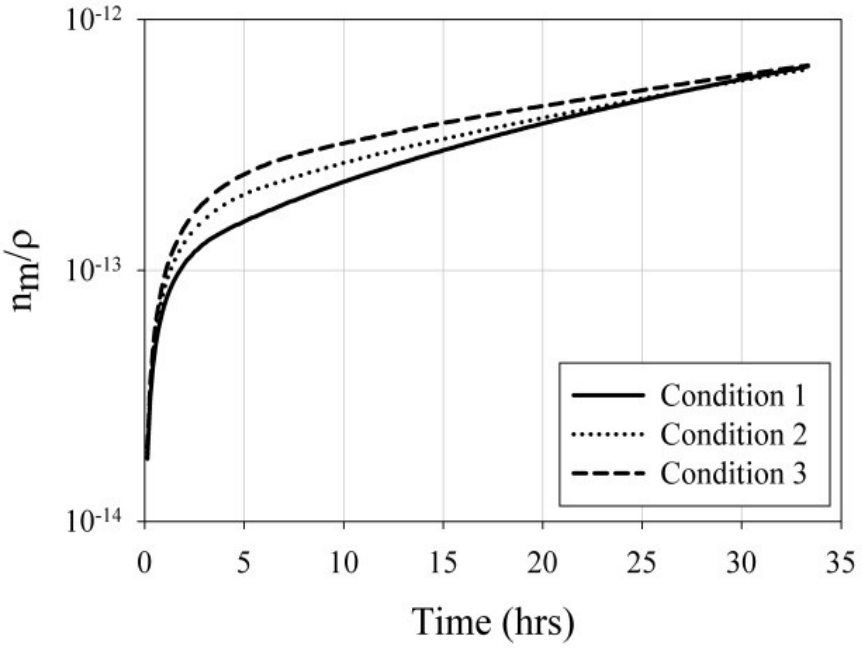

Figure 2.5-5: A preliminary study of the number of dislocations (scaled by the number of mobile matrix dislocations) which are available for entry into the grain boundaries (shown above) simulated for 24.5 MPa at 1000°C. The behavior is proportional with the predicted matrix strain magnitude and mobile dislocation production seen in each theoretical condition examined by Conditions 1-3.

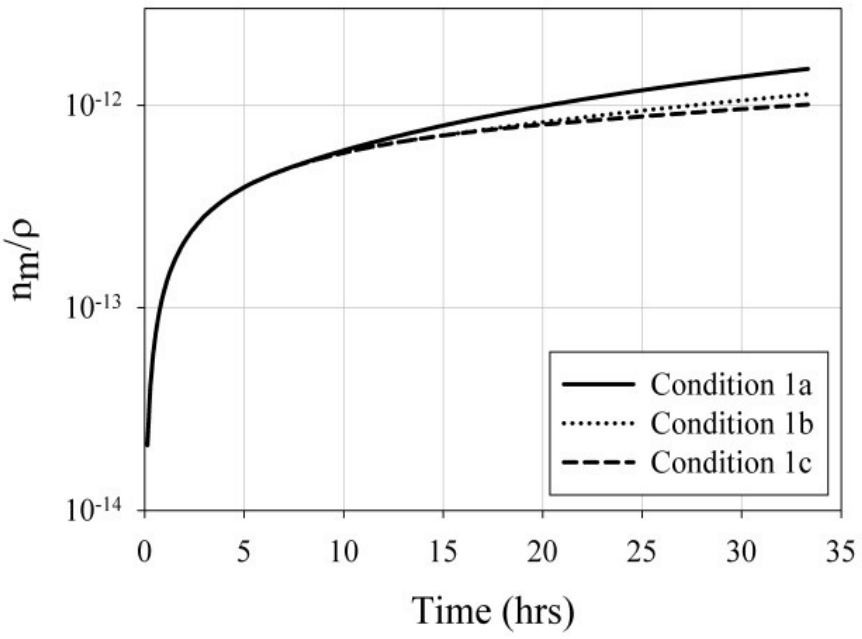

Figure 2.5-6: A preliminary study of the number of dislocations (scaled by the number of mobile matrix dislocations) which are available for entry into the grain boundaries (shown above) simulated for 24.5 MPa at 1000°C. The behavior is proportional with the predicted matrix strain magnitude and mobile dislocation production seen in each theoretical condition examined by Conditions 1a-1c.

To characterize the effect of the inextricably related matrix carbide radius (r_p) and volume fraction (ϕ_p), the spacing (λ_p) was calculated using Eq. [2.4-21] assuming a square lattice array of uniformly spaced particles[19]. The resulting matrix carbide spacing values for the Condition 1a, 1b, and 1c carbide evolution profiles are then plotted on the secondary y-axis against time alongside the values of n_m in shown in Figure 2.5-7.

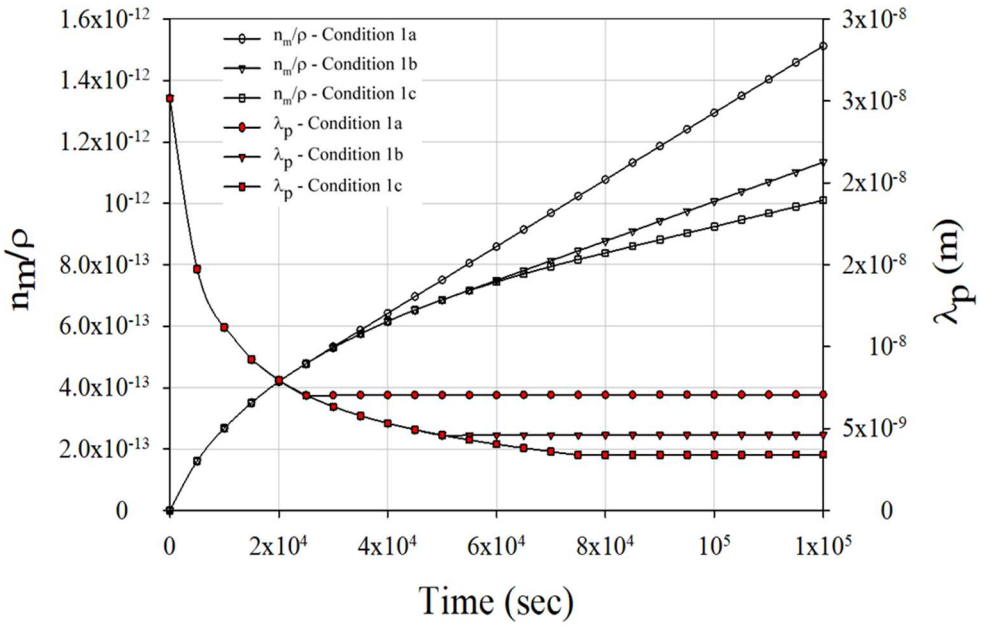

Figure 2.5-7: The matrix carbide spacing was calculated as a function of time and plotted alongside the number of matrix dislocations which are able to be absorbed by the grain boundaries at a stress of 24.5 MPa and 1000 °C. Conditions 1a, 1b, and 1c were chosen to be plotted against spacing values as the radius growth rates and volume fraction rates were maintained constant in these conditions, which is assumed to be reflective of the identical microstructure evolution of three specimens of the same material exposed to the same temperature for different aging durations.

It can be seen in Figure 2.5-7 that there is a distinct relationship between the stabilization of the matrix carbide spacing and the transient regime of the dislocation release rate. In other words, as the carbide spacing term approaches a slope of zero (the onset of which is a feature of the coarsening regime of the carbide evolution), the rate of change of the dislocations being released slows to a constant rate. For Conditions 1a, 1b, and 1c shown in Figure 2.5-7, this occurs at approximately 7 hours, 14 hours, and 21 hours, respectively. The longer the spacing term takes to stabilize – in this case, the longer the carbide growth phase – the lower

the subsequent steady state rate of matrix dislocation release. This observation also aligns with the trend seen in the final/saturation value of the carbide spacing insofar as the minimum calculated spacing value is accompanied by the slowest steady state dislocation release rate. In the case of these simulations, if the growth phase of the carbide precipitation could be extended such that it exhibited a lesser exponential decay constant, Figure 2.5-7 suggests that a much slower steady state matrix dislocation release rate could be achieved.

When considering the amount and rate of dislocation release from the matrix as a function of intragranular carbide spacing and the increased rate of stress relaxation seen in material with increasingly large carbide spacing, it can be seen that the simulation results agree with the conclusions in the work of Balantic *et al.*[18] where an increase in carbide spacing resulted in a greater steady state creep rate. This is realized upon examination of Figure 2.5-7, whereby increases in the carbide spacing term are accompanied by an increase in the steady state matrix dislocation release rate.

2.6 Conclusions

A physically-based, microstructurally-sensitive, model of grain boundary sliding has been developed. The inelastic sliding rate of the grain boundary has been described as a function of dislocation mobility through the matrix and along the grain boundary. Carbides that reside within the matrix and along the grain boundary have been shown to suppress deformation rate at elevated temperatures where both dislocation glide and/or climb are active. As deformation in the matrix

requires accommodation through grain boundary sliding which, in turn, requires a supply of extrinsic dislocations from the matrix, a model which captures the combined role of matrix and grain boundary has been developed.

The presented model aims to demonstrate the concept that matrix carbides reduce the number of dislocations which are able to arrive to and be absorbed by the grain boundary, effectively limiting the rate at which the grain boundary can slide. Dislocations, once absorbed into the grain boundary, undergo a glide and climb sequence to accommodate the initial elastic deformation of the grain. As dislocations glide along the boundary, carbides impede their motion, and produce dislocation pile-ups which generate backstress. As the magnitude of backstress increases, the driving force for dislocation glide along the boundary decreases until a steady state condition is reached. Steady state creep is considered as the balance between the rate at which dislocations enter the pile-up (hardening) and the rate at which dislocations climb out of the pile-up (recovery). As grain boundary sliding is facilitated by the gliding of extrinsic dislocations, the rate of increase in the pile-up along the grain boundary is dependent on the rate at which dislocations arrive to the grain boundary. Preliminary simulations of dislocation mobility through the matrix, using time-dependent microstructural changes (carbide size, spacing, volume fraction), identify spacing as the rate controlling microstructural feature for dislocation release rate from the matrix.

In Part II of this two-part paper, a series of aging and stress relaxation experiments on IN617 have been conducted which provide data for the above model to be analyzed. Aging at 1000°C for varying durations of time is used as a

means of producing unique microstructures from which matrix and grain boundary carbide characteristics (size and volume fraction) are measured. Following aging, stress relaxation tests are conducted at 200 MPa and 780°C such that diffusional effects, as well as microstructural changes, are suppressed throughout the duration of the accelerated type creep test. A constant microstructure permits a more direct analysis of the rate controlling properties of the matrix and grain boundary carbides on grain boundary sliding. Using the methodology presented above, stress relaxation data in conjunction with microstructural analysis will be used as input into the matrix and grain boundary sliding models, from which the rate controlling properties of matrix carbides on grain boundary sliding can be investigated.

CHAPTER 3

A COUPLED, INTRA- AND INTERGRANULAR MODEL FOR HIGH TEMPERATURE CREEP DEFORMATION OF NICKEL-BASED SUPERALLOY INCONEL 617 – II. EXPERIMENTAL RESULTS AND MODEL APPLICATION[3,4]

3.1 Abstract

Aging and stress relaxation experiments have been conducted on the nickel-based superalloy, Inconel 617, to investigate the role of intragranular and intergranular carbides on grain boundary sliding. All specimens were solutioned for 2 hrs at 1200°C and water quenched prior to testing to dissolve remaining secondary phases. Following solutioning, aging at 1000°C for increasing durations produced unique microstructural parameters of carbide size, spacing, and volume fraction within the grain and along the grain boundary. Carbide size, spacing, and volume fraction were all observed to increase with duration up to 30 hours of aging. Stress relaxation tests at 780°C with an initial stress of 200 MPa were then conducted on the aged specimens to analytically model the rate controlling properties of matrix and grain boundary carbides as they pertain to grain boundary

[3] Chapter 3 represents the full manuscript form of that which was submitted to the Journal of the Mechanics and Physics of Solids as:

A Coupled, Intra- and Intergranular Model for High Temperature Creep of Nickel-based Superalloy Inconel 617 – II. Experimental Results and Model Application

D. Spader, M. Lapera, H. Ghonem

[4] Manuscript reference formatting is revised such that it continuous throughout the thesis and shares a common bibliography. Figures, tables, and equations are enumerated to be sequential throughout the thesis.

sliding. Relaxation rate of Inconel 617 drastically decreased after aging at 1000°C for 3 hours with little variation in relaxation rate up to 30 hours of aging prior to testing.

It is considered that grain boundary sliding necessitates a supply of extrinsic dislocations that are released from the matrix during creep. As carbides act as obstacles to dislocation motion, their presence in the matrix suppresses the rate at which dislocations can arrive to the boundary to facilitate grain boundary sliding. Carbides along the grain boundary act as obstacles and provide points of dislocation accumulation resulting the generation of back stress. The rate of accumulation is therefore considered the mechanism in which steady state is achieved. Stress relaxation tests were used to identify model parameters, as discussed in Reference [35], to simulate dislocation mobility within the grain and along the grain boundary.

3.2 Introduction

The relationship between intragranular slip and grain boundary sliding were first discussed in the works of Langdon[13], McLean and Lin[27], Ishida and Henderson[36], and Hirth[7]. It was observed that the population of grain boundary dislocations increased significantly with strain[36] which was attributed to the absorption of extrinsic matrix dislocations into the grain boundary[12],[27]. The magnitude of grain boundary sliding was observed to increase with increasing slip activity in the matrix[10]. It has been suggested that grain boundary sliding, facilitated by dislocation glide, necessitates the absorption of extrinsic matrix dislocations, which subsequently glide along the boundary plane[12],[26],[28],

[34]. The rate of dislocation arrival to and along the grain boundary is suppressed through the precipitation of carbides which act as obstacles, changing the rate controlling mechanism of deformation from dislocation glide to dislocation climb[13],[14],[18],[19].

In Part I of this paper[35], the rate at which dislocations arrive to the grain boundary from the matrix, $\dot{n}_m$, has been described as:

$$\dot{n}_m = \frac{\dot{\gamma}_m r_p}{\beta b^2 \phi_p (1-\phi_p) \rho \lambda_p} \qquad [3.2\text{-}1]$$

where γ_m is the shear strain acting on the grain, r_p is the matrix carbide radius value, β is a material constant, ρ is the mobile dislocation density within the grain, λ_p is the matrix carbide spacing, b is the Burgers vector, and ϕ_p is the matrix carbide volume fraction. Following absorption into the boundary, dislocation glide results in the accumulation of back stress at the carbide interface. The backstress is proportional to the number of dislocations in the pile-up, n_p, and is expressed in a modified form of Eq. [2.4-15] as:

$$\dot{n}_p = n_{gb} \frac{M_d b \mu}{\lambda_{gb}} \tau_{net} - n_p \frac{D_{gb}}{r_{gb}^{\ 2}} \left[\exp\left(\frac{\sigma_n b^3}{kT} \right) - 1 \right] \qquad [3.2\text{-}2]$$

where μ is a material constant ($0 < \mu < 1$), n_{gb} is the number of mobile grain boundary dislocations, M_d is the dislocation mobility, λ_{gb} is the characteristic grain boundary length, b is the Burgers vector, τ_{net} is the net or effective shear stress ($\tau_{applied} - \tau_{back}$), r_{gb} is the grain boundary carbide radius, D_{gb} is the

diffusivity of the grain boundary, σ_n is the applied stress normal to the grain boundary, k is Boltzmann's constant, and T is temperature in Kelvin. In Eq. [3.2-2], the first term on the right hand side represents the rate at which mobile grain boundary dislocations arrive at the pile-up, while the second term describes the rate at which dislocations climb and escape the pile-up. With the increasing backstress, the rate of incoming dislocations to the pile-up, along with the sliding rate, decreases in accordance with Eq. [3.2-3] and Eq. [3.2-4]:

$$\tau_{back} = \frac{n_p E_{gb} b}{2\pi(1-\upsilon)\lambda_{gb}} \ln\left(\frac{\lambda_{gb}}{b}\right) \qquad [3.2\text{-}3]$$

$$\dot{u}_s = \frac{\eta}{b}\tau_{net} \qquad [3.2\text{-}4]$$

where ν is Poisson's ratio, E_{gb} is the grain boundary modulus, η is the grain boundary viscosity, and $\dot{u}_s$ is the grain boundary sliding rate. Under the assumption that the number of mobile extrinsic grain boundary dislocations, n_{gb}, is equal to the number that have been released from the matrix, n_m, Eq. [3.2-2] can be rewritten as:

$$\dot{n}_p = n_m \frac{M_d b\mu}{\lambda_{gb}}\tau_{net} - n_p \frac{D_{gb}}{r_{gb}^{\,2}}\left[\exp\left(\frac{\sigma_n b^3}{kT}\right) - 1\right] \qquad [3.2\text{-}5]$$

such that the contribution of matrix dislocations to the grain boundary sliding rate is defined.

In the following work, a series of aging and stress relaxation tests have been conducted as a means of parameter determination for the model described in the previous work[35]. Aging at 1000°C for various exposure times were used to produce unique values of carbide size, spacing, and volume fraction. Following aging, stress relaxation testing at 780°C was conducted under compressive load, with an initial stress of 200 MPa. Microstructural analysis of carbides (aging), through SEM imaging, and associated mechanical response (stress relaxation) provide the necessary parameters for analyzing the rate controlling properties carbides on the grain boundary sliding rate as described above.

3.3 Description of Experimental Work

3.3.1 Material

The material of interest in the current study is Inconel 617, a solution-strengthened nickel-based superalloy and a candidate material for the next generation of nuclear reactors. At temperatures in the range of 649-1093°C, the major strengthening phases have been determined to be the $M_{23}C_6$ type carbide which have been shown to precipitate early in the aging process[1] residing preferentially along grain boundaries, followed by intragranular regions[2], [17], [37], [38]. Standard composition can be seen in Table 3.3-1. Material used in this study was hot rolled and obtained in the solution treated condition.

Table 3.3-1 – Composition of Inconel 617 (wt.%)[2]

Ni	Cr	Co	Mo	Al	C	Fe	Mn	Si	S	Ti	Cu	B
44.5 min	20 - 24	10 - 15	8 - 10	0.8 - 1.5	0.05 - 0.15	3 (max)	1 (max)	1 (max)	0.015 (max)	0.6 (max)	0.5 (max)	0.006 (max)

All specimens were subjected to a two-hour solution heat treatment at 1200°C followed by a water quench to dissolve any remaining secondary phases. Intragranular MC carbides can still be observed after solutioning and are oriented in bands along the rolling direction, as shown in Figure 3.3-1 and Figure 3.3-2.

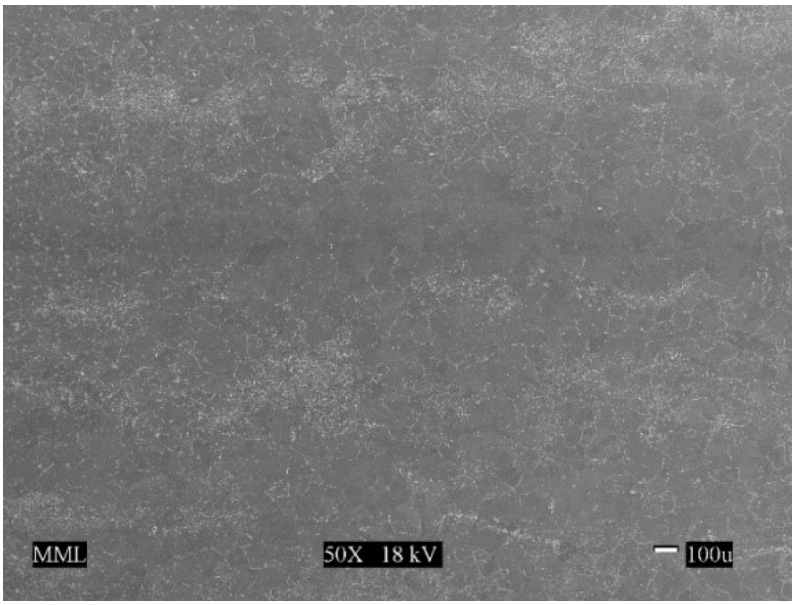

Figure 3.3-1: Microstructure (50X magnification) after solutioning at 1200 °C for 2 hours followed by a water quench. Intragranular carbides can still be observed in bands that run along the rolling direction (horizontally with respect to the micrograph). All samples were subjected to the solution treatment to ensure the same initial microstructure prior to any further aging treatments and testing.

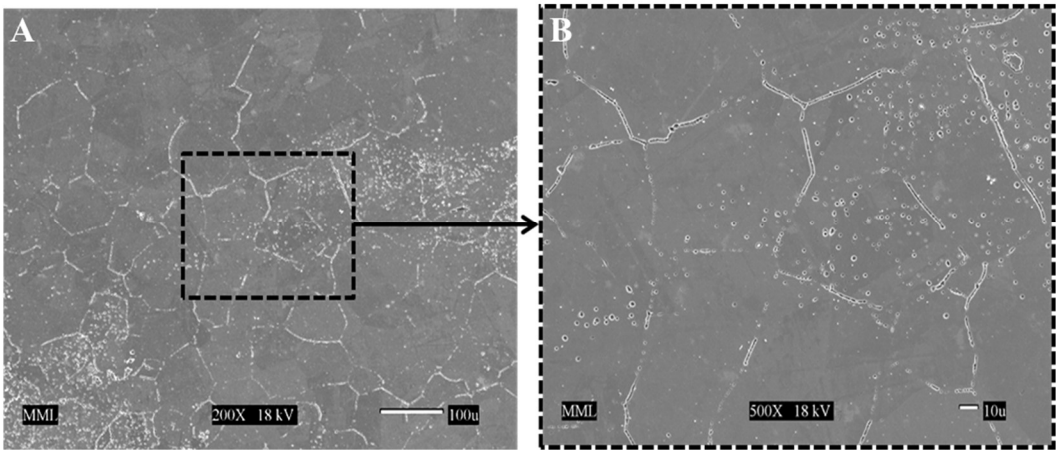

Figure 3.3-2: Microstructure at A) 200X and B) 500X after solutioning at 1200°C for 2 hours followed by a water quench. Intragranular carbides of the MC type can be observed in bands which run transverse to the images above while grain boundaries appear mostly clean.

Grain boundaries appear to be devoid of carbides, as shown in Figure 3.3-2. Grains are equiaxed after solutioning with an average grain size of 68 μm as determined through the linear incept method with directional test lines overlaid vertically and horizontally with respect to the image.

3.3.2 Specimen Aging

The heat treatments for the four specimens are detailed in Table 3.3-2. As the in-service temperature range of interest is 950 °C – 1000 °C, an aging temperature of 1000 °C was chosen in order to best replicate the microstructural evolution which would be expected for IN617 during its service life.

Table 3.3-2 – IN617 Stress Relaxation Specimen Heat Treatments

Specimen ID	Solution Temperature	Solution Duration	Cooling Type	Aging Temperature	Aging Time	Cooling Type
SR-1	1200 °C	2 hrs	Quench (water)	1000 °C	0 hrs	Quench (water)
SR-2	1200 °C	2 hrs	Quench (water)	1000 °C	3 hrs	Quench (water)
OB-1	1200 °C	2 hrs	Quench (water)	1000 °C	7 hrs	Quench (water)
SR-3	1200 °C	2 hrs	Quench (water)	1000 °C	30 hrs	Quench (water)

Solution and aging treatments of the as-received IN617 specimens were conducted in furnace with a digital temperature readout from a thermocouple placed within the furnace tube. Ice water bath quenching was performed immediately after both the solution and aging treatments. Surface preparation was conducted using a progression of coarse metallurgical grinding paper (600 grit) to diamond polishing slurry (0.5 micron). Electro-chemical etching was performed using Carpenter's Reagent Etchant (8.5 grams $FeCl_3$ / 2.4 grams $CuCl_2$/122 ml alcohol/122 ml HCl/6 ml HNO_3) and a 12V power supply with a 0.225 – 0.250 Amp current output. After etching, the specimens were analyzed using a Jeol JSM-840 SEM with a tungsten filament supplied with a 15-18kV accelerating voltage. In addition to those listed in Table 3.3-2, an additional specimen (OB-1) was solutioned in an identical fashion to the stress relaxation specimens and aged for at 1000 °C for seven hours. This was done as a point of comparison in order to verify carbide measurements made for the SR-1, SR-2, and SR-3 test specimens; these additional observations are presented in Table 3.3-2.

3.3.3 Stress Relaxation

Stress relaxation tests were carried out following ASTM E328 as a guideline for specimen dimensioning and experimental procedure. The stress relaxation specimen dimensions and test parameters are listed in Table 3.3-3.

Table 3.3-3 – IN617 Stress Relaxation Specimen Test and Program Parameters

Specimen	LxWxH (mm)	Target Stress (MPa)	Test Temperature (°C)	Ramp Time (s)	Test Force (N)
SR-1	9.44 x 9.19 x 6.32	200	780	12.384	17,338.302
SR-2	8.50 x 8.92 x 6.31			10.835	15,169.947
SR-3	8.88 x 9.27 x 6.31			11.759	16,463.520

Testing was conducted on a servo-hydraulic mechanical testing system (MTS) equipped with a high temperature furnace. The test temperature was recorded for the entire test duration through the use of two thermocouples welded to adjacent sides of each test specimen. Each thermocouple was connected to a TestStar II control system which monitored and maintained the desired temperature. The stress relaxation procedure is illustrated in Figure 3.3-3.

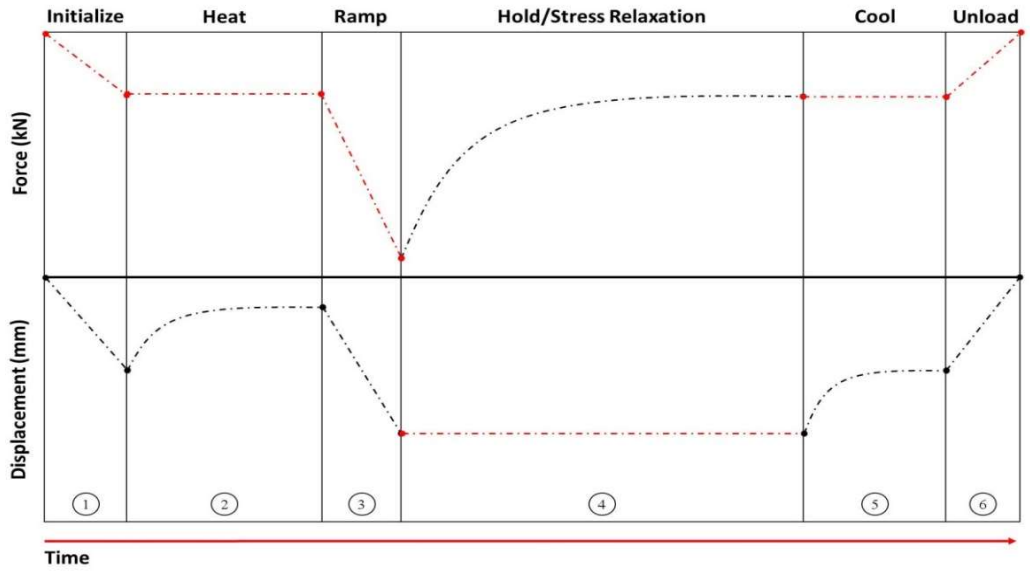

Figure 3.3-3: Illustration of the stress relaxation routine used, where red lines indicate the control mode (force or displacement) of the MTS test machine. The Initialization segment (1) involved compressing the specimen to a stress of approximately 1 MPa. During the Heat segment (2), the stress applied to each test specimen was maintained while the furnace was brought up to temperature and thermal expansion occurred. The Ramp segment (3) involved load ramping to approximately 17 kN to achieve the desired initial compressive stress of 200 MPa. The Hold/Stress Relaxation segment (4) was executed in displacement control in which each specimen was permitted to relax. When sufficient time had passed such that an identifiable saturation in stress was observed, the furnace was turned off and the specimen and test equipment were allowed to cool (5) while maintaining a constant applied stress. Once cooled to room temperature, the specimen was unloaded (6) and removed from the testing machine.

The stress relaxation test was initialized by applying a small compressive load (~1 MPa) to hold the test specimen in place between the grips. During heating to 780°C at 1 MPa, the specimen displacement was monitored in order to ensure the thermal expansion of it and the test equipment had stabilized prior to loading. A test temperature of 780 °C was chosen, as to fall above the γ' solvus temperature of approximately 760 °C[17] to prevent unintentional γ' precipitation, as well as to

suppress $M_{23}C_6$ carbide evolution[38]. Once the test temperature was achieved and a negligible fluctuation in displacement due to thermal expansion was observed, an initial stress of 200 MPa was applied at a rate of 1.4 kN/s (strain rate of $\sim 1*10^{-4}$ s^{-1}). Based on the strain-rate sensitivity of IN617 presented by Rahman *et al*.[39], the target strain rate was chosen such that test specimens remained with the elastic regime during the load ramp process, as the proportional limit has been shown to vary with strain rate. Upon achieving the initial stress, the control mode was shifted from force to displacement control, maintaining constant displacement through the stress relaxation test period.

3.4 Experimental Results and Analysis

3.4.1 Aging

Microstructure post aging for 3, 7, and 30 hours can be seen in Figure 3.4-1 - Figure 3.4-3 at 100x, 3500x, and 7500x magnification, respectively. Image analysis of the 3, 7, and 30 hour aged specimens revealed a trend of increasing carbide radius, volume fraction, and grain size up to 30 hours of exposure time as shown in Figure 3.4-4 and in Table 3.4-1. Grain size was determined from the linear intercept method and was also observed to increase with increasing exposure time.

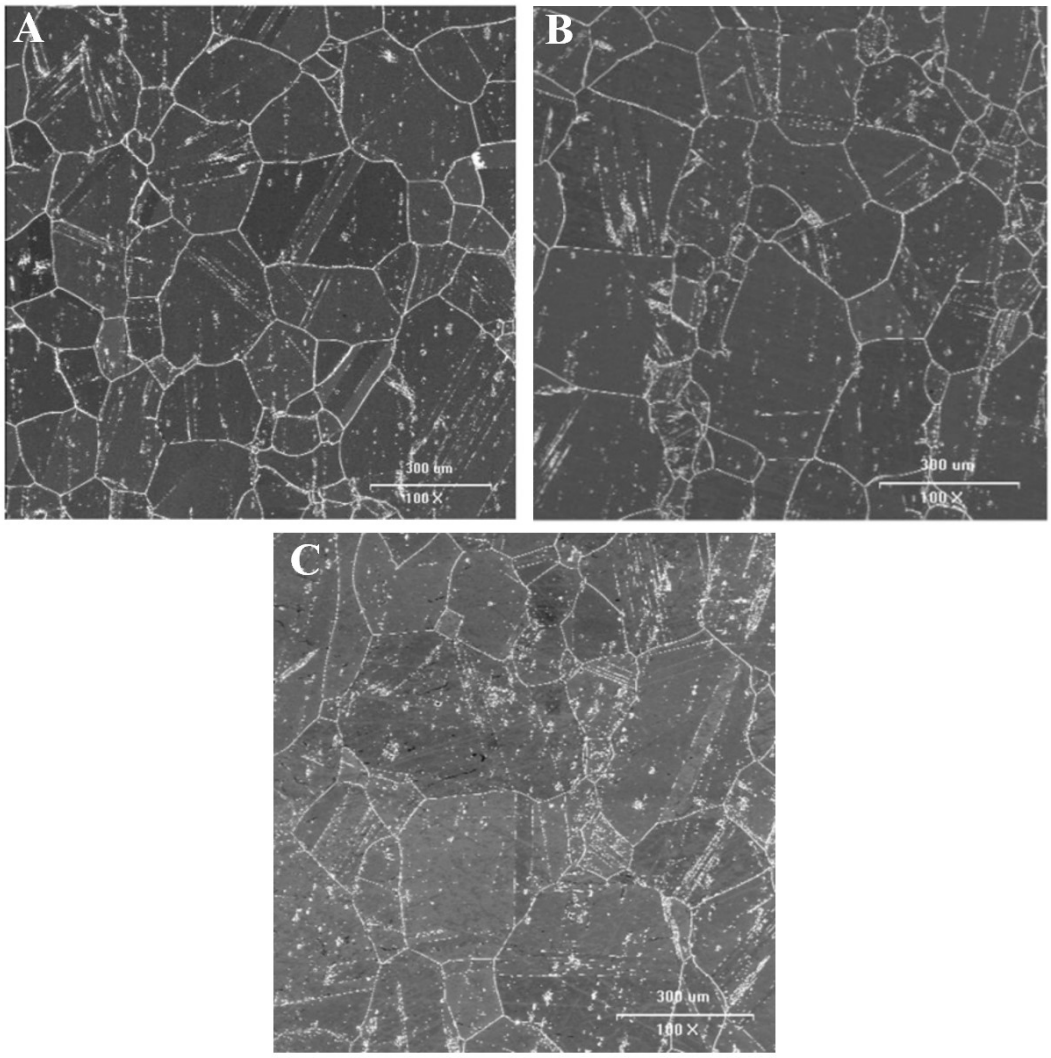

Figure 3.4-1: Microstructure at 100x of IN617 specimens aged at 1000 °C for A) 3 hours B) 7 hours and C) 30 hours showing relative grain size. Grain size was determined through linear intercept method via image analysis software (SigmaScan® - Systat Software Inc.).

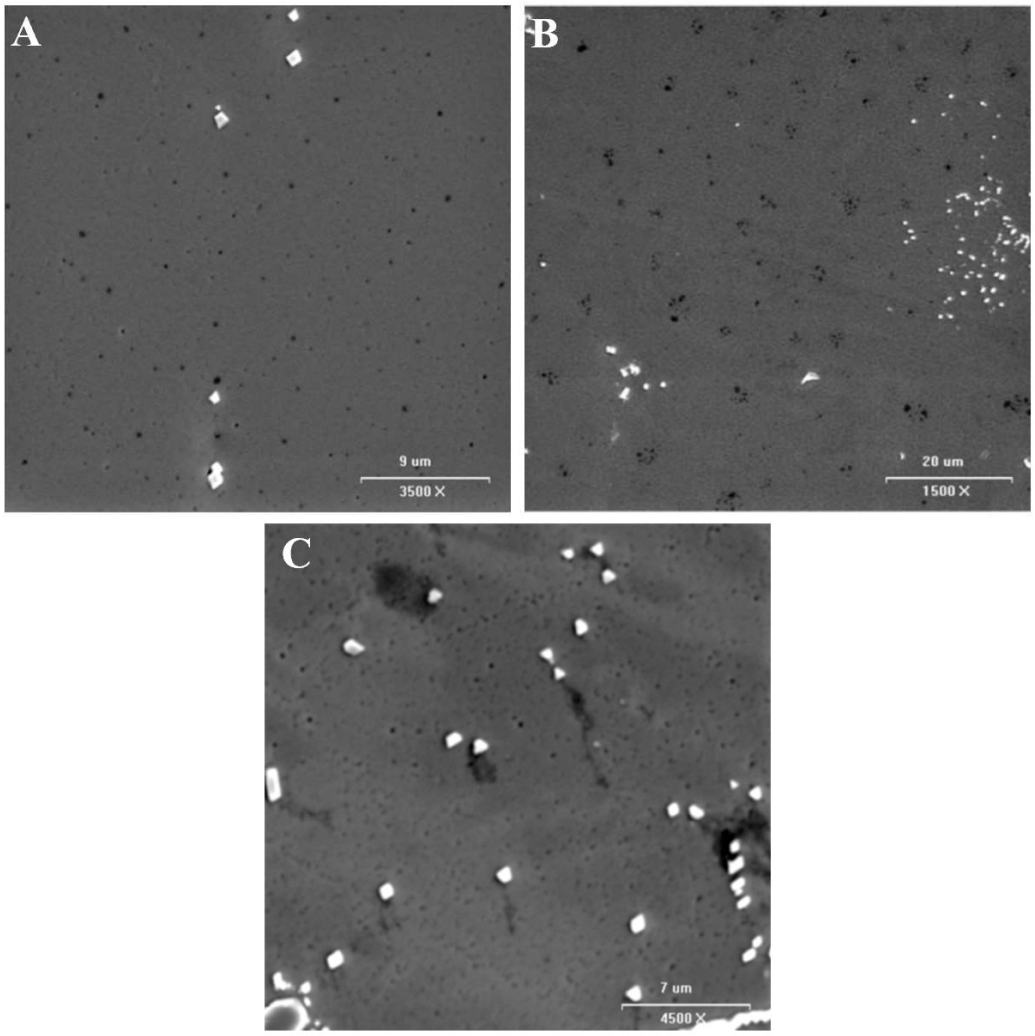

Figure 3.4-2: Microstructure at 3500x of IN617 specimens aged at 1000 °C for A) 3 hours B) 7 hours and C) 30 hours showing $M_{23}C_6$ carbide precipitation. Intragranular carbide size and volume fraction were determined via image analysis software (SigmaScan® - Systat Software Inc.).

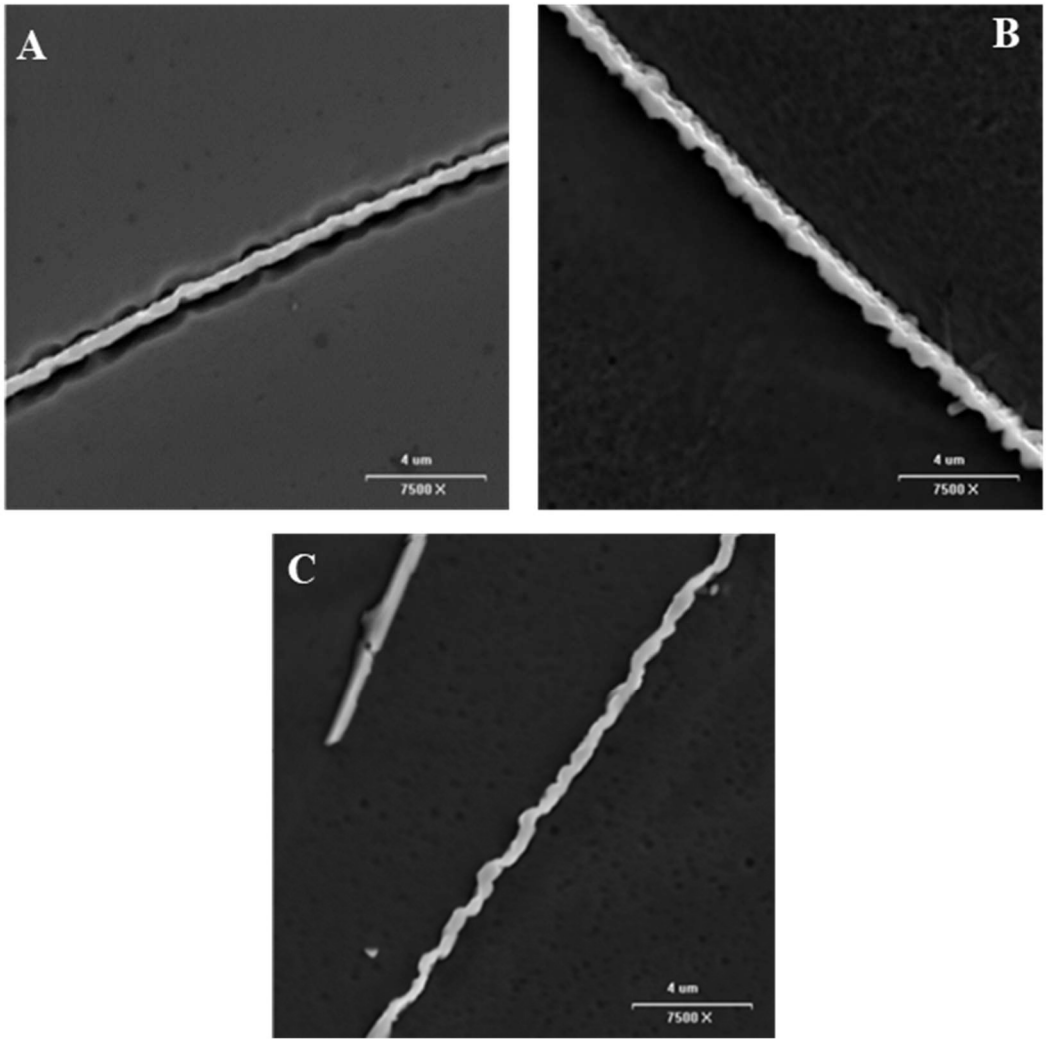

Figure 3.4-3: Microstructure at 7500x of IN617 specimens aged at 1000 °C for A) 3 hours B) 7 hours and C) 30 hours showing grain boundary carbides. Grain boundary carbide spacing and size were determined through use of image analysis software (SigmaScan® - Systat Software Inc.)

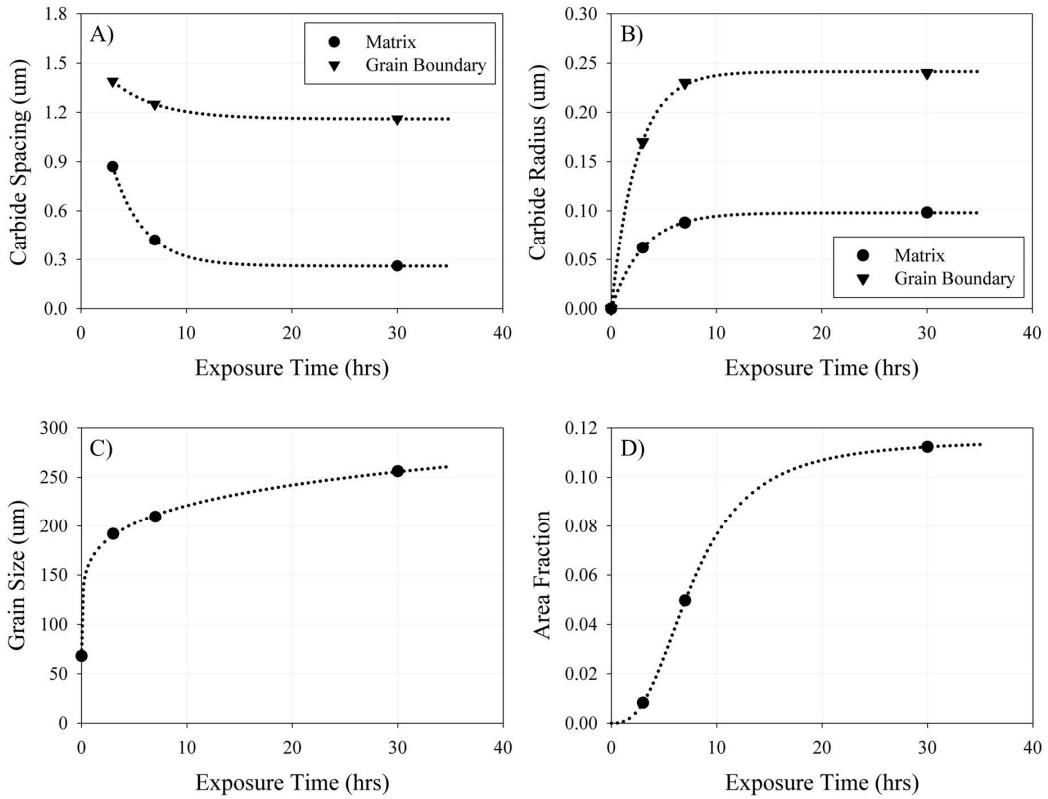

Figure 3.4-4: Microstructural measurements of A) $M_{23}C_6$ matrix and grain boundary carbide spacing B) $M_{23}C_6$ matrix and grain boundary carbide radius C) grain size and D) $M_{23}C_6$ matrix area/volume fraction (ϕ_p) prior to testing

Table 3.4-1 – Quantitative Microscopy of Heat Treated Specimens

Specimen	**SR-1**	**SR-2**	**OB-1**	**SR-3**
Exposure Time (hrs)	0	3	7	30
Matrix Carbide Volume Fraction, ϕ_p	*	0.83%	4.97%	11.23%
Median Carbide Radius, r_p (m)	*	$6.2 \cdot 10^{-8}$	$8.8 \cdot 10^{-8}$	$9.8 \cdot 10^{-8}$
ASTM Grain Size, d_{grain} (m)	$68 \cdot 10^{-6}$	$191.5 \cdot 10^{-6}$	$209.5 \cdot 10^{-6}$	$256.1 \cdot 10^{-6}$
Matrix Carbide Spacing, λ_p (m)	*	$8.7 \cdot 10^{-7}$	$4.2 \cdot 10^{-7}$	$2.6 \cdot 10^{-7}$
Mean Grain Boundary Carbide Radius, r_{gb} (m)	*	$0.17 \cdot 10^{-6}$	$0.23 \cdot 10^{-6}$	$0.24 \cdot 10^{-6}$
Mean Grain Boundary Carbide Spacing, λ_{gb} (m)	*	$1.39 \cdot 10^{-6}$	$1.25 \cdot 10^{-6}$	$1.16 \cdot 10^{-6}$

* - Microscopy revealed $M_{23}C_6$ carbides of negligible volume fraction and size

3.4.2 High Temperature Stress Relaxation

In order to verify that the loading remained in the elastic regime of the material, the linearity of the load-displacement curves for the SR-1, SR-2, and SR-3 was verified, as shown in Figure 3.4-5 and detailed in Table 3.4-2.

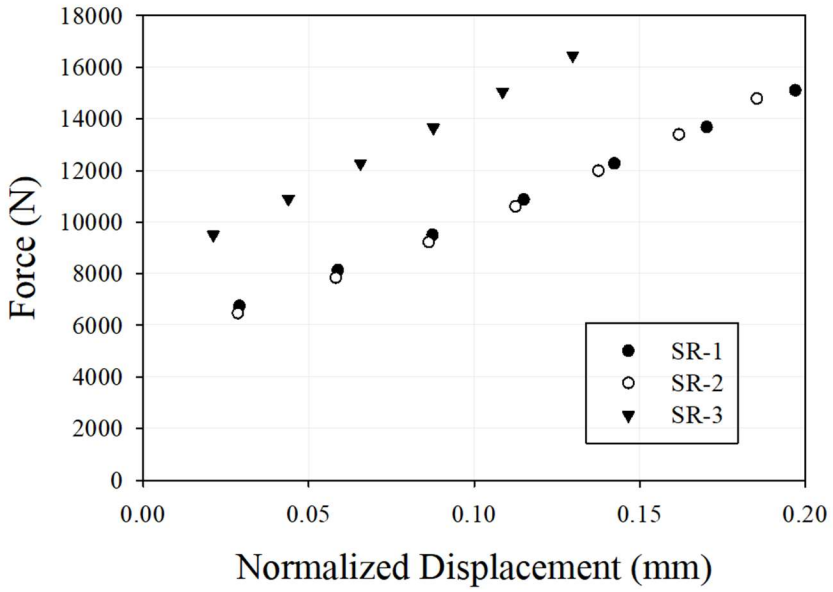

Figure 3.4-5: Load-displacement curves during Ramp segment (see Figure 3.3-3) to attain initial compressive stress of 200 MPa for stress relaxation tests for the 0 hour (SR-1), 3 hour (SR-2), and 30 hour (SR-3) aged IN617 specimens (initial portion of load ramp segment removed for clarity). A target ramp rate of -1.4 kN/s from 1 to 200 MPa was enforced, resulting in a purely elastic material response.

Table 3.4-2 – IN617 Stress Relaxation Specimen Test and Program Parameters

Specimen	LxWxH (mm)	Target Stress (MPa)	Test Temperature (°C)	Ramp Time (s)	Applied Test Force (N)
SR-1	9.44 x 9.19 x 6.32	200	780	12.384	17,338.302
SR-2	8.50 x 8.92 x 6.31			10.835	15,169.947
SR-3	8.88 x 9.27 x 6.31			11.759	16,463.520

Stress relaxation testing results can be seen in Figure 3.4-6(A) for the three aging conditions (0, 3, and 30 hours), from which the role of aging on the relaxation response can be readily observed. The magnitude and rate of relaxation is significantly reduced with thermal exposure prior, however, little variation in the relaxation response is observed for aging between 3 and 30 hours. The total strain of a material undergoing stress relaxation can be decomposed into its constituent parts as follows:

$$\varepsilon_{total} = \varepsilon_{el} + \varepsilon_{in} + \varepsilon_{pl} \quad [3.4\text{-}1]$$

where ε_{el}, ε_{in}, and ε_{pl} are the elastic, inelastic, and plastic strain components. As the stress relaxation experiments conducted in this work are carried out at 200 MPa, below the yield strength of the material at 1053K, plastic strain is not achieved ($\varepsilon_{pl} = 0$). Inelastic strain, with respect to stress relaxation, is the conversion of elastic strain to plastic strain due to the viscoelastic nature of the material. As the total strain remains constant throughout the stress relaxation test, substituting in $\varepsilon_{el} = \sigma/E$ for the elastic component of strain, and differentiating both sides with respect to time yields:

$$\dot{\varepsilon}_{in} = -\frac{1}{E}\dot{\sigma} \quad [3.4\text{-}2]$$

where $\dot{\sigma}$ is the relaxation rate. The inelastic strain rate as a function of stress is presented in Figure 3.4-6(B).

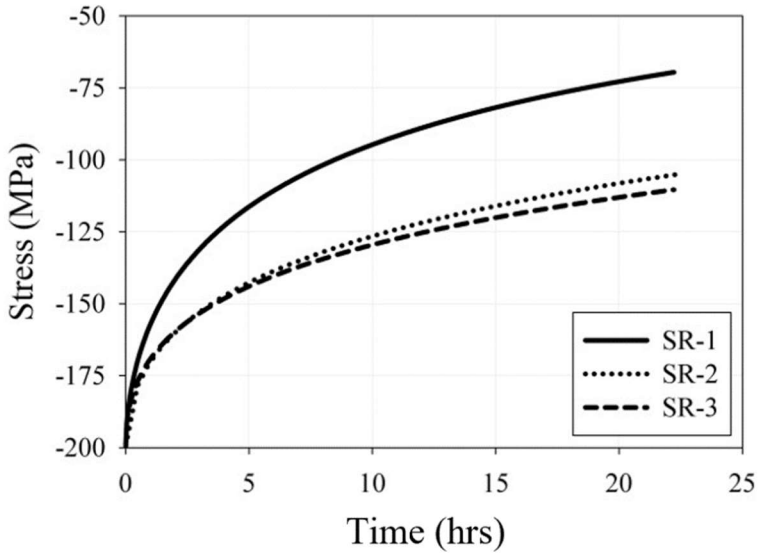

Figure 3.4-6(A): Stress vs. time for initial compressive stress of 200 MPa, showing a decrease in stress relaxation with increasing aging time.

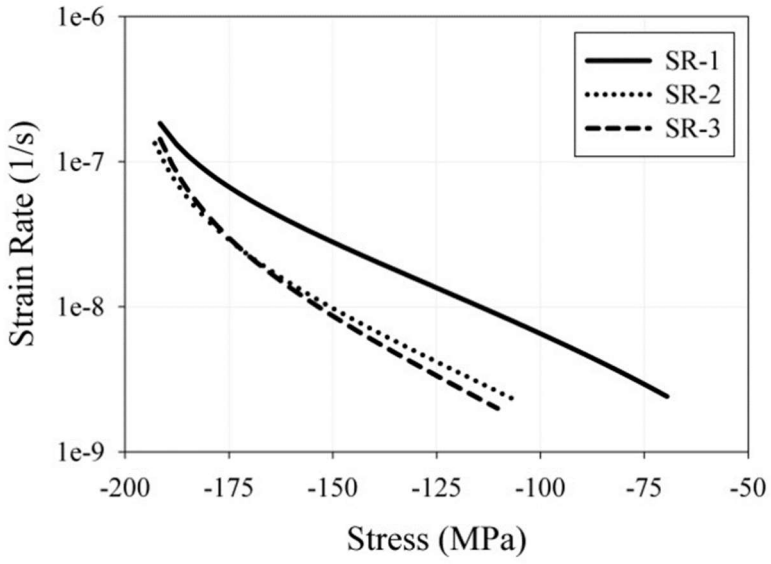

Figure 3.4-6(B): Strain rate vs. stress, showing a decrease in magnitude for increasing aging time for a given stress.

In the 0.6-0.7T_m temperature regime at moderate to high stresses, the presence of the $M_{23}C_6$ matrix carbides results in dislocation climb being the rate-controlling mechanism. Liu and Jonas[24] demonstrated the significance of matrix titanium carbonitrides in alloyed steel through stress relaxation testing at various initial stresses in the temperature range of 850 – 1050 °C. El-Magd *et al.*[21], Balantic *et al.*[18], and Mukherjee[31] showed either experimentally or through analysis of previously published work how the presence of matrix precipitates interrupts dislocation glide, slowing down the rate of deformation by forcing dislocations to climb. Mukherjee[31] identified dislocation climb as being the primary deformation mechanism when the stress exponent n is approximately equal to a value of 4 or 5. Furillo *et al.*[14], through conventional creep testing of specimens with and without grain boundary carbides, concluded that grain boundary carbides were able to suppress or completely prevent grain boundary sliding. A change in apparent stress exponent from ~2 to ~15, with the inclusion of grain boundary carbides, represented a shift from grain boundary to matrix driven creep. Determination of the stress exponent from the stress relaxation data presented in Figure 3.4-6 was calculated through the Zener-Holloman relationship:

$$Z = \dot{\varepsilon} \exp\left(\frac{Q}{RT}\right) = B\left(\frac{\sigma(t)}{E}\right)^n \qquad [3.4\text{-}3]$$

where Z is the Zener-Holloman parameter, $\dot{\varepsilon}$ is the strain rate, B, is a material specific parameter, E is the temperature dependent elastic modulus, Q is the

activation energy for creep, n is the stress exponent, T *is* temperature in Kelvin, and R is the universal gas constant. Rearranging Eq. [3.4-3] and solving for n yields:

$$n = \frac{d \ln(Z/B)}{d \ln(\sigma/E)} \qquad [3.4\text{-}4]$$

from which the stress exponent can be plotted as a function of time and stress, as shown in Figure 3.4-7(A) and Figure 3.4-7(B), respectively.

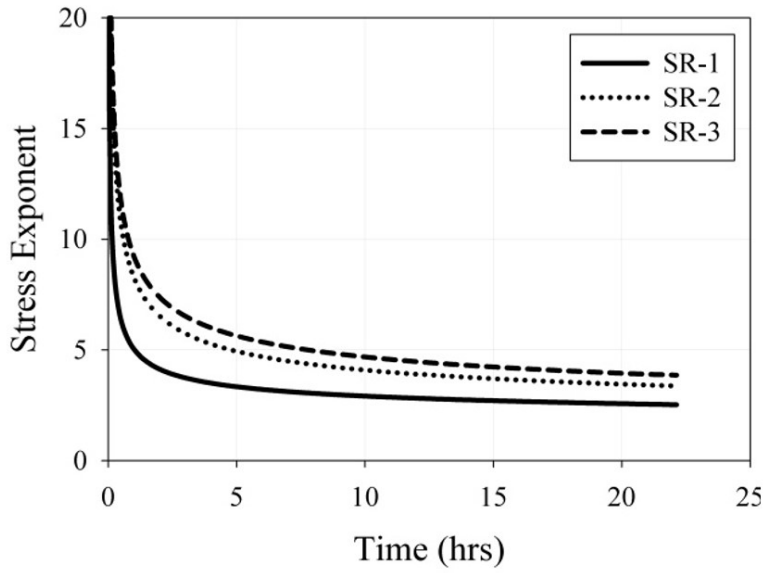

Figure 3.4-7(A): Stress exponent vs. time, showing an increase in stress exponent associated with corresponding increase in aging time.

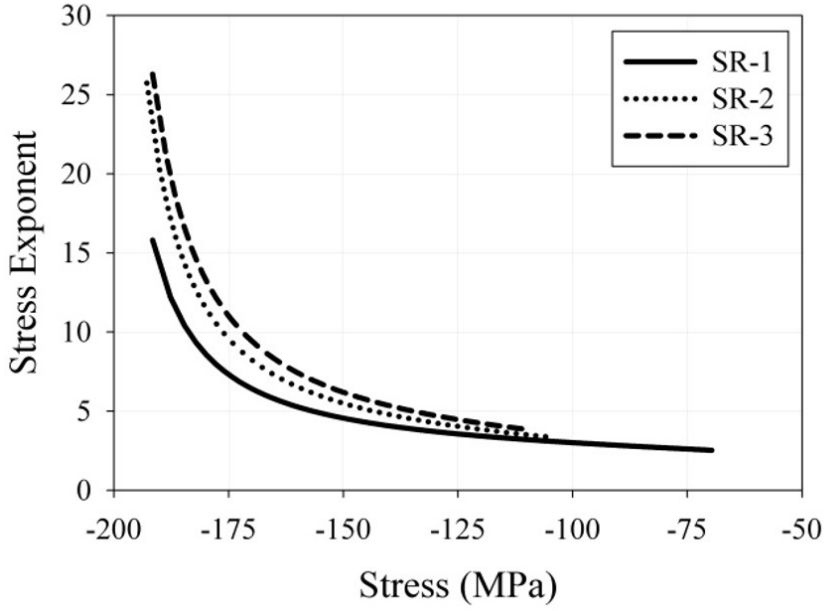

Figure 3.4-7(B): Stress exponent vs. stress, showing an increase in stress exponent at a given stress for increasing aging times. The stress exponents appear to saturate to a near identical value irrespective of stress magnitude or aging time.

The stress exponent, for all aging conditions, initially exhibited values of $n > 15$ suggesting the initial relaxation behavior was governed by matrix deformation; facilitated by through motion of matrix dislocations[14]. It is expected that the supply of dislocations to the grain boundary occurs rapidly in the initial stages decreasing in rate for values of $n > 3$, which represents a transition from combined matrix/grain boundary deformation to grain boundary dominated deformation. As such, it would be expected that matrix carbides govern the initial relaxation behavior, $n > 3$ while grain boundary carbides govern the later stages, $n < 3$.

As creep is a constant load process, ascertaining the creep behavior from stress relaxation behavior of a material is not a direct process. Determining a material's creep behavior from stress relaxation data (or vice versa) is often implemented when limited data is available, as relaxation modulus and creep compliance are the most direct way to characterize and predict a material's behavior as a function of time, stress, and temperature. This has been demonstrated with success using various numerical and analytical techniques[40]–[43].

3.5 Model Simulation

A analytical technique originally presented by Vorotnikov and Rovinskii[42], and further explained by Jung *et al*.[44], provides a straight forward method for converting stress relaxation data into creep strain data given for an equivalent, constant creep stress value. Vorotnikov and Rovinskii[42] presented a relationship which was used to successfully relate stress relaxation data to previously published creep data. With an initial elastic strain, ε_0, the rate at which the conversion of elastic strain to plastic strain via viscoelastic deformation has been characterized as:

$$\varepsilon = \frac{Kt^{p}\sigma^{*}}{E} \qquad [3.5\text{-}1]$$

where the amount of plastic strain, ε, which accumulates as a function of the effective stress, σ^{*}, Young's Modulus, E, exponential constant, p, and time dependent parameter, K. This parameter provides a general characterization of the

stress relaxation capability of the material. In the context of this work, this time-dependent coefficient equates to a smeared value which captures the grain and grain boundary's viscoelastic nature in a non-descript way. The relationship proposed by Jung *et al.*[44] is of the form:

$$\ln\left(\frac{\sigma}{\sigma_0}\right) = -k^p t^p \qquad [3.5\text{-}2]$$

Once values for *k* and *p* have been determined, Eq. [3.5-2] can be used in conjunction with the stress relaxation data to generate creep strain data given a constant creep stress (σ_{creep}) as:

$$\varepsilon_{creep} = \left(\frac{k^p t^p \sigma_{creep}}{E}\right) \qquad [3.5\text{-}3]$$

where $\sigma_{creep} = \sigma_o$. From Eq. [3.5-3], equivalent creep strain and strain rate have been calculated and presented in Figure 3.5-1(A) and Figure 3.5-1(B), respectively.

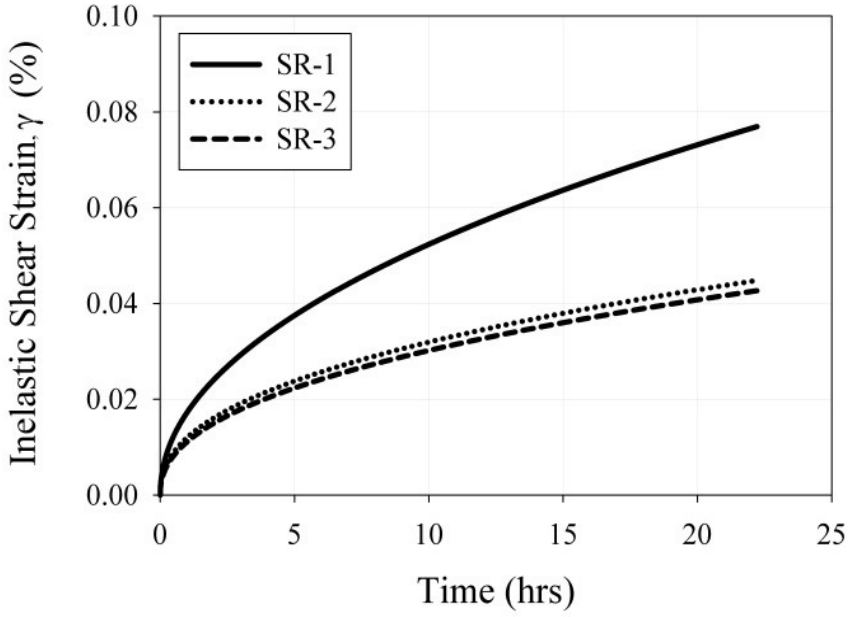

Figure 3.5-1(A): Equivalent creep strains for SR-1, SR-2, and SR-3 stress relaxation specimens generated through interconversion of stress relaxation data.

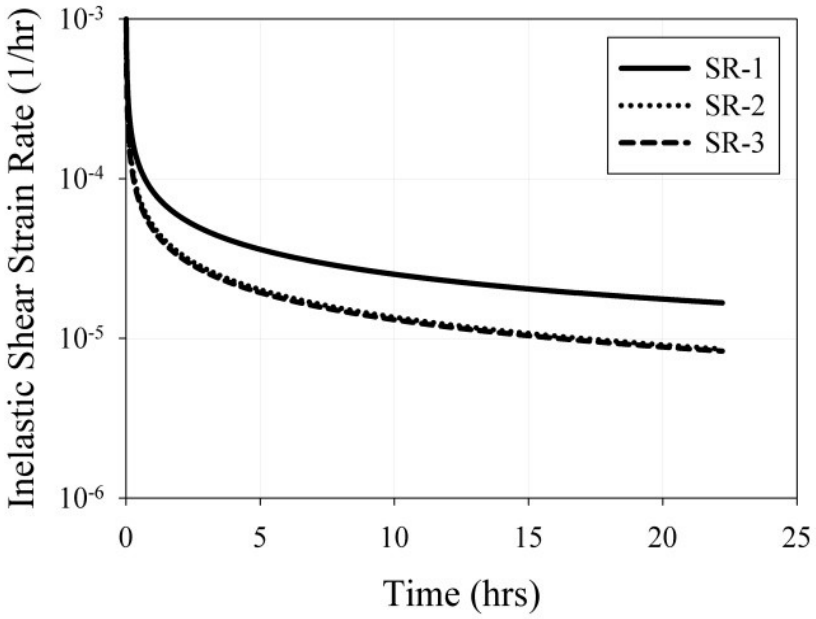

Figure 3.5-1(B): Equivalent creep strain rate for SR-1, SR-2, and SR-3 stress relaxation specimens generated through interconversion of stress relaxation data.

To apply the traction-displacement relationships to the converted creep strain data several initial conditions must first be established. The assumed initial conditions are that the number of dislocations in the pileup within the grain boundary is zero ($n_{p_{t0}} = 0$), the number of lattice dislocations made available by the matrix is zero ($n_{m_{t_0}} = 0$), there has been no previous loading of the specimen ($u_{inelastic_{t0}} = 0$), and that the compressive stress upon initial loading of the specimen is below the elastic limit of the material and subsequently no dislocation motion ensues ($u_{total_{t_0}} = u_{elastic_{t_0}}$, $v_{g,gb_{t_0}} = 0$, $v_{c,gb_{t_0}} = 0$). With the known applied stress used in the stress relaxation tests, σ_{t_0} (calculated from IN617 compression specimen dimensions and pre-determined load as verified by the ramp data generated by the load cell used in the experimental setup), the remaining initial conditions for applied traction ($T_{app_{t_0}}$) and initial elastic strain ($\varepsilon_{el_{t_0}}$) can be determined through Eq. [3.5-4] and Eq. [3.5-5]:

$$T_{net_{t_0}} = T_{app_{t_0}} - T_{back_{t_0}} = T_{t_0} \qquad [3.5\text{-}4]$$

$$\varepsilon_{el_{t_0}} = \frac{\sigma_{t_0}}{E_{eqv}} \qquad [3.5\text{-}5]$$

where E_{eqv} is an equivalent elastic modulus which approximates the stiffness of the matrix and grain boundary and $\varepsilon_{el_{t_0}}$ is the resulting initial elastic strain. The total displacement, $u_{TOT_{t_0}}$ at the matrix - grain boundary interface at $t = t_0$ (initial elastic displacement prior to relaxation) is approximated by the product of the grain

diameter, d_{grain}, Poisson's ratio of the material (ν), and initial elastic strain calculated in:

$$u_{TOT_{t_0}} = u_{elastic_{t0}} \approx \left(\varepsilon_{el_{t_0}} \nu\right) d_{grain} \quad [3.5\text{-}6]$$

Over the first-time interval where stress relaxation is observed, $[t_0, t_1]$, the first relaxed stress value recorded, σ_{t_1}, is used to determine the rate of inelastic strain development facilitated by grain boundary sliding:

$$\left.\frac{du_s}{dt}\right|_{t_0}^{t_1} = \frac{1}{ME_{eqv}}(\sigma_{t_1} - \sigma_{t_0})\lambda_{GB} \quad [3.5\text{-}7]$$

$$u_{inelastic_{t1}} = \left.\frac{du_s}{dt}\right|_{t_0}^{t_1} + u_{inelastic_{t_0}} \quad [3.5\text{-}8]$$

where M is the Taylor Factor. The rate of grain boundary sliding, $\dot{u}_s$, is determined by Eq. [3.5-7] over the interval $[t_0, t_1]$. The net traction force required over the specified time interval is then calculated as:

$$T_{net_{t_1}} = \left(\left.\frac{du_s}{dt}\right|_{t_0}^{t_1}\right)\frac{\eta}{b} = \left(\left.\frac{d\gamma}{dt}\right|_{t_0}^{t_1}\right)\frac{\lambda_{GB}\eta}{b} \quad [3.5\text{-}9]$$

The rate of change in net traction is driven by the length of the dislocation pileup within the grain boundary, the grain boundary viscosity, and the recovery facilitated by dislocation climb. With a grain boundary viscosity initially treated as a constant value, the reduction in the net traction term determined through Eq. [3.5-4] over the

given time interval is attributed to the back stress created by the dislocation pileup, and therefore can be used to calculate the requisite number of dislocations which must exist in the pileup (ignoring the logarithmic variation of n_p):

$$\left.\frac{dn_p}{dt}\right|_{t_0}^{t_1} = \left.\frac{dT_{back_{t_1}}}{dt}\right|_{t_0}^{t_1} \left[\frac{2\pi\lambda_{GB}(1-\upsilon)}{Gb\ln\left(\frac{\lambda_{GB}}{b}\right)}\right] \qquad [3.5\text{-}10]$$

The rate equation presented in Eq. [3.2-2] can be rearranged as shown in Eq. [3.5-11] in order to relate the number of dislocations that are released from the matrix, n_m, to that which is required within the grain boundary characteristic length, n_{gb}, to facilitate the grain boundary sliding process:

$$n_m\Big|_{t_0}^{t_1} = n_{gb}\Big|_{t_0}^{t_1} = \left(\frac{1}{T_{net_{t_1}}}\frac{\lambda_{GB}}{M_d b}\right)\left(\left.\frac{dn_p}{dt}\right|_{t_0}^{t_1} + n_p\Big|_{t_0}\frac{D_{gb}}{r_{GB}^{\,2}}\left[\exp\left(\frac{\sigma_n b^3}{kT}\right)-1\right]\right) \qquad [3.5\text{-}11]$$

This rearrangement, along with Eq. [2.4-33] presented in the previous work[35] links the matrix microstructure and dislocation kinetics to that of the grain boundary. In order to gain an understanding of the behavior of the dislocation kinetics within the matrix and grain boundary, the uncoupled version of the grain boundary sliding model is applied to the test data using Eqs. [3.5-4] - [3.5-10] as described below. The uncoupled matrix model requires the input of the constant microstructural parameters, stress, and temperature (along with required physical and material constants) and is capable of generating a corresponding n_m. The grain boundary sliding model requires the same input and is initially executed in an

inverted fashion which outputs n_{gb}, n_p, and T_{back}, as well as their associated rates and rate of recovery via dislocation climb. This provides insight into the grain boundary dislocation population, n_{gb}, as well as the number of dislocations within the pileup, n_p, the rate of change of the pileup, $\frac{dn_p}{dt}$, the backstress (or back-traction) T_{back}, and recovery rate over a given grain boundary characteristic length.

The high temperature stress relaxation test data for specimens SR-1, SR-2, and SR-3, through the previously described conversion process, are used to produce equivalent creep strain curves, as shown in Figure 3.5-1(A). As grain boundary sliding is asserted to be the expression of the stress relaxation mechanism, the inelastic grain boundary displacement can be determined through application of Eq. [3.5-9] to the stress relaxation data. The calculated inelastic sliding displacement for each stress relaxation data set is shown in Figure 3.5-2.

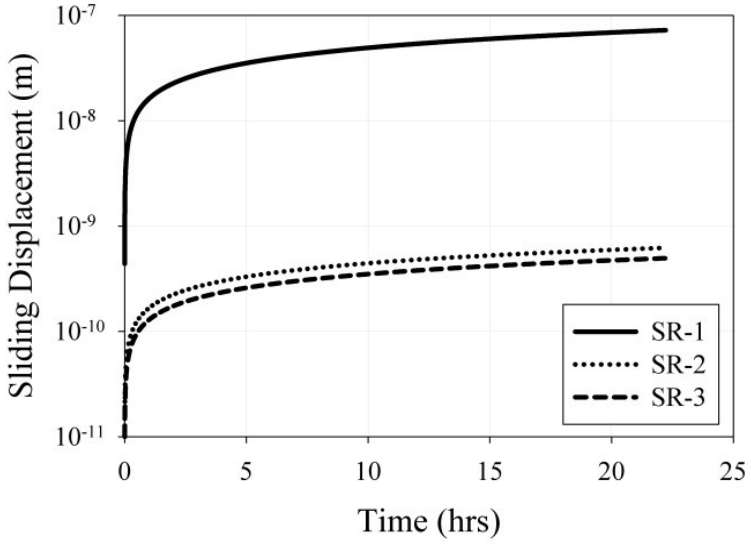

Figure 3.5-2: Inelastic grain boundary sliding calculated through use of physics-based deformation model for solutioned-only (SR-1), 3 hour aged (SR-2), and 30 hour aged (SR-3) IN617 stress relaxation specimens.

The creep strain data is then analyzed using Eq. [3.5-9] to generate a time-dependent value of T_{net}. As the initial applied traction is known, Eq. [3.5-4] can be used to determine the backstress (or back traction), T_{back}, generated over the grain boundary characteristic length for the selected time interval. These time-dependent back traction and net traction behaviors for each of the three test specimens are shown in Figure 3.5-3 and Figure 3.5-4.

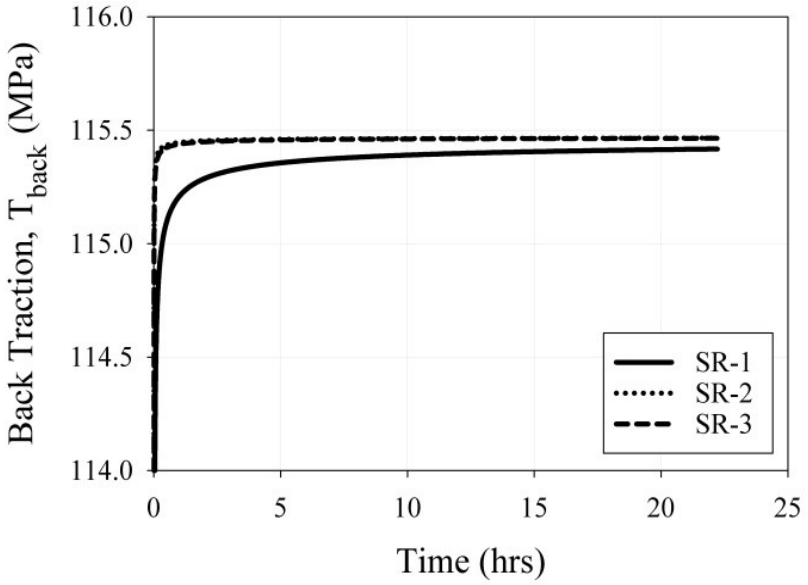

Figure 3.5-3: Simulation results for the backstress (back traction) acting along the grain boundary as functions of time for solutioned-only (SR-1), 3 hour aged (SR-2), and 30 hour aged (SR-3) IN617 stress relaxation specimens.

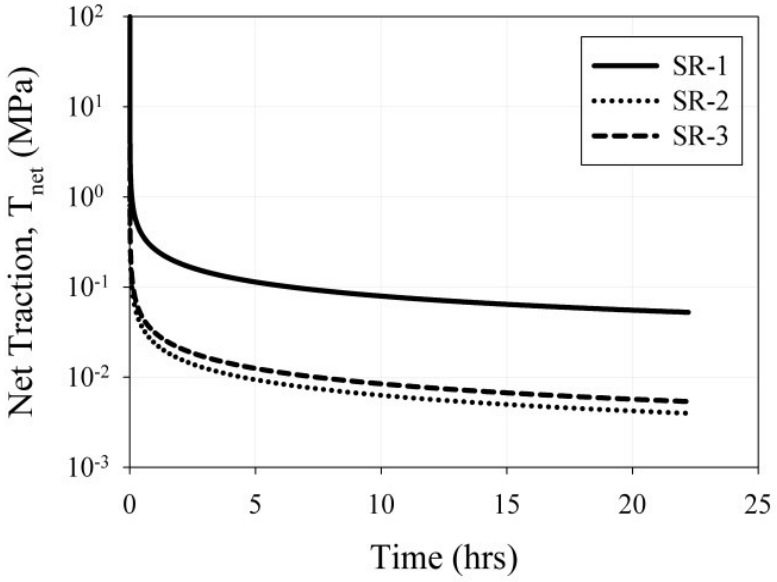

Figure 3.5-4: Simulation results for the net traction acting along the grain boundary as functions of time for solutioned-only (SR-1), 3 hour aged (SR-2), and 30 hour aged (SR-3) IN617 stress relaxation specimens.

As the backstress is generated due to the dislocation pileup formation and continued growth within the characteristic grain boundary length, the rate of change of the back stress is used to determine the rate of change of the number of dislocations within the pileup, $\frac{dn_p}{dt}$, through Eq. [3.5-10]. These profiles are shown in Figure 3.5-5. The solution to the differential equation for $\frac{dn_p}{dt}$ presented in Eq. [3.5-10] can be obtained through numerical integration of the curves in Figure 3.5-5 in order to determine the number of dislocations within the pileup at a given time, which is shown for each test specimen in Figure 3.5-6(A) and Figure 3.5-6(B).

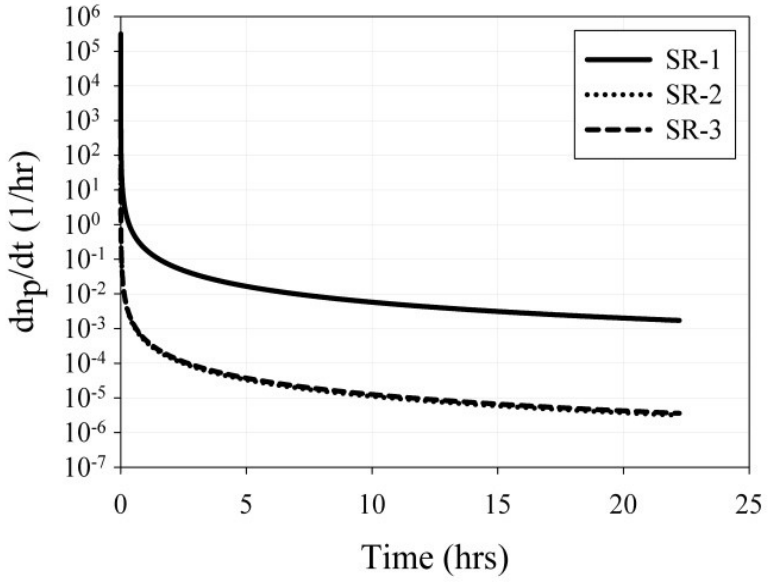

Figure 3.5-5: Simulation results from the physics-based model simulation which show the rate of change of the pileup (dn_p/dt) for solutioned-only (SR-1), 3 hour aged (SR-2), and 30 hour aged (SR-3) IN617 stress relaxation specimens.

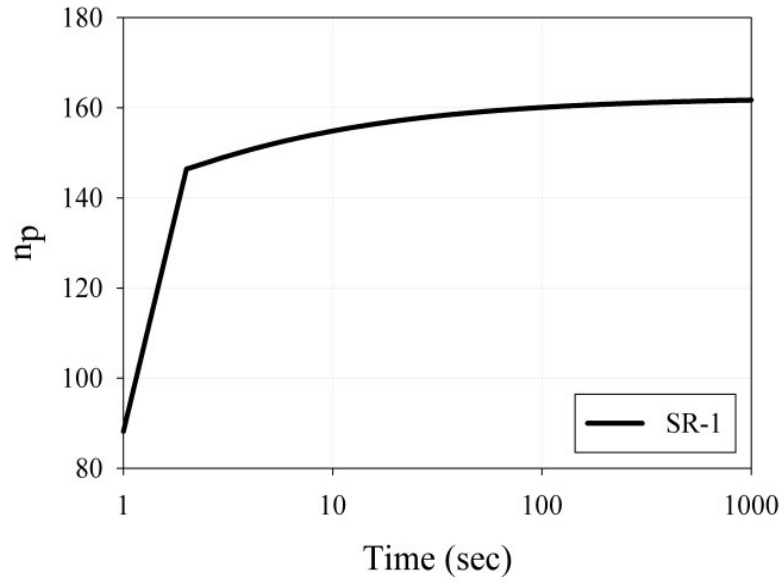

Figure 3.5-6(A): Simulation results from the physics-based model simulation which show the number of dislocations contained within the modeled pileup, n_p, for the solutioned-only (SR-1) IN617 stress relaxation specimens.

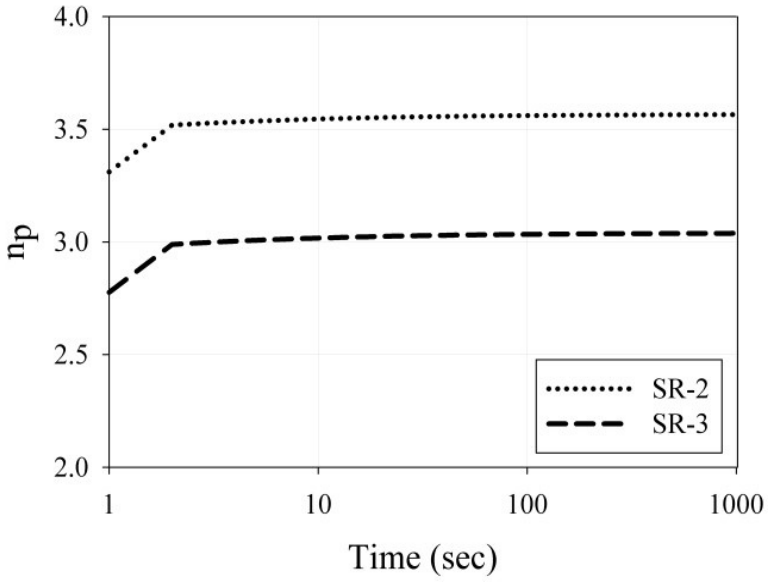

Figure 3.5-6(B): Simulation results from the physics-based model which show the number of dislocations contained within the modeled pileup, n_p, for 3 hour aged (SR-2) and 30 hour aged (SR-3) IN617 stress relaxation specimens (SR-1 removed for clarity)

With an understanding of how T_{net} and n_p (as well as their rates) behave as a function of time, along with knowledge of the constant microstructural parameters of the material system, the grain boundary dislocation population can be assessed. The number of dislocations within the grain boundary, n_{gb}, as a function of time for each specimen is calculate, normalized, and plotted against time in Figure 3.5-7. The normalization constant, ψ, is defined as:

$$\psi = \frac{\xi b}{L_{gb}} \qquad [3.5\text{-}12]$$

where L_{gb} is the grain boundary length, b is the Burgers vector, and ξ is a material constant. Eq. [3.5-12] provides a means of normalizing the calculated values of n_{gb}

with respect to grain size and the theoretical maximum number of grain boundary dislocations which can be accommodated within a grain boundary length ($\approx L_{gb}/b$).

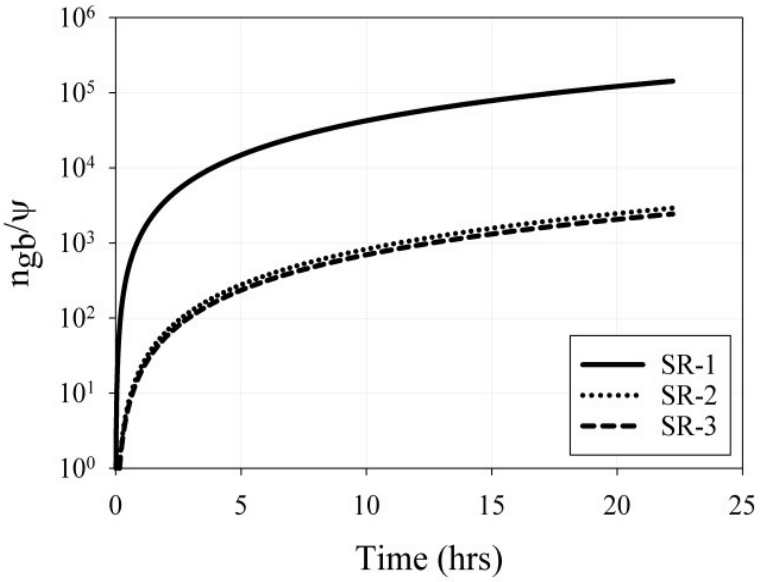

Figure 3.5-7: Simulation results for the normalized number of matrix dislocations absorbed by the grain boundary for solutioned-only (SR-1), 3 hour aged (SR-2), and 30 hour aged (SR-3) IN617 stress relaxation specimens.

The previous work[35] used the matrix deformation model to study several different matrix carbide ripening (growth, coarsening, dissolution) time profiles in order to assess the effects on the number and rate of matrix dislocation release as a function of matrix microstructure. In a similar fashion, the matrix deformation model is used to analyze the matrix dislocation release behavior of test specimens SR-1, SR-2, and SR-3. The difference now being that, unlike the matrix microstructure studies performed in the previous paper[35], the microstructure of the three test specimens is constant over the time domain of

interest, as detailed in Table 3.4-1. The matrix dislocation release as a function of time for each of the stress relaxation test specimens is shown in Figure 3.5-8.

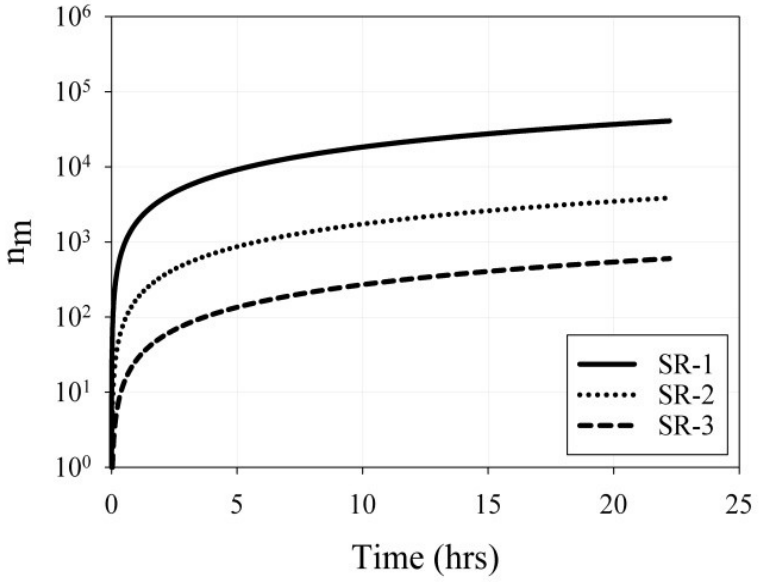

Figure 3.5-8: Simulation results for number of matrix dislocations released for solutioned-only (SR-1), 3 hour aged (SR-2), and 30 hour aged (SR-3) IN617 stress relaxation specimens.

The initial simulation behavior of n_m exhibited instability within the first ten time steps, which is believed to be a result of the assumed initial conditions that were assigned. Beyond this region, the number and rate of dislocation release from the matrix (n_m and $\dot{n}_m$, respectively) can be compared with the number and rate of dislocation absorption within the grain boundary (n_{gb} and $\dot{n}_{gb}$, respectively) that are required to facilitate the grain boundary sliding that acts as the stress relaxation mechanism in IN617 test specimens. In comparing Figure 3.5-7 and Figure 3.5-8, it can be seen that the magnitude of n_m is not always larger than that of n_{gb} which requires further explanation. With respect to the physics-based model used to

generate the results, shown in Figure 3.5-7 and Figure 3.5-8, the grain boundary sliding process demands the value of n_{gb} in order to produce the inelastic strain which ultimately provides the relaxation of stress. The inherent assertion of the model then is that the matrix is, at a minimum, capable of supplying exactly the value of n_{gb}. In considering the values calculated for the mobile dislocation density within the grain for each test specimen as was done in the previous work[35] and the work of Alexandreanu *et al.*[12] which suggests that the grain is capable of producing more dislocations than the grain boundaries are capable of accommodating, it is presumed that such differences in magnitude seen between n_m and n_{gb} in Figure 3.5-7 and Figure 3.5-8 arise as a result of the normalization technique applied through the use of ψ.

An additional stress relaxation experiment was conducted to investigate the proposed grain-grain boundary sliding model. Specimen SR-2 was allowed to continue relaxing for a duration of 235 hours such that the saturation behavior could be observed. After completion of the test, the stress was reduced to 1 MPa at a rate of 1.4 kN/s and subsequently reloaded to 200 MPa in accordance with the procedure illustrated in Figure 3.3-3. The stress relaxation experimental data and stress exponent analysis of this test can be seen in Figure 3.5-9 - Figure 3.5-12.

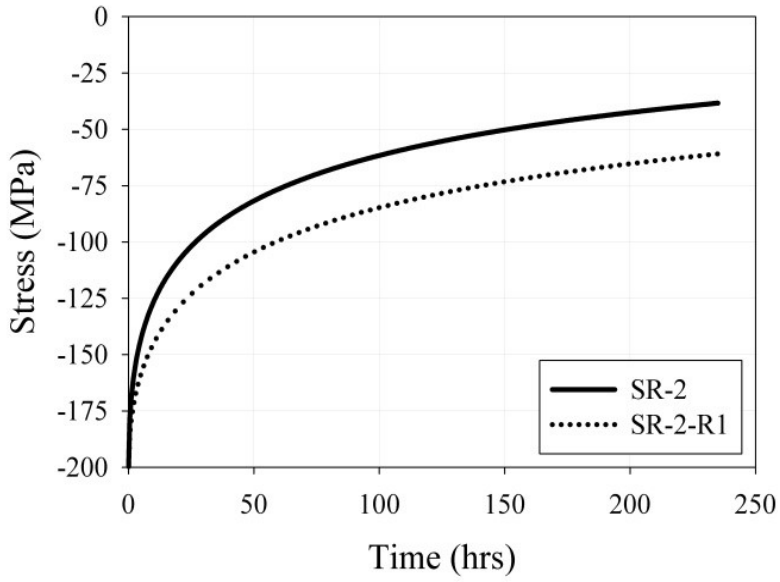

Figure 3.5-9: Stress vs. time for initial (SR-2) and reload (SR-2-R1) IN617 stress relaxation test specimens. The amount of stress relaxation decreases upon reloading of the previously relaxed specimen.

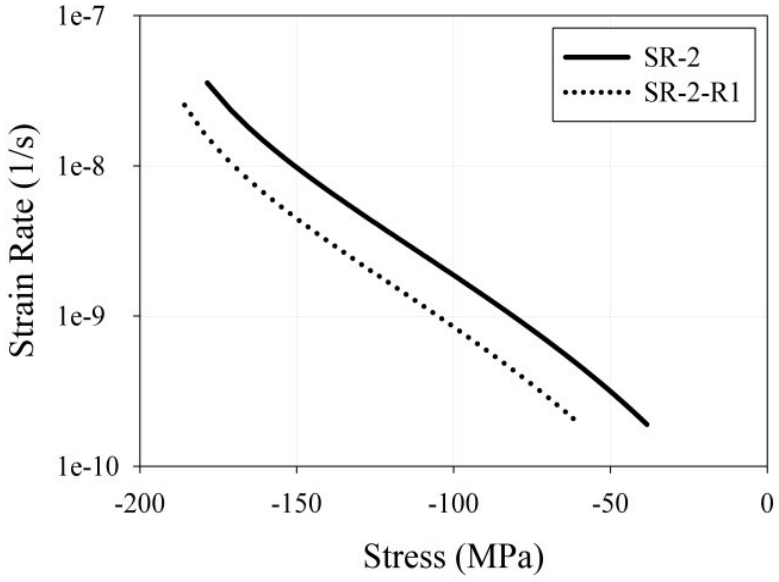

Figure 3.5-10: Strain rate vs. stress for initial (SR-2) and reload (SR-2-R1) IN617 stress relaxation test specimens.

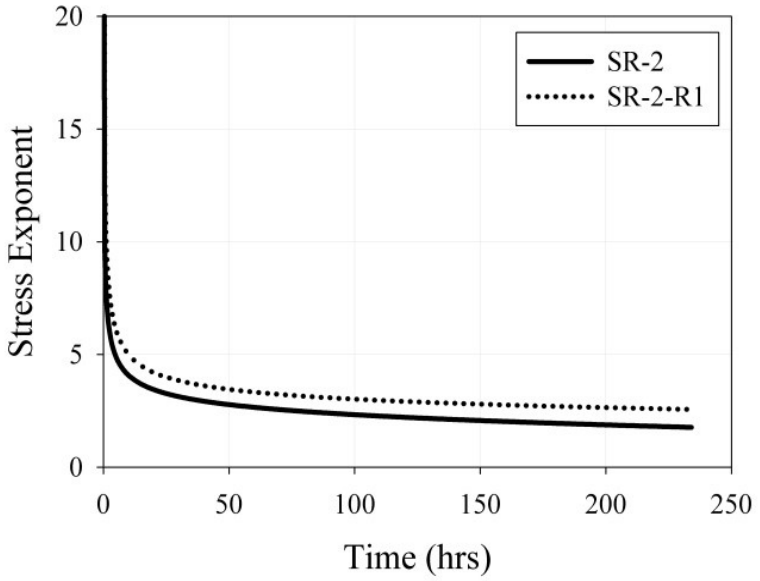

Figure 3.5-11: Stress exponent vs. time for initial (SR-2) and reload (SR-2-R1) IN617 stress relaxation test specimens.

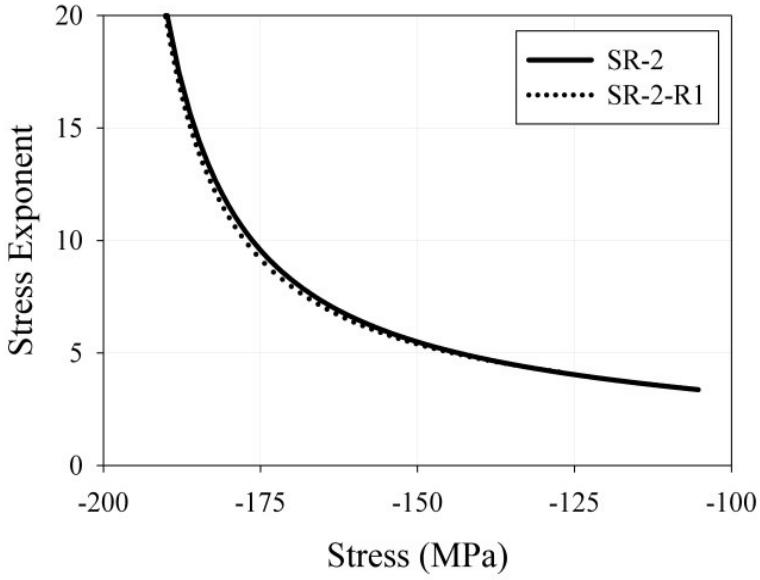

Figure 3.5-12: Stress exponent vs. stress for initial (SR-2) and reload (SR-2-R1) IN617 stress relaxation test specimens.

It is expected, from inspection of Figure 3.5-12, that the microstructure has remained constant during testing of SR-2 and SR-2-R1, as the stress exponent for a given stress was consistent between both cycles. The difference in relaxation response of SR-2 and SR-2-R1 occurs predominately within the first 36 hours of relaxation, after which both cycles exhibit similar relaxation rates, as shown in Figure 3.5-13. It is considered that the initial suppression of relaxation is related to the presence of extrinsic grain boundary dislocations released by the matrix during the first cycle.

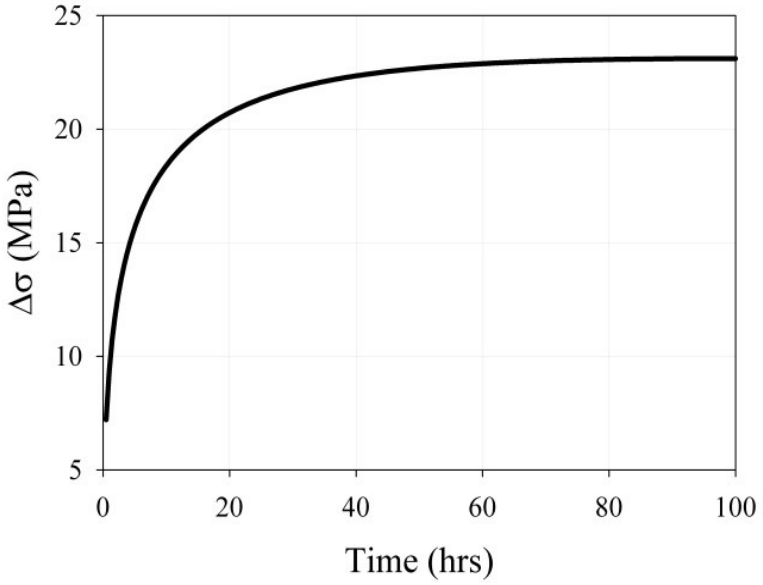

Figure 3.5-13: Difference in relaxed stress between specimens SR-2 and SR-2-R1. After approximately 36 hours, there is a negligible change in stress between the two cycles.

With the appropriate initial conditions, it was desired to execute the coupled, physics-based model in a serial fashion depicted in Figure 3.5-15. As grain boundary sliding had already occurred in the SR-2 test specimen, the initial

conditions used for the SR-2-R1 simulation changed relative to that of the SR-2 specimen; inelastic displacement accumulated from previous cycle, the elastic strain of the grain along the grain-grain boundary interface, as well as the number of dislocations within the grain boundary. Beyond 22 hours of stress relaxation, the calculated values of n_m, n_p , and n_{gb} for all specimens began to exhibit saturation behavior, as shown in Figure 3.5-6 – Figure 3.5-8. The calculated inelastic grain boundary sliding displacement for all specimens, as shown in Figure 3.5-2, did not exhibit the same saturation, but rather appeared to trend toward a linear behavior. In considering the stress exponent value and observation of these simulation behaviors, it was determined that 36 hours (denoted by t_B in Figure 3.5-14) would be the point in time from which to restart the SR-2 simulation in an attempt to predict the SR-2-R1 test results. After 36 hours, the stress exponent of the SR-2 specimen fell below a value of three, which evidenced a shift in mechanism away dislocation climb-controlled creep[14]. Using the same methodology by which the simulation results were produced in the previous section, the profiles for n_m and n_{gb} were extended by re-running the SR-2 simulation to the 36 hour threshold. Analysis of the simulation results showed that at 36 hours, the values of n_m and n_{gb} for the SR-2 specimen had saturated to a reasonable extent.

Figure 3.5-14 illustrates the loading procedure for the SR-2 and SR-2-R1 stress relaxation specimens. After the SR-2 specimen had been allowed to relax from Point (1) to Point (2), it was unloaded. The elastic strain at the matrix-grain boundary which remains as a result of the inelastic sliding which occurred between

Point (1) and Point (2), along with the number of dislocations absorbed by the grain boundary, is approximated by the values of the SR-2 simulation (specifically Eq. [3.2-1] and Eq. [3.2-2]) evaluated at 36 hours (t_B). These values are used as initial conditions for simulation of the SR-2-R1 specimen, as illustrated in Figure 3.5-14 and Figure 3.5-15.

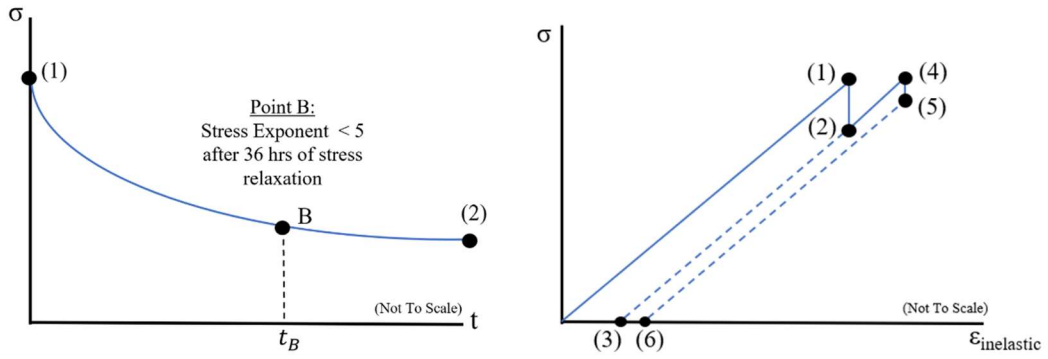

Figure 3.5-14: Overview of the initial (SR-2) and repeated (SR-2-R1) stress relaxation tests accompanied by the process flow for the simulation used to predict the creep strain behavior of SR-2-R1. The initial stress relaxation test consists of loading the specimen (SR-2) to a compressive stress depicted by Point (1). The specimen relaxes to Point (2) and is unloaded along the path made by Point (2) and Point (3). The reloading to perform the second stress relaxation test of the specimen (SR-2-R1) follows the path from Point (3) to Point (4), which is the same stress magnitude as the initial stress achieved at Point (1) from the previous test. The specimen then relaxes to a stress state represented by Point (5), and is then unload from Point (5) to Point (6).

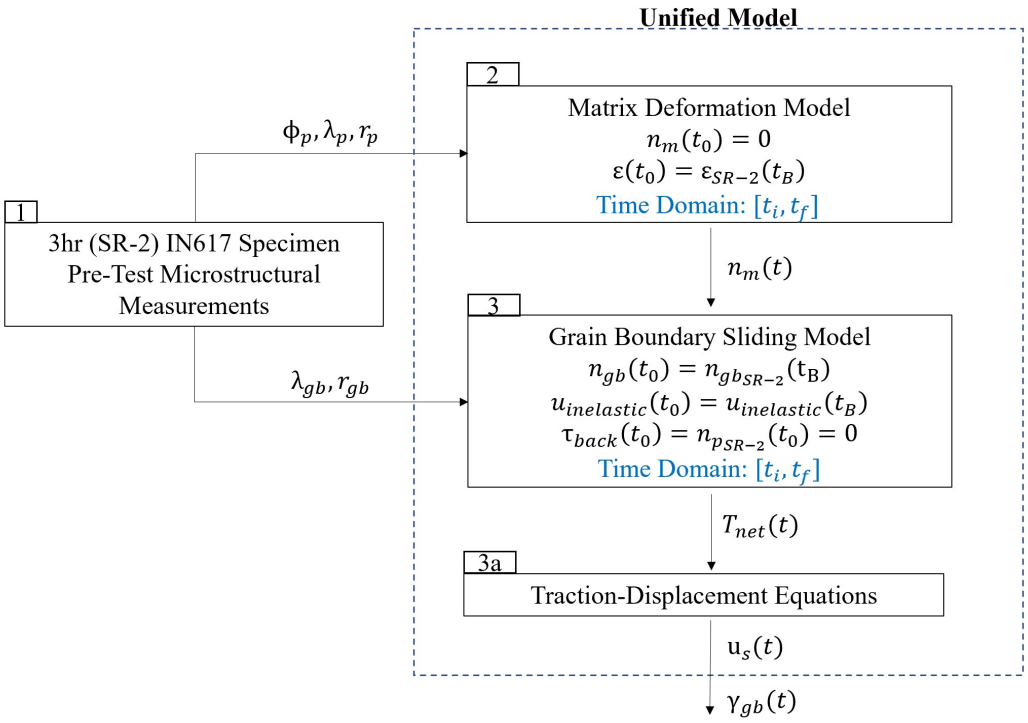

Figure 3.5-15: Flowchart representation of how the SR-2 stress relaxation specimen test and simulation results provide initial conditions for simulation of the reload, SR-2-R1. The microstructural measurements taken from the pre-test SR-2 specimen are held constant as the test temperature is established such that no microstructural change will occur. The value of n_{gb} at 36 hours from the simulation results presented Figure 3.5-7(B) is used as the initial condition for the grain boundary dislocation population for the SR-2-R1 simulation. The initial value of n_m for the SR-2-R1 simulation is taken to be zero, along with the initial value of the dislocation pileup, n_p. The initial strain, ε_0, is the irrecoverable strain of the matrix which occurred during the first stress relaxation experiment (SR-2).

The initial value of n_p for the SR-2-R1 simulation is taken to be zero. This is due to the fact that the load was removed between the initial (SR-2) and reload (SR-2-R1) stress relaxation tests. In the absence of an applied force, there is no motivation for the dislocation pile-up to form. These initial conditions can then be applied to Eq. [3.2-2]. The elastic strain which was generated at the grain-grain boundary interface from the sliding during the SR-2 stress relaxation test results in

a residual elastic strain of the matrix. As the grain and grain boundary remain coherent, the amount of elastic strain which has occurred within the grain – and subsequently accommodated by the viscoplastic sliding of the grain boundary – cannot be recovered. This irrecoverable strain can be simply envisioned as illustrated in Figure 3.5-16.

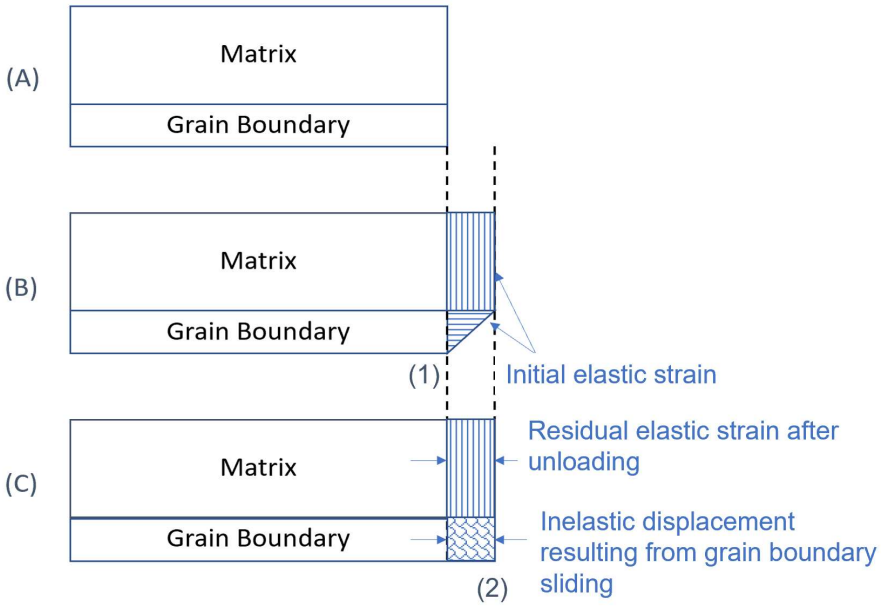

Figure 3.5-16: Simplified illustration showing (A) the representative grain-grain boundary interface prior to loading (B) the resulting initial elastic deformation following the applied load (C) the irrecoverable elastic strain within the matrix which results from the inelastic sliding of the grain boundary. Point (1) and Point (2) illustrate the inelastic grain boundary sliding process which corresponds to relaxation between Point (1) and Point (2) in Figure 3.5-14.

As the microstructure of the SR-2 and SR-2-R1 specimens are held constant at the test temperature of 780 °C, the values of $M_{23}C_6$ carbide volume fraction, radius, and spacing remain known. Once the SR-2-R1 stress relaxation experiment

had been conducted, the stress relaxation data was then used to produce a creep strain curve (as described by Eq. [3.5-3]) representative of a constant stress of 200 MPa at 780 °C. Figure 3.5-17 shows the curve-fitted creep strain behavior (converted from SR-2-R1 stress relaxation data via the previously presented[35]) compared to that of SR-2-R1 model simulation prediction using initial conditions established from the first stress relaxation test (SR-2) as described above.

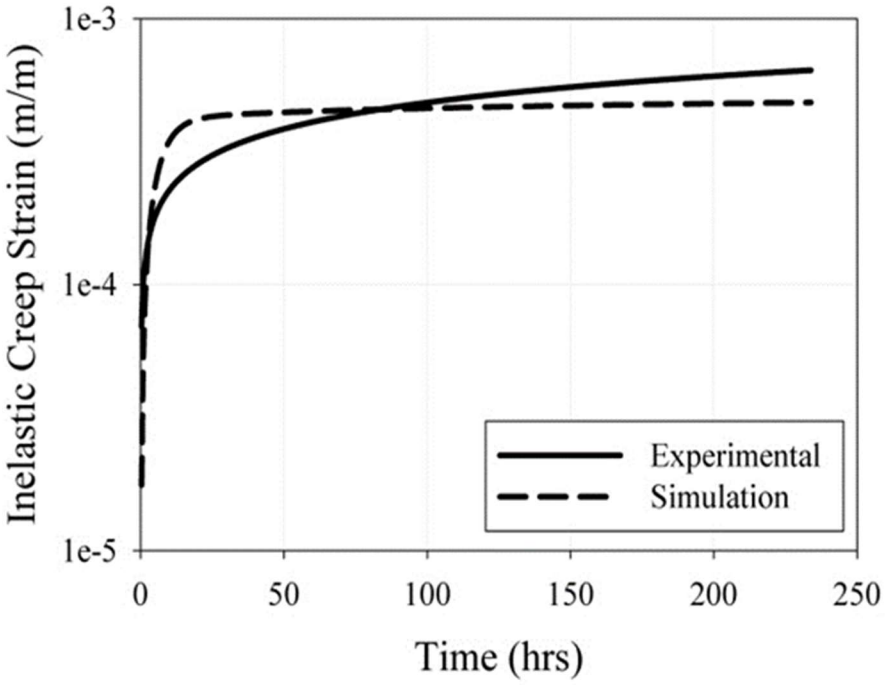

Figure 3.5-17: Comparison of the SR-2-R1 creep data (converted from the stress relaxation experimental data) and coupled matrix-grain boundary sliding simulation results for the SR-2-R1 IN617 specimen at a constant creep stress of 200 MPa at 780 °C.

Figure 3.5-17 shows that the coupled physics-based model previously developed[35] reasonably predicts the primary creep strain behavior of the SR-2-R1 IN617 specimen. The exponential rise of the creep strain which characterizes

the primary creep regime is well captured by the model with respect to rise time. The model somewhat overshoots the saturation value of the primary creep regime the model and predicts a slightly higher value than what is seen experimentally. The rate and value of creep strain saturation were found to be sensitive to the constant value selected to represent the grain boundary viscosity, η. Sensitivity studies performed in the generation of Figure 3.5-3 - Figure 3.5-6 also revealed that depending on the value of η chosen, the magnitude to, and rate at which, backstress accumulates is directly impacted.

3.6 Discussion

The value of the grain boundary viscosity influences the grain boundary sliding rate through the relationship established in Eq. [3.5-9]. In each of the model simulations for the test specimens, a simplifying assumption was made in which the grain boundary viscosity was assumed to be constant with respect to time. This is similar to the approach taken by Raj and Ashby[45] in their treatment of grain boundary viscosity with respect to grain boundary diffusion facilitated sliding, which they approximated through the use of Eq. [3.6-1]:

$$\eta = \frac{1}{132}\left(\frac{d_{grain}^3 kT}{\delta D_{GB}\Omega}\right) \qquad [3.6\text{-}1]$$

where d_{grain} is the grain diameter, k is Boltzmann's constant, T is temperature, D_{GB} is the diffusion coefficient for grain boundary diffusion, δ is the grain boundary thickness, and Ω is the atomic volume. Ashby[30] later revised and included in his grain boundary viscosity definition the dependency of dislocation

spacing within the grain boundary. This definition of viscosity was then defined to have lower and upper bound values as established in Eq. [3.6-2]:

$$\frac{kT}{8bD_{GB}} \leq \eta \leq \frac{kT}{8bD_{GB}\left(\rho_{gb}\lambda\right)} \qquad [3.6\text{-}2]$$

where ρ_{gb} is the density of grain boundary dislocations and λ is a given unit length. As dislocations enter the grain boundary from within the matrix, the dislocation-to-dislocation spacing decreases. As Ashby indicated, the power required for dislocation glide varies in a manner proportional with the square of its glide velocity. More directly, as ρ_{gb} approaches the maximum value of (1/λ), spacing decreases, followed by a decrease in boundary viscosity[30]. As such, an improvement on the physics-based deformation model presented in the previous work[35] is likely to come from the incorporation of a time-dependent viscosity term in the form of:

$$\eta = f\left\{n_{gb}(t), D_{gb}, k, T\right\} \qquad [3.6\text{-}3]$$

Analysis of the simulation results, specifically the rate at which dislocations enter the grain boundary from the matrix and enter the grain boundary pileup, provides a basis that suggests the grain boundary viscosity may be best described through use of a power law relationship, initially at a maximum value which subsequently saturates to a minimum. This can be physically rationalized by realizing that prior to subjecting the material to a creep (or stress relaxation) service environment, the grain boundary dislocation spacing can be

taken to relatively large as the grain has not been releasing dislocations for grain boundary absorption. As time progresses, more dislocations enter and occupy the grain boundary volume, thereby decreasing the dislocation-to-dislocation spacing. The grain boundary viscosity will decrease until it reaches its saturation limit which corresponds to the grain boundary's inability to absorb more dislocations until climb or annihilation occurs[12],[28].

A comparison of Figure 3.5-8 with the stress relaxation data suggests that even though the difference in matrix microstructure of test specimens SR-2 and SR-3 results in a rather significant difference in the number of matrix dislocations released, the grain boundary carbide spacing exerts influence over the amount of relaxation. As the difference in grain boundary carbide spacing between test specimens SR-2 (1.39 microns) and SR-3 (1.16 microns) is marginal, it is then reasoned that the difference in the number of dislocations which can be accommodated is proportionally marginal. This is supported by the fact that the dislocation pileup within the grain boundary saturates to a lower value and at a faster rate than calculated for the SR-1 specimen, as shown in Figure 3.5-6. By comparison, the back stress calculated for SR-2 and SR-3 reaches its maximum value quicker, thereby reducing the amount of effective stress which is promoting the grain boundary sliding (and subsequent relaxation) in a more rapid fashion than which occurs in test specimen SR-1. With respect to the grain boundary, as seen in Figure 3.5-3 the backstress appears to saturate to a similar value for all stress relaxation specimens, whereas the net stress shown in Figure 3.5-4 appears to saturate to different values unique to each specimen. This arises as a result of the

climb-facilitated recovery rate being different for each specimen due to differences in grain boundary carbide radius.

The solutioned-only test specimen, SR-1 – which had negligible $M_{23}C_6$ matrix and grain boundary carbide precipitation – showed drastically different model simulation results. Figure 3.5-8 reveals that the number of matrix dislocations released, as well as the rate, is significantly higher than that of either SR-2 or SR-3 specimens. With the increase in matrix dislocation release stemming from a clean matrix, the number of dislocations able to be absorbed by the boundary with a greater characteristic length in which to accommodate them, the amount of grain boundary sliding and inelastic strain increases significantly, as seen in Figure 3.5-2.

For specimen SR-1, the characteristic length of the grain boundary, λ_{gb}, was approximated as the length of one side of a hexagon with the simplified circular grain (measured diameter, d_{grain}) circumscribed within it. As such, the length over which the dislocations are able to pile up was significantly larger than the other specimens which contained grain boundary carbides. The simulation results shown in Figure 3.5-5 indicate a noticeably higher value of $\left(\frac{dn_p}{dt}\right)$ for specimen SR-1 relative to that of SR-2 and SR-3. This observation is not initially intuitive, as SR-2 and SR-3, have shorter characteristic lengths over which the dislocation pile-ups are forming compared to that of SR-1. This may suggest, in agreement with the work of Wu *et al.*[15], that the grain boundary carbide spacing exerts, in addition

to the matrix microstructure, a significant influence over the amount of grain boundary sliding which can be expressed.

3.7 Conclusions

Four, high temperature stress relaxation tests are performed on IN617 specimens of three distinct heat treatments. Prior to conducting the high temperature stress relaxation tests, four overall heat treatment combinations were analyzed via SEM and shown to result in four unique microstructural states of matrix and grain boundary $M_{23}C_6$ carbide precipitation. The matrix and grain boundary carbides were characterized through quantitative microscopic techniques which provided radius, volume fraction, and spacing.

The solutioning temperature of 1200 °C was chosen such that it would exceed the $M_{23}C_6$ carbide solvus temperature, thereby dissolving any $M_{23}C_6$ carbide formation prior to thermal aging treatments. The thermal aging treatments carried out at 1000 °C produced varying levels of precipitation of $M_{23}C_6$ carbides within the grain and grain boundary, which provided different "snapshots in time" of the microstructural evolution which occurs in IN617. The high temperature stress relaxation tests were performed at a temperature of 780°C and initial stress of 200 MPa. The test temperature of 780 °C was selected as it is above the γ' solvus temperature for IN617 and below that of the $M_{23}C_6$ solvus temperature[8],[17]. In doing this, any changes in precipitation beyond that which occurred in the prescribed heat treatment were effectively eliminated, allowing for experimental data to be produced with a constant microstructure that could then

be used as input for the previously established physics-based model[35]. The initial stress was chosen such that the test conditions would provide the requisite combination of temperature and stress such that high temperature dislocation creep would be the active mechanism[46], but low enough such that the material yield strength at the test temperature would not be exceeded.

The stress relaxation rate observed for test specimens SR-1, SR-2, and SR-3 was then used to produce equivalent creep curves using a graphical interconversion technique[42]. Using the methodology established in the previous work[35], the physics-based model could be used to examine the physical premise coupling the intragranular and intergranular regions through the dislocation release and subsequent grain boundary dislocation population terms, n_m and n_{gb}. Unlike in the preliminary simulations, the simulations used to analyze the SR-1, SR-2, and SR-3 specimens considered the as-tested conditions, in which the matrix and grain boundary carbide size and spacing were constant. The simulation results confirmed the preliminary assessments, showing that with increasing matrix carbide size and volume fraction (accompanied by the corresponding decrease in spacing) resulted in fewer dislocations being able to arrive to the grain boundary. Given the difference in values of n_m for the SR-2 and SR-3 specimens being noticeably larger than that which is seen in their corresponding n_{gb}values (shown in Figure 3.5-8 and Figure 3.5-7, respectively), this suggests that grain boundary carbide spacing plays a significant role in the formation of the pileup and must be considered.

An additional stress relaxation test was performed on the SR-2 test specimen (SR-2-R1), in which the same initial stress of 200 MPa was reapplied after the initial relaxation exhibited saturation behavior. Initial conditions for terms n_m, n_{gb}, n_p, and elastic strain within the matrix were determined for the SR-2-R1 test specimen through running of the uncoupled constituent matrix and grain boundary sliding deformation models for test specimen SR-2. The initial conditions were then used in the coupled model, whereby the matrix deformation model output a time-dependent value of dislocations able to be absorbed by the boundary (n_m) which was then considered additive to the grain boundary dislocation population (n_{gb}). The rate of change of the dislocation pileup at a grain boundary obstacle (i.e. carbide) could then be used to determine the backstress generated and utilized in a traction-displacement relationship. The traction-displacement law is subsequently used to determine the rate of inelastic grain boundary sliding. Once the SR-2-R1 stress relaxation experimental data could be converted to an equivalent creep strain curve, it was shown that the physics-based model was capable of reasonably predicting the creep strain behavior of the SR-2-R1 specimen.

The model results slightly over-estimate the saturate primary creep strain at a time earlier than what is seen experimentally. The assumption of a constant grain boundary viscosity appears to play a significant role in the rate and saturation value of the primary creep regime and requires further investigation into its variable nature resulting from the time-dependent increase in grain boundary dislocation population.

CHAPTER 4

RECOMMENDATIONS FOR FUTURE WORK

- The physics-based model is a unified model which couples the matrix deformation occurring during creep with that of the grain boundary sliding which provides viscoplastic accommodation. The matrix deformation component of the coupled grain-grain boundary deformation model was initially written/designed to be capable of incorporating time-dependent microstructure into the calculation of the release of matrix dislocations, whereas the grain boundary sliding component of the coupled grain-grain boundary model, at this stage, was not. The experimental design of the work presented herein eliminated the time-dependency of the microstructure. A potential next step involved in this research would be to incorporate the ability for time-dependent microstructural inputs to be used within the grain boundary sliding component of the model. This would allow for simulation of creep tests in which in-service microstructural evolution occurs, which is very often the case in industrial applications where IN617 is used.
- The significance of the assumed constant value of the grain boundary viscosity was shown to be very influential in the response of the grain boundary as it pertained to dislocation pileup and backstress generation. The further study of grain boundary viscosity characterization and development of viscosity function which is able to capture and account for the number of

dislocations within the grain boundary would be very useful in increasing the capability and robustness of the unified model.

As the rate at which dislocations enter the grain boundary from the matrix, the characteristic length of the grain boundary, as well as the size and density of $M_{23}C_6$ grain boundary carbides, is almost always a unique combination of parameters which dictates the grain boundary dislocation population and kinetics. Therefore, a viscosity function that is microstructure-independent would likely be most advantageous.

- As the unified, physics-based model presented is currently a series of Matlab® routines which employ primarily analytical treatments that are carried out in a serial fashion, the adaptation of the model to a finite element method subroutine is the next logical step in its development. The use of numerical techniques in a user-defined subroutine would allow for extrapolation of the simplified single crystal - grain boundary model presented here to much larger analyses involving the full-scale modeling of polycrystalline material. This would bolster the accuracy and usefulness of the model as it would provide insight into macroscopic-level material behavior, where the effects of adjacent grain and grain boundaries of various angles can be analyzed simultaneously.
- The unified model presented is primarily used in the investigation of the early stages of creep (primary to steady state). Tertiary creep occurs through damage mechanisms involving void formation, coalescence, and crack

propagation. Though the mechanisms are not considered as part of this model, they are nonetheless important. When applying this model to predict conventional creep behavior, it has been suggested that there are critical grain boundary characteristic lengths which govern the rate of grain boundary sliding-facilitated creep crack growth[29],[47],[48]. The calculation and incorporation of a critical displacement of sliding within the grain boundary (which is a function of the grain boundary microstructure) could prove to be useful in extending the model in its current state to incorporate damage considerations and subsequent modeling of tertiary creep behavior.

BIBLIOGRAPHY

[1] S. Kihara, J. B. Newkirk, A. Ohtomo, and Y. Saiga, "Morphological changes of carbides during creep Inconel 617 at 1000C," *Metall. Trans. A*, vol. 11, pp. 1019–1031, 1980.

[2] S. Metals, "Inconel Alloy 617." p. Publication Number SMC-029, 2005.

[3] D. Chapin, S. Kiffer, and J. Nestell, "The Very High Temperature Reactor: A Technical Summary," 2004.

[4] K. Maciejewski, "The Role of Microstructure on Deformation and Damage Mechanisms in a Ni-based Superalloy at Elevated Temperatures," The University of Rhode Island, 2013.

[5] A. K. Jena and M. C. Chaturvedi, "Role of Alloying Elements for Nickel Superalloys," *J. Mater. Sci.*, vol. 19, pp. 3121–3139, 1984.

[6] G. Dieter, *Mechanical Metallurgy*, 3rd ed. McGraw-Hill, 1986.

[7] J. P. Hirth, "The influence of grain boundaries on mechanical properties," *Metall. Trans.*, vol. 3, no. 12, pp. 3047–3067, 1972.

[8] S. Xu, J. I. Dickson, and A. K. Koul, "Grain growth and carbide precipitation in superalloy, UDIMET 520," *Metall. Mater. Trans. A*, vol. 29, no. 11, pp. 2687–2695, 1998.

[9] S. Chomette, J. M. Gentzbittel, and B. Viguier, "Creep behaviour of as received, aged and cold worked INCONEL 617 at 850C and 950C," *J. Nucl. Mater.*, vol. 399, no. 2–3, pp. 266–274, 2010.

[10] A. Soula *et al.*, "Analysis of high-temperature creep deformation in a polycrystalline nickel-base superalloy," vol. 511, pp. 301–306, 2009.

[11] K. Thibault, D. Locq, P. Caron, D. Boivin, Y. Renollet, and Y. Bréchet, "Influence of microstructure on local intra- and intergranular deformations during creep of a nickel-based superalloy at 700°C," *Mater. Sci. Eng. A*, vol. 588, pp. 14–21, 2013.

[12] B. Alexandreanu, B. H. Sencer, V. Thaveeprungsriporn, and G. S. Was, "The effect of grain boundary character distribution on the high temperature deformation behavior of Ni-16Cr-9Fe alloys," *Acta Mater.*, vol. 51, no. 13, pp. 3831–3848, 2003.

[13] T. Langdon, "Grain Boundary Sliding As A Deformation Mechanism During Creep," *Philos. Mag.*, vol. 22, no. 178, pp. 689–700, 1970.

[14] F. T. Furillo, J. M. Davidson, J. K. Tien, and L. A. Jackman, "The effects of grain boundary carbides on the creep and back stress of a nickel-base superalloy," *Mater. Sci. Eng.*, vol. 39, no. 2, pp. 267–273, 1979.

[15] X. J. Wu and A. K. Koul, "Grain boundary sliding in the presence of grain boundary precipitates during transient creep," *Metall. Mater. Trans. A*, vol. 26, no. 4, pp. 905–914, 1995.

[16] X. Wu, S. Williams, and D. Gong, "A true-stress creep model based on deformation mechanisms for polycrystalline materials," *J. Mater. Eng. Perform.*, vol. 21, no. 11, pp. 2255–2262, 2012.

[17] W. . Mankins, J. . Hosier, and T. . Bassford, "Microstructure and Phase Stability of INCONEL Alloy 617," *Metall. Trans.*, vol. 5, no. 2, pp. 2579–2590, 1974.

[18] D. A. Balantic, M. Jenko, F. Vodopivec, and R. Celin, "Effect of Change of Carbide Particles Spacing and Distribution on Creep Rate of Martensite Creep Resistant Steels," vol. 45, no. 6, pp. 555–560, 2011.

[19] B. F. Dyson, "Microstructure Based Creep Constitutive Model for Precipitation Strengthened Alloys: Theory and Application," *Mater. Sci. Technol.*, vol. 25, no. 2, pp. 213–220, 2009.

[20] A. Manonukul, F. P. . Dunne, and D. Knowles, "Physically-based model for creep in nickel-base superalloy C263 both above and below the gamma solvus," *Acta Mater.*, no. 50, pp. 2917–2931, 2002.

[21] E. El-Magd, G. Nicolini, and M. Farag, "Effect of carbide precipitation on

the creep behavior of Alloy 800HT in the Temperature Range 700 °C to 900 °C," *Metall. Mater. Trans. A*, vol. 27, no. 3, pp. 747–756, 1996.

[22] J. Rosler and E. Arzt, "The Kinetics of Dislocation Climb Over Hard Particles-I. Climb without Particle-Dislocation Interaction," *Acta Metall.*, vol. 36, no. 4, pp. 1043–1051, 1988.

[23] E. Arzt and J. Rösler, "The kinetics of dislocation climb over hard particles-II. Effects of an attractive particle-dislocation interaction," *Acta Metallurgica*, vol. 36, no. 4. pp. 1053–1060, 1988.

[24] W. J. Liu and J. J. Jonas, "A stress relaxation method for following carbonitride precipitation in austenite at hot working temperatures," *Metall. Trans. A*, vol. 19, no. 6, pp. 1403–1413, 1988.

[25] H. Fukutomi, H. Takatori, and R. Horiuchi, "Grain Boundary Sliding with and without Matrix Slip Deformation in Cadmium Bicrystals," *Trans. Japan Inst. Met.*, vol. 23, no. 10, pp. 579–584, 1982.

[26] A. D. Sheikh-Ali and J. A. Szpunar, "Stimulation and Suppression of Grain Boundary Sliding by Intragranular Slip in Zinc Bicrystals," pp. 439–450, 2003.

[27] T. L. Lin and D. McLean, "Changes Produced by Deformation in Grains and Grain Boundaries of Nickel," *Metal Science Journal*, vol. 2, no. 1. pp. 108–113, 2010.

[28] A. H. Pshenichnyuk, V. V. Astanin, and O. A. Kaibyshev, "The model of grain-boundary sliding stimulated by intragranular slip," *Philos. Mag. A Phys. Condens. Matter, Struct. Defects Mech. Prop.*, vol. 77, no. 4, pp. 1093–1106, 1998.

[29] J. Dahal, "Grain Boundary Deformation and Damage Mechanisms in Intergranular Crack Growth of a Nickel Based Superalloy," University of Rhode Island, 2011.

[30] M. F. Ashby, "Boundary Defects, And Atomistic Aspects of Boundary

Sliding and Diffusional Creep," *Surf. Sci.*, vol. 31, pp. 498–542, 1972.

[31] Amiya Mukherjee, "The Rate Controlling Mechanism in Superplasticity," *Mater. Sci. Eng.*, vol. 8, no. 2, pp. 83–89, 1971.

[32] D. and B. Hull D.J., " Introduction to Dislocations (third edition).," *Pergamon Press Pergamon Press*, vol. Oxford, 2, p. Oxford, 252 pp, 1984.

[33] A. Shirzadi and S. Jackson, *Structural Alloys for Power Plants - Operational Challenges and High-temperature Materials*. Cambridge, UK: Woodhead Publishing, 2014.

[34] J. Friedel, *Dislocations*. Pergamom Press, 1964.

[35] M. Lapera, D. Spader, and H. Ghonem, "A Coupled, Physics-Based Intra- and Intergranular Model for High Temperature Creep of Nickel-Based Superalloy Inconel 617 – I. Model Concepts and Formulation," pp. 1–23.

[36] Y. Ishida and M. Henderson Brown, "Dislocations in Grain Boundaries and Grain Boundary Sliding," *Acta Metall.*, vol. 15, no. 5, pp. 857–860, 1967.

[37] G. P. Sabol and R. Stickler, "Microstructure of Nickel-Based Superalloys," *Phys. Status Solidi*, vol. 35, no. 1, pp. 11–52, 1969.

[38] K. Mo, "Microstructural Evolution and Mechanical Behavior of Nickel Based Alloys for Very High Temperature Reactor," University of Illinois at Urbana-Champaign, 2011.

[39] M. S. Rahman, G. Priyadarshan, K. S. Raja, C. Nesbitt, and M. Misra, "Characterization of High Temperature Deformation Behavior of INCONEL 617," *Mech. Mater.*, no. 41, pp. 261–270, 2009.

[40] W. F. Knoff and I. L. Hopkins, "An improved numerical interconversion for creep compliance and relaxation modulus," *J. Appl. Polym. Sci.*, vol. 16, no. 11, pp. 2963–2972, 1972.

[41] R. S. Anderssen, A. R. Davies, and F. R. De Hoog, "On the Volterra integral equation relating creep and relaxation," *Inverse Probl.*, 2008.

[42] G. S. Vorotnikov and B. M. Rovinskii, “Stress Relaxation, Creep, and Uniaxial Strain: General and Special Features,” *J. Appl. Mech. Tech. Phys.*, vol. 7, no. 6, pp. 19–26, 1966.

[43] I. L. Hopkins and R. . Hamming, “On Creep and Relaxation,” *J. Appl. Phys.*, vol. 28, no. 8, pp. 906–909, 1957.

[44] Y. Il Jung, Y. N. Seol, B. K. Choi, and J. Y. Park, “Behavior of stress-relaxation and the estimation of creep in Zr-1.1Nb-0.05Cu alloy,” *Mater. Des.*, vol. 42, pp. 118–123, 2012.

[45] R. Raj and M. F. Ashby, “On grain boundary sliding and diffusional creep,” *Metall. Trans.*, vol. 2, no. 4, pp. 1113–1127, 1971.

[46] H. J. Frost and M. F. Ashby, *Deformation Mechanism Maps : The Plasticity and Creep of Metals and Ceramics*. Pergamom Press, 1982.

[47] S. Xu, X.-J. Wu, A. K. Koul, and J. I. Dickson, “An intergranular creep crack growth model based on grain boundary sliding,” *Metall. Mater. Trans. A*, vol. 30, no. 4, pp. 1039–1045, 1999.

[48] S. Xu, A. K. Koul, and J. I. Dickson, “Creep crack growth in the absence of grain boundary precipitates in UDIMET 520,” *Metall. Mater. Trans. A Phys. Metall. Mater. Sci.*, vol. 32, no. 13, pp. 795–804, 2001.

APPENDICES

APPENDIX A

Matrix Deformation Model

Function File Name: improved_euler_heaviside_D.m
Description: Driver File for Matrix Deformation Model

```
clc
clear all

%%Constants

E=159E9; %Young's Modulus [Pa] at 780C
G=E/sqrt(3); %Shear Modulus [Pa]

rho_0=10E10; %Initial number of mobile dislocations [# of dislocations/m^2]
sigma=200E6;    %Applied Stress [Pa]
t_max=234*3600; %Time domain of interest

%Backstress (both terms) opposing dislocation climb is time-dependent and can
%be calculated from the volume fraction with the underlying assumption of a
%square lattice and equal spacing (same assumption made previously)

% For Use Only With Time-Dependent Microstructure
        [rad,vol]=ExpRiDec2(1);

% For 30 hr SR Specimen
        rad=2.5E-10;
        vol=68E-6;
        sheet='0hr';

% For 3 hr SR Specimen
        rad=6.2E-8;
        vol=0.0083;
        %sheet='3hr';
        sheet='3hrR1';

% For 30 hr SR Specimen
        rad=9.8E-8;
        vol=0.1123;
        sheet='30hr';
```

```
%% ODE Solver

%For simulation of the SR-2-R1 specimen, added anelastic shear strain from
%model at t=36 hours for 3 hr specimen.
%This is to capture the reloading of the matrix after it has relaxed and
%been "locked" in place by the irrecoverable grain boundary sliding. This
%value was determined using nm_ngb_forward.m
init=[(sigma/E); rho_0; 0]; %for 0hr, 3hr, and 30 hr SR specimens

%Otherwise, use this initialization array for a new run
init=[((sigma/E)+5.5014e-04); rho_0; 0];

dt = 1;
t0 = 0;
x0=init';

t=zeros(t_max+1,1);
x=zeros(t_max+1,3);

t(1) = t0;
x(1,:) = x0;

for i=1:t_max

                f1=rad;
                f2=vol;
                [k0] = Intragranular_ODEs_nosigmai_heaviside_D(t0,x0,f1,f2);
                x1=x0+k0*dt;

                f1=rad;
                f2=vol;
                t1 = t0 + dt;
                [k1] = Intragranular_ODEs_nosigmai_heaviside_D(t1,x1,f1,f2);
                x1=x0+0.5*(k0+k1)*dt;
                t0=t1;
                x0=x1;

                t(i+1) = t0;
                x(i+1,:) = x0';
end
```

```
%%%%% Subplotting Block %%%%%

%Change the line color when running multiple simulations to be plotted on
%one figure
        color='r';
        disp('Calculating displacements...')
        format shorteng
        x(:,4)=x(:,1)*100E-6;
%Strain rate
        dedt=diff([eps;x(:,1)])./diff([eps;t(:)]);
        dedt=dedt./x(:,1);
        x(:,5)=dedt;
%Store n_m and time in order to pass to GBS code (later)
        n_m=x(:,3);
        time=t(:);
%Plotting
        figure
        subplot(2,2,1)
        plot(t,rad,color)
        hold on
        title('Carbide Radius Time Profile');
        xlabel('Time (s)');
        ylabel('Radius (m)')
        subplot(2,2,2)
        plot(t,vol,color)
        hold on
        title('Carbide Volume Fraction Time Profile');
        xlabel('Time (s)');
        ylabel('Volume Fraction')
        subplot(2,2,3)
        plot(t,x(:,1),color)
        hold on
        title('Predicted Creep Strain');
        xlabel('Time (s)');
        ylabel('Strain (m/m)')
        subplot(2,2,4)
        plot(t,x(:,3),color)
        hold on
        title('Dislocations Available to GB for GBS')
        ylabel('Number of Dislocations Available')
        xlabel('Time (s)')
```

```
%%%Block to reduce data size and write out for easier data handling

% reduc=500; %%USER DEFINED sampled at every (reduc-1) intervals
% fileID=['Simulation Results_all_reduc_',num2str(reduc)];
% fopen(fileID);
% headers={'Time', 'Carbide Radius', 'Carbide Volume Fraction', 'Normal Strain',
'Dislocation Density','Number of Dislocations','Displacement','Normal Strain
Rate','Carbide Radius', 'Carbide Volume Fraction', 'Normal Strain','Dislocation
Density','Number of Dislocations','Displacement','Normal Strain Rate','Carbide
Radius', 'Carbide Volume Fraction', 'Normal Strain','Dislocation Density','Number
of Dislocations','Displacement','Normal Strain Rate'};

%%%Range of cells for headers

% xlsrange_headers='A1:V1';
% filename_read='Simulation Results_all';
% %Name of sheet to read in
% %filename_read_sheet='1a1b1c-output';
% filename_read_sheet='123-output';
% fulldat=xlsread(filename_read,filename_read_sheet);
% filename_write=fileID;
% %Name of sheet to write out
% %sheet2='1a1b1c-output-all';
% sheet2='123-output-all';
% xlswrite(filename_write,headers,sheet2,xlsrange_headers);


%%%Extracts initial values irrespective of sampling frequency, reduc

% reducdat=zeros(1,22); % # of columns to extract from
% reducdat(1,1)=0; %time zero
% reducdat(1,2:end)=[fulldat(1,1:end)]; %initial conditions
% k=2;
% time=reduc;

% %Extracts values at sampling frequency, reduc

% for i=reduc:reduc:size(fulldat,1)
%     reducdat(k,1)=time;
%     reducdat(k,2:end)=[fulldat(i,:)];
%     k=k+1;
```

```
%     time=time+reduc;
% end


%%%Assesses size of reduced data set and concatenates strings based on size in
order to write out to Excel file

% length=size(reducdat,1)+1; % +1 to account for column labels
% concat=['V',num2str(length)];
% xlsrange_data=['A2',':',concat];
% xlswrite(filename_write,reducdat(:,:),sheet2,xlsrange_data)
```

Function File Name: Intragranular_ODEs_nosigmai_heaviside_D.m
File Description: Ordinary Differential Equations for Matrix Deformation

```
function [strain_intra] = Intragranular_ODEs_nosigmai_heaviside_D(t,x,f1,f2)

T=780+273; %Temperature [K]
D=3E-18; %Intragranular Diffusion Coefficient
E=159E9; %Young's Modulus [Pa]
M=3; %Taylor Factor
G=E/sqrt(M); %Shear Modulus [Pa]
kb=1.38e-23; %Boltzmann's Constant
b=2.5E-10; %Burgers vector
f_atomic=6.7750e+020; %Atomic frequency

rho_0=10E10; %Initial number of mobile dislocations [# of dislocations/m^2]
sigma=200E6; %Applied Stress [Pa]
alpha=1E3; %Material constant

%%For time-dependent microstructure only – uses function handles to evaluate
matrix carbide radius and volume fraction at each time step
% if i==1
% [rad,vol]=ExpRiDec2(i);
% f1=rad(1,1);
% f2=vol(1,1);
% else
% end

%System of ODEs

%eps_dot - Strain Rate Eq.
strain_intra(1) = (1.6/M)*(alpha*x(2))*f2*(1-f2)*1E-3*(sqrt(pi/(4*f2))-
1)*c*D*sinh((sigma*b^2*(1.6*f1*1E-3*((pi/(4*f2))^1/2-1)))/(M*kb*T));

%rho_dot - Dislocation Evolution Eq.
strain_intra(2) = (480*alpha)*rho_0*x(2)*c*D*f2*(1-f2)*1E-3*(sqrt(pi/(4*f2))-
1)* sinh((sigma*b^2*(1.6*1E-3*f1*((pi/(4*f2))^1/2-1)))/(M*kb*T));

%r_c_dot - Rate of Dislocation Escape Eq.
strain_intra(3) =M*((1.6/M)*(alpha*x(2))*f2*(1-f2)*1E-3*(sqrt(pi/(4*f2))-
1)*c*D*sinh((sigma*b^2*(1.6*1E-3*f1*((pi/(4*f2))^1/2-1)))/(M*kb*T)))/...
 ((1.6*x(2))*b*f1*f2*(1-f2)*((pi/(4*f2))^1/2-1));
```

```
End
```

Function File Name: ExpRiDec2.m
File Description: Carbide Volume Fraction and Radius Function Handle Builder for Matrix Time-Dependent Microstructure

```
function [rad,vol]=ExpRiDec2(i)


%Exponential Rise and Decay Tool for Building Exponentially-Saturating
%Functions
%Exponential Rise Form

% A = B + C(1-exp(Dt))

% A == max/saturation value
% B == initial value
% C == arbitrary value that chosen such that log(-1*((A-B)/C)-1) is a real,
%positive number
% D == rise constant


%Enter saturation time
t_growth=14400; %sec
%Enter radius growth rate during coarsening
r_coarse=1E-16;
%Enter end of coarsening
t_coarse=21600; %sec
%Enter domain size
t_max=80000;

%Radius function coefficients
% %Enter max/saturation radius value
radA=4E-8; %m
%Enter initial value at time = 0
radB=2E-9; %m
%Enter constant
radC=1E-2;
%Decay Constant
radF=5E-6;

%Volume fraction function coefficients
%Enter max/saturation value
```

```
volA=0.286; %m
%Enter initial value at time = 0
volB=1E-2; %m
%Enter constant
volC=1000;
%Decay Constant
volF=5E-6;

%Pre-allocate radius and volume fraction arrays
f=zeros(t_max,2);

 radD=-2.6389e-10; %KEEP THIS ON FOR SIMULATION 1,2,3
 %radD=-1.0000E-12; %TURN THIS OFF - ONLY ON FOR SIMULATION
1.A,1.B,1.C STUDY

 volD=-1.9169e-08; %KEEP THIS ON FOR SIMULATION 1,2,3
 %volD=-3.2E-9; %TURN THIS OFF - ONLY ON FOR SIMULATION
1.A,1.B,1.C STUDY

% Function Handles Used for Building Arrays

f1r = @(k)radB+radC*(1-exp(radD*k));
f1v = @(k)volB+volC*(1-exp(volD*k));
f2r = @(k,Cr)Cr+r_coarse*(k-t_growth);
f2v = @(k,Cv)Cv;
f3r = @(k,radE)radE*exp(-radF*(k-t_coarse));
f3v = @(k,volE)volE*exp(-volF*(k-t_coarse));

rad = zeros(t_max,1);
vol = zeros(t_max,1);
rad(1,1)=radB;
vol(1,1)=volB;

%Conditional structure that allows for function switching depending on regime of
Ostwald Ripening (growth vs. coarsening vs. dissolution)
for k=2:t_max+1
   if k <=t_growth
      rad(k) = f1r(k);
      vol(k) = f1v(k);
   elseif k >t_growth && k <=t_coarse
      Cr=rad(t_growth);
      Cv=vol(t_growth);
      rad(k) = f2r(k,Cr);
      vol(k) = f2v(k,Cv);
   else k > t_coarse
```

```
        radE=rad(t_coarse);
        volE=vol(t_coarse);
        rad(k) = f3r(k,radE);
        vol(k) = f3v(k,volE);
    end %IF
end %FOR

%%%%%%%%%%% Write Out Function Coefficients to Excel

T=table({'Growth End Time';'Coarsening Start Time';'Coarsening End Time';...
        'Radius';'Radius';'Radius';'Radius';'Radius';'Radius';...
        'Volume Fraction';'Volume Fraction';'Volume Fraction';...
        'Volume Fraction';'Volume Fraction';'Volume Fraction'},...
        {'-';'-';'-';'Max/Saturation Value (A)';...
        'Initial Value (B)';'Rise Constant (C)';'Exponential Rise Constant (D)';...
        'Decay Constant (E)';'Exponential Decay Constant (F)';'Max/Saturation
Value (A)';...
        'Initial Value (B)';'Rise Constant (C)';'Exponential Rise Constant (D)';...
        'Decay Constant (E)';'Exponential Decay Constant (F)'},...
        [t_growth;t_growth;t_coarse;radA;radB;radC;radD;radE;radF;...
         volA;volB;volC;volD;volE;volF]);

T.Properties.VariableNames={'Parameter','Coefficient','Value'};
writetable(T,'Carbide Behavior Parameters.xls')

    end %FUNCTION
```

APPENDIX B

Grain Boundary Sliding Model

Function File Name: nm_ngb_forward.m
Description: Written to couple matrix and GBS models in a serial fashion - nm previously known as a function of time and called in to be used at each time interval to be used as the ngb value such that the dislocation pileup kinetics can be calculated followed by sliding rate and strain

```
clear nm ngb Tback Tnet dnpdt dudt depsdt np eps i_max
sigma=200E6;
sigma0=200E6;
TF=sqrt(3);
tau=sigma/TF;
d_grain_array=[68E-6 191.5E-6 209.5E-6 256.1E-6];% 0hr / 3hr / 7hr / 30 hr
r_m_array=[b 6.2E-8 8.8E-8 9.8E-8];% 0hr / 3hr / 7hr / 30 hr
r_GB_array=[b 0.17E-6 0.23E-6 0.24E-6];% 0hr / 3hr / 7hr / 30 hr
lambda_GB_array=[((pi*d_grain(1))/6) 1.39E-6 1.25E-6 1.16E-6]; % 0hr / 3hr /
7hr / 30hr
K_array=[0.0046 0.4818; 0.0051 0.4248; 0.0012 0.5717; 0.0044 0.4335; 0.0057
0.3293];% 0hr / 3hr / 7hr / 30hr / 3hr-reload (3hrR1)

sheet='SR3hrR1_alt';
lambda_GB=lambda_GB_array(2);
r_GB=r_GB_array(2);
d_grain=d_grain_array(2);


C3=(D/r_GB^2)*(exp((sigma*b^3)/(kb*T))-1); %climb rate constant term
C4=110E1; %material constant (1/mu)

%Viscosity for the 0hr Specimen has a lesser viscosity with more dislocations
%presumably in the grain boundary in accordance with Ashby's work

if strcmp(sheet,'SR0hr_alt')==1
   eta=3E7;%0 hr
elseif strcmp(sheet,'SR3hrR1_alt')==1
   eta=2E12; %3hrR1 reload specimen
elseif strcmp(sheet,'SR3hr_alt')==1
   eta=3E8;%3 hr
else %strcmp(sheet,'SR30hr_alt')==1
   eta=5E8;%30 hr
end

%Initialize and establish loop variable
```

```
i_max=234*3600; %Added in v2 in order to standardize time domains amongst
SR specimens

time=zeros(i_max,1);
%time=[0:i_max]';
%(time) is introduced as a way to control time domain outside of test data
%since curve fits are used for stress relaxation. This allows for
%consistency between specimens WRT to the time domain
time=[0:i_max]';

%Initial conditions

cd('C:\University of Rhode Island\Paper2\Simulations')

%Read in time values of nm from matrix deformation model

% nm_range=['C1:C',num2str(i_max)];
% nm(:)=xlsread('nm_master.xlsx','3hrR1',nm_range);

%Only use for extended run (~230 hrs) for Paper 2 plot
% i_max=234*3600;
cd('C:\University of Rhode Island\Paper2\Simulations\03242019');
nm_range=['C1:C',num2str(i_max)];
nm(:)=xlsread('nm.xlsx','3hrR1',nm_range);

%Assumes pileup has relaxed after unloading, but ngb population is still
%present
Tback(1,1)=0;
np(1,1)=0;

%Read in last calculated value of ngb from 3hr simulation
%Read in ngb from last data point where model is valid (Stress exponent n > 3 for
t <= 36 hours)

%Number of dislocations within the grain boundary from the original 3 hr
%simulation prior to reloading. This will assume that the last calculated
%value for ngb is the new initial value for the 3hrR1 reload specimen/simulation

cd('C:\University of Rhode Island\Paper2\Simulations')
ngb(1,1)=xlsread('nm_master.xlsx','3hr',['J',num2str(36*3600)]);


Tnet(1,1)=tau;

%Amount of accumulated inelastic grain boundary sliding from the original
```

```
%3 hr simulation prior to reloading. This will assume that the last
%calculated value for u_inelastic is the new intial value for the 3hrR1
%reload specimen/simulation
u_inelastic(1,1)=u_inelastic_3hr(36*3600,2);

%Assume no measurable global plastic strain
eps(1,1)=0;%u_inelastic(1,1)/lambda_GB;


for i=1:i_max
   dt=1;
   inc=time(i)+((time(i+1)-time(i))/2);
   ngb(i,1)=ngb(1,1)+nm(i);

   dnpdt(i,1)=inc;
   dnpdt(i,2)=((ngb(i,1)*Md*b)/lambda_GB)*Tnet(i,1)/C4-np(i,1)*C3;

   np(i+1,1)=np(i,1)+dnpdt(i,2)*dt;

   dTbackdt(i,1)=inc;
   dTbackdt(i,2)=dnpdt(i,2)*((G*b)/(2*pi*(1-
v)*lambda_GB))*log(lambda_GB/b);

   Tback(i+1,1)=Tback(i,1)+dTbackdt(i,2)*dt;
   Tnet(i+1,1)=tau-Tback(i+1,1);

   dudt(i,1)=inc;
   dudt(i,2)=Tnet(i+1,1)*(b/eta);

   u_inelastic(i+1)=u_inelastic(i,1)+dudt(i,2)*dt;

   depsdt(i,1)=inc;
   depsdt(i,2)=dudt(i,2)*(1/lambda_GB)*TF;

   eps(i+1,1)=eps(i,1)+depsdt(i,2)*dt;

end

figure
semilogy(time,CR1(K_array(5,:),time),'r',time,eps,'b');

legend('3 hr Aged, Reloaded - Experimental (Curve Fit)','3 hr Aged, Reloaded -
Simulation');
legend('location','southeast');
xlabel('Time (sec)');
```

```
ylabel('Global Inelastic Strain (m/m)');

cd('C:\University of Rhode Island\Paper2\Simulations');


%%%  Data Reduction Loop for General Usage %%%
%%% Toggle On and Off as Needed %%%

    SR2R1_sim_data_reduc=[time(1) CR1(K_array(5,:),time(1)) eps(1) ];
    j=2;
    for i=1000:1000:size(eps,1)
       SR2R1_sim_data_reduc(j,:)=[time(i) CR1(K_array(5,:),time(i)) eps(i)];
       j=j+1;
    end

xlswrite('SR2R1_simvsdata.xlsx',SR2R1_sim_data_reduc,'Sheet1',['A1:C',num2st
r(size(SR2R1_sim_data_reduc,1))]);
    xlswrite('SR2R1_simvsdata.xlsx',[C4; eps; eta],'Constants',['A1:A3']
```

APPENDIX C

Stress Relaxation Experimental Data Post-Processing Script

Function File Name: SRdata_readin_v2.m
Description: Reads in load ramp and stress relaxation data from the native .dat files produced by the MTS test machine software. Load ramp data files contain time (seconds), temperature (Volts), axial force (N), and axial displacement (mm) columns. Stress relaxation data files contain time (seconds), temperature (Volts), force (Newtons), displacement (mm), and displacement error (mm) columns. Script will output data in a manner such that force-displacement and stress relaxation curves can be generated.

```
prompt='Enter name of data set you wish to analyze (0hr, 3hr, 7hr, or 30hr): ';
str=input(prompt,'s');
datastr=['data_',str];
fclose all;

%% Read in stress relaxation data
%Columns 1-5:
%time (sec)  temperature (volts)  force (N)  Displacement (mm) Displacement
Error (mm)
file=('SR_Hold_data.dat');

if strcmp(str,'0hr')==1
   cd('C:\University of Rhode Island\Experimental\A617 Accelerated Creep
Testing\Test Data\A617-SR-Sol-2');
   fid=fopen(file);
   while ~feof(fid)
      C=textscan(fid,'%s %s %s %s %s','headerlines',5);
   end
      data_0hr=cellfun(@str2double,C,'UniformOutput',0);
      data_0hr=[data_0hr{:}];

elseif strcmp(str,'3hr')==1
   cd('C:\University of Rhode Island\Experimental\A617 Accelerated Creep
Testing\Test Data\A617-SR-3');
   fid=fopen(file);
   while ~feof(fid)
      C=textscan(fid,'%s %s %s %s %s','headerlines',5);
   end
      data_3hr=cellfun(@str2double,C,'UniformOutput',0);
      data_3hr=[data_3hr{:}];

elseif strcmp(str,'7hr')==1
   cd('C:\University of Rhode Island\Experimental\A617 Accelerated Creep
Testing\Test Data\A617-SR-7hr');
```

```
    fid=fopen(file);
    while ~feof(fid)
        C=textscan(fid,'%s %s %s %s %s','headerlines',5);
    end
        data_7hr=cellfun(@str2double,C,'UniformOutput',0);
        data_7hr=[data_7hr{:}];
else %strcmp(str,'30hr')==1
    cd('C:\University of Rhode Island\Experimental\A617 Accelerated Creep
Testing\Test Data\A617-SR-30');
    fid=fopen(file);
    while ~feof(fid)
        C=textscan(fid,'%s %s %s %s %s','headerlines',5);
    end
        data_30hr=cellfun(@str2double,C,'UniformOutput',0);
        data_30hr=[data_30hr{:}];
end

fclose(fid)


%% %Load Force-Displacement data for Elastic Loading Verification
%Columns 1-4:
%Time (s)  Temperature (v)  Axial Force(N)  Axial Displacement(mm)


file=('SR_Ramp_data.dat');
fid=fopen(file);

if strcmp(str,'0hr')==1
        cd('C:\University of Rhode Island\Experimental\A617 Accelerated Creep
Testing\Test Data');
        fid=fopen(file);
        while ~feof(fid)
            C=textscan(fid,'%s %s %s %s %s','headerlines',5);
        end
        FDdata_0hr=cellfun(@str2double,C,'UniformOutput',0);
        FDdata_0hr=[FDdata_0hr{:}];

elseif strcmp(str,'3hr')==1
      cd('C:\University of Rhode Island\Experimental\A617 Accelerated Creep
Testing\Test Data\A617-SR-3');
      fid=fopen(file);
      while ~feof(fid)
          C=textscan(fid,'%s %s %s %s %s','headerlines',5);
      end
```

```
    FDdata_3hr=cellfun(@str2double,C,'UniformOutput',0);
    FDdata_3hr=[FDdata_3hr{:}];

elseif strcmp(str,'7hr')==1
    cd('C:\University of Rhode Island\Experimental\A617 Accelerated Creep
Testing\Test Data\A617-SR-7hr');
    fid=fopen(file);
    while ~feof(fid)
        C=textscan(fid,'%s %s %s %s %s','headerlines',5);
    end
    FDdata_7hr=cellfun(@str2double,C,'UniformOutput',0);
    FDdata_7hr=[FDdata_7hr{:}];

else %strcmp(str,'30hr')==1
     cd('C:\University of Rhode Island\Experimental\A617 Accelerated Creep
Testing\Test Data\A617-SR-30');
     fid=fopen(file);
     while ~feof(fid)
        C=textscan(fid,'%s %s %s %s %s','headerlines',5);
     end
     FDdata_30hr=cellfun(@str2double,C,'UniformOutput',0);
     FDdata_30hr=[FDdata_30hr{:}];
end

fclose(fid)


%% Write original data to Excel

fclose all
cd('C:\University of Rhode Island\Experimental\A617 Accelerated Creep
Testing\Test Data\A617-SR-3');
sheet2=['F-D_',str];
excelfile='SR_data.xlsx';

if strcmp(str,'0hr')==1
   xlswrite(excelfile,FDdata_0hr,sheet2);
elseif strcmp(str,'3hr')==1
   xlswrite(excelfile,FDdata_3hr,sheet2);
elseif strcmp(str,'7hr')==1
   xlswrite(excelfile,FDdata_7hr,sheet2);
else %strcmp(str,'30hr')==1
   xlswrite(excelfile,FDdata_30hr,sheet2);
end
```

```
%% Write manipulated data to Excel (manipulations described in subsequent
comments)


%Time shift for all data
if strcmp(str,'0hr')==1
    area_0hr=86.69; %mm^2
    FDdata_0hr(:,1)=FDdata_0hr(:,1)-FDdata_0hr(1,1);
    data_0hr(:,1)=data_0hr(:,1)-data_0hr(1,1);
elseif strcmp(str,'3hr')==1
    area_3hr=75.85; %mm^2
    FDdata_3hr(:,1)=FDdata_3hr(:,1)-FDdata_3hr(1,1);
    data_3hr(:,1)=data_3hr(:,1)-data_3hr(1,1);
elseif strcmp(str,'7hr')==1
    area_7hr=90.98; %mm^2
    FDdata_7hr(:,1)=FDdata_7hr(:,1)-FDdata_7hr(1,1);
    data_7hr(:,1)=data_7hr(:,1)-data_7hr(1,1);
else %strcmp(str,'30hr')==1
    area_30hr=82.32; %mm^2
    FDdata_30hr(:,1)=FDdata_30hr(:,1)-FDdata_30hr(1,1);
    data_30hr(:,1)=data_30hr(:,1)-data_30hr(1,1);
end


if strcmp(str,'0hr')==1
    %Making load positive in value for SR curves
    data_0hr(:,3)=-1*data_0hr(:,3);
    %Making load positive in value for F-D curves
    FDdata_0hr(:,3)=-1*FDdata_0hr(:,3);
    %Making displacement positive in value for F-D curves
    FDdata_0hr(:,4)=-1*FDdata_0hr(:,4);
    %Compressive stress calculated from 0hr specimen area
    sigma_0hr(:,1)=data_0hr(:,3)/area_0hr;
    %Concatenating matrices of information of interest
    FD0hr=[FDdata_0hr(:,1) FDdata_0hr(:,4) FDdata_0hr(:,3)];%Columns: Time,
Disp, Load
    SR0hr=[data_0hr(:,1) sigma_0hr(:,1)]; %Columns: Time, Stress
    %Sheet labels for Excel dump
    sheet3='FD0hr_alt';
    sheet4='SR0hr_alt';
    %Excel dump
    xlswrite(excelfile,FD0hr,sheet3);
```

```
    xlswrite(excelfile,SR0hr,sheet4);

elseif strcmp(str,'3hr')==1
    %Making load positive in value for SR curves
    data_3hr(:,3)=-1*data_3hr(:,3);
    %Making load positive in value for F-D curves
    FDdata_3hr(:,3)=-1*FDdata_3hr(:,3);
    %Making displacement positive in value for F-D curves
    FDdata_3hr(:,4)=-1*FDdata_3hr(:,4);
    %Compressive stress calculated from 3hr specimen area
    sigma_3hr(:,1)=data_3hr(:,3)/area_3hr;
    %Concatenating matrices of information of interest
    FD3hr=[FDdata_3hr(:,1) FDdata_3hr(:,4) FDdata_3hr(:,3)]; %Columns: Time,
Disp, Load
    SR3hr=[data_3hr(:,1) sigma_3hr(:,1)]; %Columns: Time, Stress
    %Sheet labels for Excel dump
    sheet5='FD3hr_alt';
    sheet6='SR3hr_alt';
    %Excel dump
    xlswrite(excelfile,FD3hr,sheet5);
    xlswrite(excelfile,SR3hr,sheet6);

elseif strcmp(str,'7hr')==1
    %Making load positive in value for SR curves
    data_7hr(:,3)=-1*data_7hr(:,3);
    %Making load positive in value for F-D curves
    FDdata_7hr(:,3)=-1*FDdata_7hr(:,3);
    %Making displacement positive in value for F-D curves
    FDdata_7hr(:,4)=-1*FDdata_7hr(:,4);
    %Compressive stress calculated from 7hr specimen area
    sigma_7hr(:,1)=data_7hr(:,3)/area_7hr;
    %Concatenating matrices of information of interest
    FD7hr=[FDdata_7hr(:,1) FDdata_7hr(:,4) FDdata_7hr(:,3)]; %Columns: Time,
Disp, Load
    SR7hr=[data_7hr(:,1) sigma_7hr(:,1)]; %Columns: Time, Stress
    %Sheet labels for Excel dump
    sheet7='FD7hr_alt';
    sheet8='SR7hr_alt';
    %Excel Dump
    xlswrite(excelfile,FD7hr,sheet7);
    xlswrite(excelfile,SR7hr,sheet8);

else %strcmp(str,'30hr')==1
    %Making load positive in value for SR curves
    data_30hr(:,3)=-1*data_30hr(:,3);
```

```
    %Making load positive in value for F-D curves
    FDdata_30hr(:,3)=-1*FDdata_30hr(:,3);
    %Making displacement positive in value for F-D curves
    FDdata_30hr(:,4)=-1*FDdata_30hr(:,4);
    %Compressive stress calculated from 30hr specimen area
    sigma_30hr(:,1)=data_30hr(:,3)/area_30hr;
    %Concatenating matrices of information of interest
    FD30hr=[FDdata_30hr(:,1) FDdata_30hr(:,4) FDdata_30hr(:,3)]; %Columns:
Time, Disp, Load
    SR30hr=[data_30hr(:,1) sigma_30hr(:,1)]; %Columns: Time, Stress
    %Sheet labels for Excel Dump
    sheet9='FD30hr_alt';
    sheet10='SR30hr_alt';
    %Excel Dump
    xlswrite(excelfile,FD30hr,sheet9);
    xlswrite(excelfile,SR30hr,sheet10);
end

%%% Plot Block  - Toggle On and Off as Needed %%%
%
% figure
% plot(-data_0hr(1,1)+data_0hr(:,1),-1*data_0hr(:,3)./area_0hr,'r',...
%     -data_3hr(1,1)+data_3hr(:,1),-1*data_3hr(:,3)./area_3hr,'b',...
%     -data_7hr(1,1)+data_7hr(:,1),-1*data_7hr(:,3)./area_7hr,'g',...
%     -data_30hr(1,1)+data_30hr(:,1),-1*data_30hr(:,3)./area_30hr,'m');
% xlabel('Time (sec)')
% ylabel('Compressive Stress (MPa)')
% title('Stress Relaxation - A617 at 780 deg. C')
% legend('Solutioned','3 hr Aged','7 hr Aged', '30 hr Aged')

% figure
% %Force Displacement Plot
% plot(-1*FDdata_0hr(:,4),-1*FDdata_0hr(:,3),'r',-1*FDdata_3hr(:,4),-
1*FDdata_3hr(:,3),'b',...
%     -1*FDdata_7hr(:,4),-1*FDdata_7hr(:,3),'g',-1*FDdata_30hr(:,4),-
1*FDdata_30hr(:,3),'m');
% xlabel('Displacement - Compression (mm)')
% ylabel('Compressive Force (N)');
% title('Force vs. Displacement - A617 Stress Relaxation at 780 deg. C ')
% legend('Solution','3 hr Aged', '7 hr Aged','30 hr Aged');

% %%
% k=1;
% for i=1:3600:size(sigma_rate_0hr,1)
%     sig_rate_0hr_reduc(k,:)=[sigma_rate_0hr(i,1) sigma_rate_0hr(i,2)];
```

```
%     k=k+1;
% end
% plot(sig_rate_0hr_reduc(:,1),sig_rate_0hr_reduc(:,2))
```

APPENDIX D

Flowchart for Coupled, Matrix Deformation – Grain Boundary Sliding Model for Constant Microstructure Condition

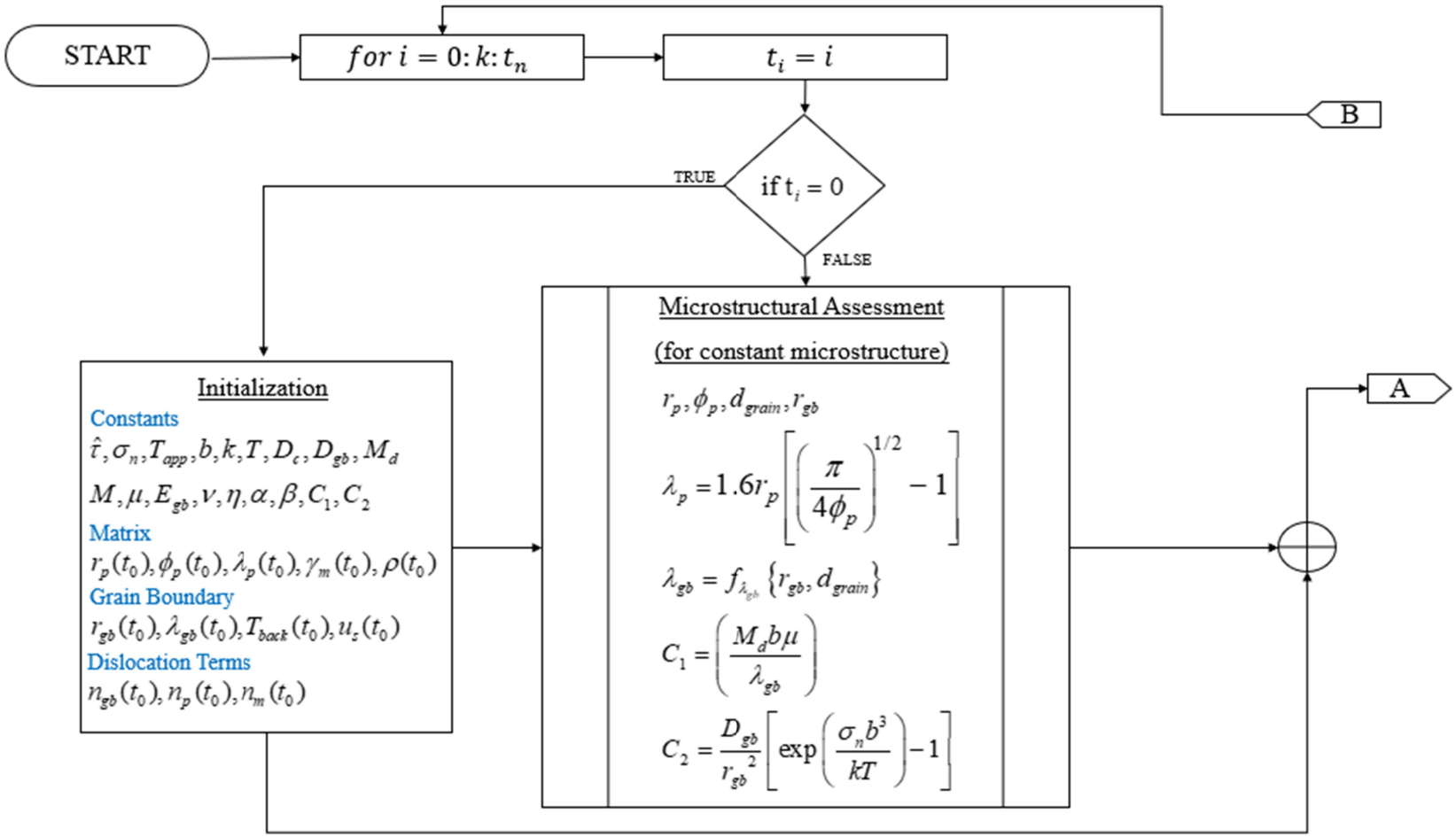
START
$for\ i = 0{:}\,k{:}\,t_n$
$t_i = i$
B
TRUE
if $t_i = 0$
FALSE
Initialization
Constants
$\hat{\tau}, \sigma_n, T_{app}, b, k, T, D_c, D_{gb}, M_d$
$M, \mu, E_{gb}, \nu, \eta, \alpha, \beta, C_1, C_2$
Matrix
$r_p(t_0), \phi_p(t_0), \lambda_p(t_0), \gamma_m(t_0), \rho(t_0)$
Grain Boundary
$r_{gb}(t_0), \lambda_{gb}(t_0), T_{back}(t_0), u_s(t_0)$
Dislocation Terms
$n_{gb}(t_0), n_p(t_0), n_m(t_0)$
Microstructural Assessment
(for constant microstructure)
$r_p, \phi_p, d_{grain}, r_{gb}$
$\lambda_p = 1.6 r_p \left[\left(\frac{\pi}{4\phi_p} \right)^{1/2} - 1 \right]$
$\lambda_{gb} = f_{\lambda_{gb}} \{ r_{gb}, d_{grain} \}$
$C_1 = \left(\frac{M_d b \mu}{\lambda_{gb}} \right)$
$C_2 = \frac{D_{gb}}{r_{gb}^2} \left[\exp\left(\frac{\sigma_n b^3}{kT} \right) - 1 \right]$
A

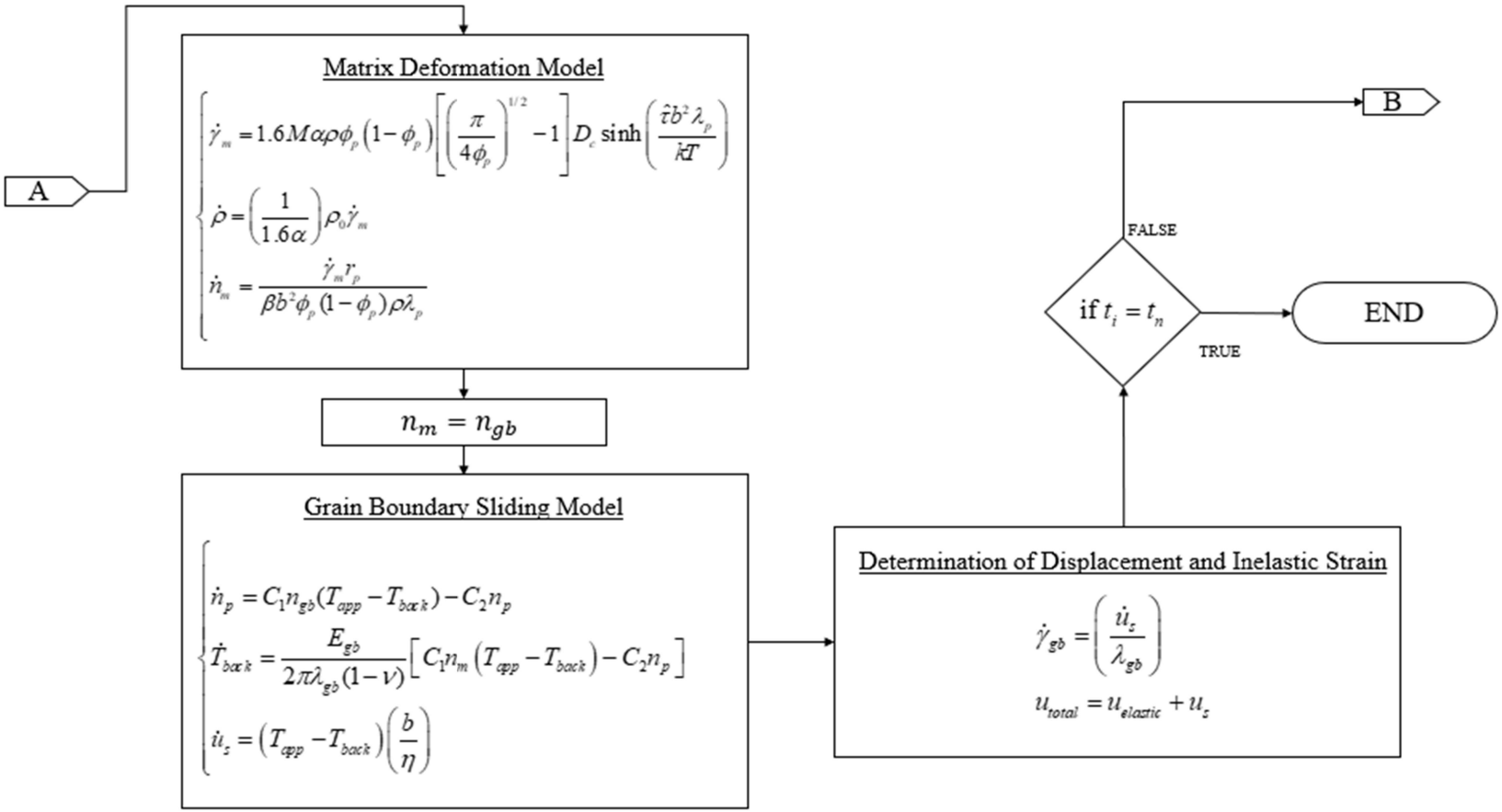
A
Matrix Deformation Model
$\dot{\gamma}_m = 1.6M\alpha\rho\phi_p(1-\phi_p)\left[\left(\frac{\pi}{4\phi_p}\right)^{1/2}-1\right]D_c\sinh\left(\frac{\hat{\tau}b^2\lambda_p}{kT}\right)$
$\dot{\rho} = \left(\frac{1}{1.6\alpha}\right)\rho_0\dot{\gamma}_m$
$\dot{n}_m = \frac{\dot{\gamma}_m r_p}{\beta b^2\phi_p(1-\phi_p)\rho\lambda_p}$
$n_m = n_{gb}$
Grain Boundary Sliding Model
$\dot{n}_p = C_1 n_{gb}(T_{app}-T_{back})-C_2 n_p$
$\dot{T}_{back} = \frac{E_{gb}}{2\pi\lambda_{gb}(1-\nu)}\left[C_1 n_m\left(T_{app}-T_{back}\right)-C_2 n_p\right]$
$\dot{u}_s = \left(T_{app}-T_{back}\right)\left(\frac{b}{\eta}\right)$
Determination of Displacement and Inelastic Strain
$\dot{\gamma}_{gb} = \left(\frac{\dot{u}_s}{\lambda_{gb}}\right)$
$u_{total} = u_{elastic} + u_s$
if $t_i = t_n$
FALSE
TRUE
B
END